6-22-2022

Additive Manufacturing and Applications of Silica Glass Materials

Omena Okpowe
ookpo002@fiu.edu

Recommended Citation

Okpowe, Omena, "Additive Manufacturing and Applications of Silica Glass Materials" (2022). *FIU Electronic Theses and Dissertations*. 5021.
https://digitalcommons.fiu.edu/etd/5021

FLORIDA INTERNATIONAL UNIVERSITY

Miami, Florida

ADDITIVE MANUFACTURING AND APPLICATIONS OF SILICA GLASS MATERIALS

A dissertation submitted in partial fulfillment of the

requirements for the degree of

DOCTOR OF PHILOSOPHY

in

MATERIALS SCIENCE AND ENGINEERING

by

Omena Okpowe

2022

To: Dean John L. Volakis
College of Engineering and Computing

This dissertation, written by Omena Okpowe, and entitled Additive Manufacturing and Applications of Silica Glass Materials, having been approved in respect to style and intellectual content, is referred to you for judgment.

We have read this dissertation and recommend that it be approved.

Norman Munroe

Jiuhua Chen

Bilal El-Zahab

Nezih Pala, Co-Major Professor

Chunlei Wang, Co-Major Professor

Date of Defense: June 22, 2022

The dissertation of Omena Okpowe is approved.

Dean John L. Volakis
College of Engineering and Computing

Andres G. Gil
Vice President for Research and Economic Development and
Dean of the University Graduate School

Florida International University, 2022

DEDICATION

I dedicate this dissertation to God who saw me through all of this.

ACKNOWLEDGMENTS

I am grateful to my supervisor, Dr Chunlei Wang, for her supervision and immense support. Her research experience and knowledge enriched my graduate experience significantly. I am grateful for her mentorship.

I would also like to appreciate my co-supervisor, Dr Nezih Pala for his immense support and the stability he inculcated into my research.

I would like to express my gratitude to the members of my dissertation committee, Dr. Norman Munroe, Dr Jiuhua Chen and Dr El-Zahab for accepting to serve on my committee as well as for their contributions, encouragement, motivation and counsel towards my dissertation.

I would want to express my appreciation to all members of the Wang group past and present. I am thankful to Dr Durygin and Dr Drozd of CESMEC as well as Dr Francoh, Mr. Schwarz and Mr. Milian of AMERI.

I am thankful to CESMEC, INSYST and AMERI for the use of their facilities as well as the Mechanical Engineering Department and the University Graduate School for funding my graduate studies.

I am thankful to family: My parents, especially my mother, who was a constant source of support and my greatest encouragement, my dear wife, brothers, sisters, in-laws and friends who were equally very supportive.

ABSTRACT OF THE THESIS

ADDITIVE MANUFACTURING AND APPLICATIONS OF SILICA GLASS MATERIALS

by

Omena Okpowe

Florida International University, 2022

Miami, Florida

Professor Chunlei Wang, Co-Major Professor

Professor Nezih Pala, Co-Major Professor

The difficulty in shaping and fabrication of miniaturized features on glass structures using conventional fabrication techniques makes the recent advancements in glass manufacturing necessary. Pioneer efforts towards glass additive manufacturing have proven to be the nexus between the past and the future of glass fabrication. Additive manufacturing potentially allows for speed, scalability, environmental and cost friendliness, high resolution as well as flexibility for functional glass materials. Adapting additive manufacturing methods toward glass fabrication is thus of great importance.

We first fabricated three dimensional doped and undoped Borosilicate glasses via stereolithography which exhibited comparable optical properties to commercial glasses, irrespective of their low softening temperatures. Processing parameters of densification and calcination were optimized to achieve structural and optical stability of the resulting undoped and Cerium-doped borosilicate glass. Optical parameters including the optical band gap, Urbach energy and refractive index were deduced from the optical absorption spectra with comparable quality to doped glasses fabricated by other methods.

The glasses exhibited a band gap of 3 eV, Urbach energy of 0.75 eV and refractive index of 2.14 for 8 % Ce-doped glass, respectively. The results indicate the suitability of Cerium-doped glass fabricated by stereolithography for luminescence applications and that additive manufacturing could be promising for borosilicate glass fabrication.

We also investigated the use of the stereolithography technique for fabrication of functionally graded materials with emphasis on gradient refractive index optics. These class of materials allow for planar surfaces which make mounting in complex optical systems much easier in addition to providing enhanced optical properties. They find applications in facets such as micro-optical telescopes, solid state lasers, fiber collimators, optical data storage etc. Stereolithography is a good technique for gradient refractive index optics because it allows for a flexibility of dopant inculcation so that there is a variation in the refractive within the glass structure. Our simulation results for the gradient optical lens designs based on the adoption of the precursor cum resin sludge properties showed measurable and tunable optical properties such as spherical aberrations. Experimental results establish stereolithography as a veritable technique and show the propensity for the adaptation of this technique for the fabrication process.

TABLE OF CONTENTS

LIST OF TABLES

TABLE PAGE

LIST OF FIGURES

Introduction

1.1 Overview

The continuous new dimensions in the field of additive manufacturing has resulted in efforts geared towards adopting various techniques and approaches for its application towards glass ceramics and functional glass applications. Its key advantages are that it helps in overcoming challenges associated with glass fabrication such as difficulty in shaping, the resort to high temperatures for processing, resort to hazardous chemicals for miniaturization and the difficulty in tuning properties of these glass materials. Among the various additive manufacturing types, stereolithography has now become a better alternative for glass and ceramic additive manufacturing because it provides for high resolution structures, on demand manufacturing as well as being customer specific. Since the advent of Stereolithography by Chuck Hall in 1986, several research and innovations have led to a variety of other types of additive manufacturing techniques in addition to improvements to enable its application to polymeric, composites, metals, ceramics etc. 3D printing of glass has now gradually evolved to being established as a field of research. It has now helped to overcome key issues associated with glass manufacturing such as resort to hazardous chemicals and high temperatures, while also allowing for a flexible property tunability of final glass ensembles to enable an extended range of applications such as in electronics, optical, biomedical devices, etc. Among the eight categories of 3D printing, VPP and Direct Ink Writing have been the most successful with regards to glass manufacture and are now a subject of intense research. VPP process for ceramics is a cold cure process that entails 3D printing a pre-polymer resin-ceramic mix based on a light source of some wavelength, and then subjecting it to thermal processing. Herein we present a summary of mechanisms, techniques and materials for vat based photopolymerization with specific emphasis on its application towards glass additive manufacturing. It also encompasses recent trends and advances in the field for transparent glass ceramics such as the use of alternative sol gel and preceramic precursors, doping and miniaturization trends.

1.2 Research Objectives and Approaches

Figure 1 is a flow chart showing the research plan in this dissertation. The ultimate goal is to show the possibility as well as develop new glass and functional glass materials via additive manufacturing. We have focused on the stereolithographic technique (SLA) for this dissertation. Conventional glass manufacture comprises melting and quenching processes as well as resort to substances such as Hydrogen Fluoride for miniature and high-resolution structures. These techniques sometimes require mold construction so as to sustain high temperatures as well as resort to high melt temperatures. In this dissertation, we fabricated borosilicate glass structures using stereolithography approach to show the possibility for low softening temperature glasses via stereolithography. We then introduce rare earth dopants into their structures to allow for functional glasses such as luminescent and scintillating glasses. Finally, we design a laboratory made 3D printer that allows for the fabrication of functionally gradient glass materials with gradient optical properties.

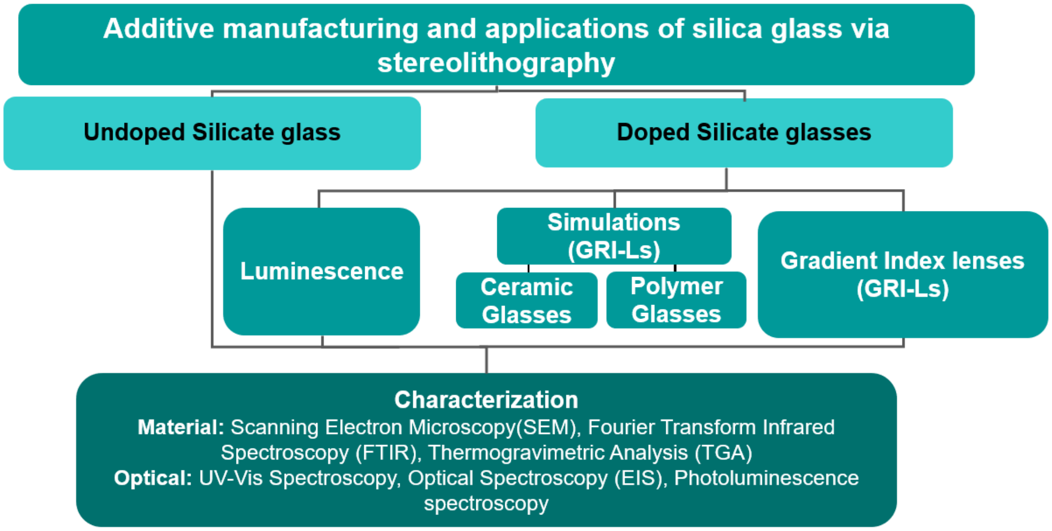

Figure 1: Research plan

1.3 Hypotheses

The main objective of this research was to develop silicate materials via a tripartite photocure, debind and sinter process of a liquid glass composite. A secondary objective was to investigate the tunability of the process to enable inculcation of dopants, which can result in functional glass materials with appropriate luminescent and optical properties.

Key hypotheses were:

a) The debinding and Sintering conditions could be optimized to enable the application of stereolithography to low softening temperature glass ceramics.

b) Additive manufacturing (Stereolithography) facilitates an improved process for fabrication of functional glass materials such as 3D Ce-doped glass scintillators for radiation sensing as well as Gradient Index systems via dopant and process control.

c) By coupling the Stereolithography approach with sol gel precursors, functional glass materials can be fabricated to enable a cleaner fabrication route.

d) Simulations enables precision control of properties for SLA fabrication of functionally graded materials such as GRI-Ls.

1.4 Scope of the Dissertation

The second chapter gives background information about Additive manufacturing of silica glass materials. It also discusses the current trends and techniques for attaining functional glass materials via additive manufacturing. Chapter 3 discusses the results of an Additive manufacturing procedure for Borosilicate glass fabrication via stereolithography. Chapter 4 presents the results of simulation and preliminary results about incorporation of Stereolithography towards fabrication of Gradient Refractive Index Lens optical properties are simulated and the miscibility of the sol gel precursors and photocurable resin mixes are investigated. Chapter 5 discusses further the stereolithography-simulated results for a pure hybrid resin lens system based on a mixture of epoxy and acrylate resin systems. Chapter 6 gives a summary of the major observations from this work and provide some recommendations for future efforts.

Background and Literature Review

2.1 Background

Glass additive manufacturing was predated by porous ceramic additive manufacturing which were first reported using powder selective laser sintering in 1990 [1]. Although several reviews exist for additive manufacturing of ceramics [2]–[7], this review is focused on current progress and trends for silica glass vat additive manufacturing. Hitherto, the conventional method for glass fabrication had been by melt-quenching. Additive manufacturing helps to overcome some challenges associated with glass fabrication such as difficulty in shaping, the resort to high temperatures for processing, resort to hazardous chemicals for miniaturization and the difficulty in tuning properties of these glass materials. Figure 2-1 shows the accelerated interest in additive manufacturing for glass ceramic materials since 1986. The use of material extrusion [8] and stop flow lithography [9] have been reported for glass additive manufacturing of SiO_2 glass, but these have resulted in rough structures [8] and 2D structures respectively. Attempts on additive manufacturing of borosilicate glass using Direct laser sintering [10] and soda lime glass using selective laser melting [11] were also reported, however, both resulted in non-transparent glass products. The use of thermoplastic binders coupled with UV curable ink for casting, photo structuring and calcination was also patented in 2020 [12]. This work yielded crystalline glass (here “crystalline” means higher transparency with neutral color) products.

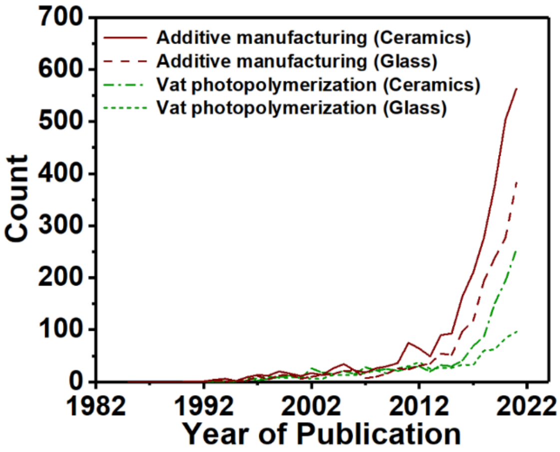

Figure 2-1: Research works in Glass and Ceramic additive manufacturing and VPP as observed from the number of annual research articles (culled from Web of Science, accessed February, 2022).

In recent times, two sludge-based AM approaches have been shown to be successful. These have been based on VPP and Direct Ink Writing. In both approaches, ceramic precursors are mixed with liquid prepolymer resins, 3D printed and then subjected to post printing (typically thermal) processing. The successes of both works have led to extended research aimed at improving the overall fabrication process.

In recent times, two sludge-based AM approaches have been shown to be successful. These have been based on VPP and DIW. In both approaches, ceramic precursors are mixed with liquid prepolymer resins, 3D printed and then subjected to post printing (typically thermal) processing. The successes of both works have led to extended research aimed at improving the overall fabrication process. The DIW technique was first patented for additive manufacturing of ceramics by Calvert and coworkers [13]. DIW had been used for 3D printing for a wide range of materials such as photonic crystals [14], [15], energy devices [16] etc. until its recent success with glass materials. In this technique, which is a variant of material extrusion, the rheological properties of the sludge are tuned in such a way that in the presence of a shear force the viscous liquid flows and thins to maximize the z resolution of the eventual prints and then stops when the force is removed. Sludge components are also selected in such a way that the nano-filler ceramic particles do not clog the print nozzle. In adopting the DIW technique for glass fabrication, Dylla-Spears and co-workers [17] utilized sludges comprising fumed silica nanoparticles dispersed in high boiling point tetraglyme and polydimethylsiloxane (PDMS). The ceramic composition is tuned to allow for shear thinning during printing and then subjected to an extended drying, calcination and the

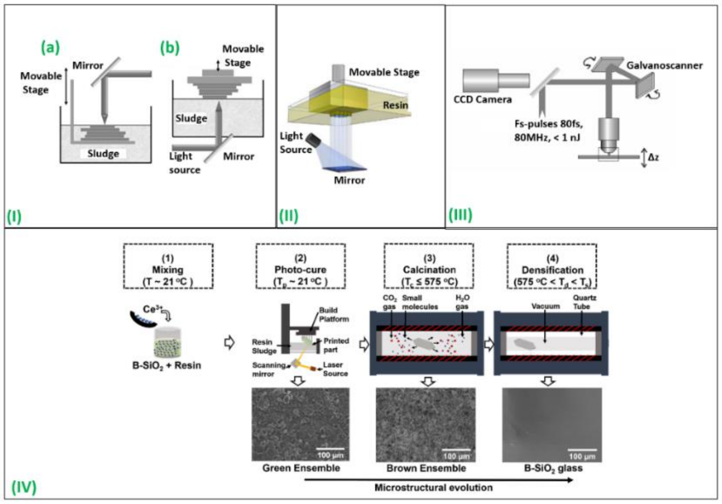

Figure 2-2: Schematic of (I) a stereolithography setup showing (a) top-down and (b) bottom-up printing mechanisms. Reproduced from [18]. (II) A Digital light processing set up. Reproduced from [19]. (III) A Two photon polymerization setup. Reproduced from [20]. (IV) Schematic of the main processes in the fabrication of 3D borosilicate glass ensembles. T_p, T_c, T_d and T_s indicate printing, calcination, densification and softening temperatures, respectively. Step (1): Mixing step (and incorporation e.g. Ce dopant); Step (2): Printing and photocuring process of the sludge using the SLA 3D printer; Step (3): Calcination process of the green ensemble in the furnace; Step (4): Densification process of the calcined glass within a vacuumed quartz tube in the furnace. Reproduced from [21].

densification process. The major challenge with this procedure has been the long drying time (~110hours). On the other hand, the VPP technique for ceramics offers a major advantage over the DIW because it takes a relatively shorter time. It includes stereolithography (SLA) as well as digital light processing (DLP), multiple photon polymerization (MPP) and their variants. Schematic 3D printers for these three sub types of additive manufacturing are shown in Figure 2-2. Stereolithography (SLA), a VPP technique was invented by Charles W.s Hall in 1984 [22]. VPP generally entails the curing of a liquid photosensitive pre-polymer resin mixture by an irradiation light source most commonly, UV. The later induces a chemical reaction by first attacking the photoinitiator which in turn reacts with the monomers and oligomers in the resin mixture thereby resulting in a highly cross-linked polymer network. Whereas the z-resolution is determined by the nature of the sludge, the laser diameter determines the x/y resolution even though both of these may go as low as tens of micrometers. Figure 2-2(IV) gives a pictorial description of the stages and microstructure scanning electron micrographs for the additive manufacturing of borosilicates via stereolithography. For ceramics, VPP entails first the mixing and dispersing of a pre-polymer resin mixture with ceramic filler particles leading to a photocurable sludge. The mixing may be carried out with the aid of surfactants or additives to allow for homogeneity. The sludge is then subjected to photocuring in the printer after which the calcination and densification processes are carried out. Figure 2-3(I) shows the resulting products after each step, as well as the images of the scanning electron microscopy tests obtained for typical printed, calcined and densified objects. Once the printing process is completed, the ceramic particles are embedded within the polymer matrix as only the polymer component is photosensitive.

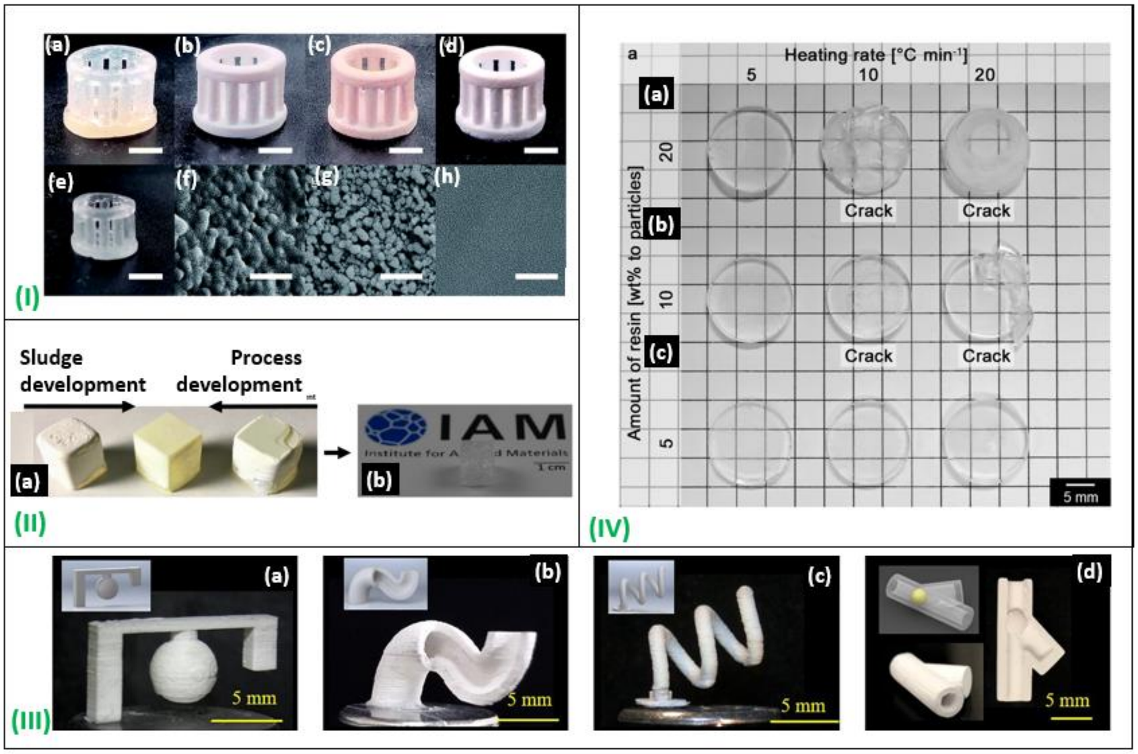

Figure 2-3: (I) SLA printed green ensemble subjected to isothermal heat treatments at a) 21 ˚C (b) 150 ˚C (c) 250 ˚C (d) 500 ˚C (e) 1250 ˚C; Scanning electron micrographs of surfaces post-thermal treatment at (f) 21 ˚C (g) 500 ˚C (h) 1250 ˚C. Reproduced from [23]. (II) (a) Green ensemble printed via SLA: inadequate resin composition (left) optimized resin composition and print parameters (center), inadequate print parameters (right). (b) sintered glass Ensemble at 1300 ˚C. Reproduced from [24]. (III) SLA printed green ensembles based on the Fabrication results via the Suspension-enclosing projection stereolithography (SEPS) process: (a) a suspended ball; (b) a windy tube (c) a spiral structure (d) a valve structure. Reproduced from [25]. (IV) Effect of heating rate and resin content on the crack observation in sintered glass from SLA based photocurable resins. Reproduced from [26].

Successful printing is typically dependent on the rheological and optical properties of the sludge as well as the eventual shrinkage in the final glass product, which in turn, to an extent is dependent on the sludge compositions and constituents. Good shear thinning, high particle loading as well as low viscosity are desired. The printing parameters such as curing intensity and time are also key. Work by Hoffman and coworkers. (Figure 2-3(II)) investigated how key print parameters affected the quality of final products [24]. The optimum concentration of initiator for polymerization process was established alongside investigations on rheology, cure kinetics and polymerization time. Sludge compositions may range from 30 vol % (low viscosity) to 60 vol % (high viscosity) of ceramics in the resin, however, it is best to keep the overall viscosity close to 3000 mPa which is typical for commercial resins. Higher viscosities result in lower shrinkage even though the light scattering and thickness of the sludge at high viscosities may affect printability.

DLP on the other hand was originally developed in 1987 by Larry Hornbeck of Texas Instruments [27]. Its working mechanism is almost the same as the SLA process except that, a micro mirror system is digitally utilized to project a light source on the photosensitive sludge one layer after another. instead of the printing process being dependent on a moving laser This layer after another printing makes it faster than the SLA technique and resolution here is dependent on the projection plane and the mirror. A hybrid system of TPP and DLP printing system has also been recently reported for SiOC structures where submicron structures were printed upon typical macro structures [28]. A key challenge with the VPP process is the resort to first fabricating support structures before the object itself. Although these supports help to prevent collapse of parts such as overhangs in complex prints as well as act as heat dissipaters for high temperature printing, subsequent removal of these supports may lead to poor surface properties as well as unwanted cracks in the fabricated objects. Work by Xuan Song and coworkers [25], utilized a ball milled elasto-viscoplastic liquid ensemble comprising a ceramic filler, prepolymer resin mix and a phosphate ester dispersant. Their printer setup was coupled with a heating system so that by regulating the temperature of the liquid ensemble during printing, the need for supports in their products were eliminated. Figure 2-3(III) shows some green ensemble structures printed without typical SLA support structures. A novel technique, computed axial lithography (CAL), which allows for a support free printing, a comparatively more rapid printing has been recently developed by Spadaccini and coworkers [29]. Unlike the SLA which photocures one laser spot at a time or the DLP which exposes a 2D plane at a time for photocuring it entails exposure of a rotating cylindrical vat containing a photocurable resin sludge to a coordinated system of light beams of different doses and orientation so that 3D structures may be created in an approximately single step.

Table 1 gives information on some recently successful additive manufacturing techniques for glass 3D printing as well as their peculiar challenges. Whereas the sludge-based techniques have a relatively low anisotropy while exhibiting relatively undesirable extended sintering times, compared to the fused deposition modelling (FDM) and powder bed fusion (PBF) techniques, they have a much higher resolution as a result of the nozzle and laser dimensions which are employed. The mechanical strength of printed products is a function of the quality of sintering where employed so that the both sludge-based techniques as well as the PBF technique exhibits relatively higher mechanical properties compared to FDM. In addition, the sludge-based AM techniques allow for room temperature fabrication of shapes and structures which is not possible with the PBF and FDM techniques as these are rather done at temperatures around the fusion temperatures of the precursor materials.

Table 2-1: Key Pros and Cons of Additive manufacturing techniques for glass manufacturing.

	FDM	PBF	DIW	Vat
Relative cost effectiveness	High	High	Low	Low
Anisotropy	High	High	Low	Low
Dependence on nozzle parameters diameter	n/a	n/a	High	n/a
Resolution/precision	Poor	Poor	Good	Good
Extended drying times	Not required	Not required	Not required	Not required
Post sintering	Not required	Not required	Required	Required
Printing temperature	High	High	Low (~25 ^{o}C)	Low (~25 ^{o}C)
Print accuracy/precision	Low	Low	High	High
Mechanical strength	Low	High	Good	Good
Availability to non-silica variants	High	High	Low	Low
Surface quality/roughness	Poor	Poor	Good	Good
References	[8][30]	[10], [31]	[17]	[21], [32]

Table 2 gives information on sludge composition of recent works on sludge based additive manufacturing for glass. Irrespective of the techniques used, the calcination temperatures have all been engineered to effectively eliminate all of the polymeric component of the green ensemble while not tampering with the printed structure or causing any significant pulverization. The ceramic component of the sludge thus far for silica glasses have either been fumed silica nanopowder which are known to exhibit thixotropic properties or sol gel precursors prepared from the so-called Stober process. The densification temperature and time condition are engineered to allow for the expected densities, accommodate dopants where present as well as prevent alteration to the structure fidelity and this has ranged between 700 ˚C to 1300 ˚C all below the softening temperature of the ceramic component of the green ensemble (most time silica). Key novelties thus far reported include high resolution features, application tailored precision doping, extension to the use of low softening temperature precursor ceramics such as borosilicates, use of commercial sludges as well as the use of Computed Axial Lithography for single step printing.

Table 2-2: Recent approaches for vat polymerization of silica glass structures.

3D Printing technique	Calc. (˚C)	Dens. T (˚C) t (h)	Ceramic precursor	Monomer	Crosslinker	Photo-initiator	Key Novelty	Ref
SLA	600	1300 (47 h)	Silica nanopowder	HEMA	Tetraethylene glycol diacrylate (TEGDA); Trimethylolpropane ethoxylate triacrylate	Diphenyl (2,4,6-trimethylbenzoyl) phosphine oxide; Phenylbis (2,4,6 trimethyl benzoyl) phosphine oxide	High Resolution	[32]
	1000	1250	Silica	2-Hydroxyethyl methacrylate	poly (ethylene glycol) diacrylate 200	2,2-dimethoxy-2-phenylacetophenone (DMPA, 99%)	Luminescent application	[33]
	575	700	Borosilicate	Hydroxyethyl methacrylate (HEMA)	Tetraethylenglycol diacrylate (TEGDA); Trimethylolpropane ethoxylate triacrylate***	Diphenyl (2,4,6-trimethylbenzoyl) phosphine oxide; Phenylbis (2,4,6-trimethyl benzoyl) phosphine oxide***	Low softening temperature materials	[21]
DLP	800	1250 (16 h)	Fumed silica(<100nm)	4-hydroxybutyl acrylate; polyethylene glycol (200) diacrylate	Trimethylolpropane ethoxylate triacrylate	Diphenyl (2,4,6-trimethylbenzoyl) phosphine oxide (TPO)	Effects of sludge parameters on the rheological properties of	[34]
	50 (drying), 800 ˚C	900 - 1100 ˚C (5 d)	TEOS	APTMS (3-acryloxypropyl trimethoxy silane)	-	TPO, 1-hydroxycyclohexyl phenyl ketone, and phenylbis(2,4,6trimethylbenzoyl)phosphine oxide	Use of sol gel precursor	[19]
	500	1000 (26 h)	Triethylphosphate (TEP), Trimethyl borate (TMB), Poly(diethoxysiloxane)	Acrylate monomers Neorad U25-20D (DSM Coating Resins)	Tripropylene glycol diacrylate	TPO((diphenyl(2,4, 6-trimethylbenzoyl)-phosphine oxide,)	Voxel-specific composition, structure and properties based on the phase separable resins)	[35]
3D laser nanolithography		1200	Zirconium n-propoxide,MAPTMS	Methacryloxypropyl trimethoxysilane (MAPTMS,) methacrylic acid	-	4,4′-bis(diethylamino) benzophenone	Nanoscale resolution (Miniaturization (200 nm))	[36]
MPP	600	1300 (46 h)	Commercial Silica nanopowder	Hydroxyethylmethacrylate (HEMA)	Tetraethylenglycoldiacrylate (TEGDA), polyethylenglycoldiacrylate 550	2.2-dimethoxy-2-phenylacetophenone		[37]
CAL	600	1300 (17.2 h)	Glassomer µSL v2.0				Non-layered Single step printing	[38]

2.2 Overview of Vat Photopolymerization process for SiO_2 Glass Manufacture

a. Photopolymerization and Resin systems

For their pioneer disclosure on SLA printing, Charles et al[22] utilized a prepolymer resin mix comprising urethane dimethacrylate, acrylic acid and benzophenone photoinitiator, alongside methyl ethyl hydroquinone triallyl phosphate as inhibitor. Since then materials for VPP are now broadly classified into Free radical systems and Cationic systems depending on the polymerization mechanism of the major monomeric component. The development of polymers from prepolymer resin systems is an exothermic process that may either be step growth (SGP) or chain growth polymerization (CGP). Whereas Step growth polymerization (polycondensation) entails continuous reaction of monomers with themselves in a stepwise manner with the release of small molecules such as H_2O, HCl, NH_3, CH_3OH, etc, chain growth polymerization entails growth of a monomer by continuous addition of monomers to an active chain. The chain growth polymerization which has been widely harnessed for vat polymerization entails an initiation, propagation, chain transfer and termination steps described in table 3 below. First an initiator is dissociated by a light source after which it attacks a monomer, creating an active site, then subsequently monomers add to this site continuously until the termination stages which may be either by combination where two propagating species combine to yield a singular one or disproportionation or chain transfer where the radical on the propagating chain s transferred to non-radical specie or to the solvent. Chain growth polymerization (CGP) is most common for polymerization of vinyl monomers and may be further categorized into Free radical, ionic and coordinate polymerization depending on the initiation source for the polymerization process: radicals, ions and transition metals (and salt complex) catalysts respectively. The tacticity and consequent crystallinity typical for coordination polymerized systems implies that it is not advantageous for ceramic additive manufacturing as rather than undergoing a calcination process, the polymers may first undergo melting resulting in shape distortion of printed structures. For the purpose of this review we focus on free radical and ionic polymerization mechanisms.

Typically, photoresin systems used in stereolithography may comprise of polymerizable monomers, oligomers, photoinitiators, reactive diluents and other additives. For radical polymerization-based systems, photoinitiators determine cure rate, and are required to have a high initial efficiency, good solubility in the prepolymer system, chemical stability and transparency. They are usually molecules with labile bonds such as azos, disulfides, peroxides etc. and may be Norrish Type I (where photochemical reaction is via photocleavage) Or Norrish type II (where photochemical reaction is by hydrogen abstraction). In general monomers are vinyl types such as acrylates, methacrylate and styrene.

In comparison to cationic resin systems, prints resulting from this mechanism exhibit a relatively high shrinkage (>20 %), fast cure rate, poor mechanical properties, high volatility and no dark polymerization[39]. A key issue with radical based systems is their tendency to be inhibited by oxygen due to the formation of intermediate compounds/radicals such as relatively stable peroxides radicals when radical species are oxidized. The coupling of adequate resin degassing[21] with either the use of inert environment, physical barriers as well as high irradiation lamps during printing have been suggested as a means of overcoming this challenge [40]. Ionic polymerization though similar to free radical polymerization utilizes ionic sources as the photoinitiator instead of

Table 2-3: Mechanism of free radical photopolymerization for VPP

Process	Mechanism
Photoinitiation	

(a) Dissociation (b) Association	$\mathbf{I_2} \rightarrow \mathbf{2I}^{\cdot}$ $\mathbf{I}^{\cdot} + \mathbf{M} \rightarrow \mathbf{P_1}^{\cdot}$
Propagation	$\mathbf{P_1}^{\cdot} + \mathbf{M} \rightarrow \mathbf{P_2}^{\cdot}$ … $\mathbf{P_x}^{\cdot} + \mathbf{M} \rightarrow \mathbf{P_{x+1}}^{\cdot}$
Termination (a) Combination (b) Disproportionation	 $\mathbf{P_x}^{\cdot} + \mathbf{P_y}^{\cdot} \rightarrow \mathbf{P_{(x+y)}}$ $\mathbf{P_x}^{\cdot} + \mathbf{P_y}^{\cdot} \rightarrow \mathbf{P_x} + \mathbf{P_y}$
Chain transfer (a) To monomer (b) To solvent	 $\mathbf{P_{(x+1)}}^{\cdot} + \mathbf{M} \rightarrow \mathbf{P_{x+1}} + \mathbf{M}^{\cdot}$ $\mathbf{P_{(x+1)}}^{\cdot} + \mathbf{S} \rightarrow \mathbf{P_{x+1}} + \mathbf{S}^{\cdot}$
$\mathbf{I_2}$ = Photoinitiator, $\mathbf{I}^{\cdot}$ = dissociated photoinitiator molecule M = monomer, $\mathbf{P_x}^{\cdot}$.= propagating polymer radical with x repeat units S = Solvent	

radicals so that the active centers are ions. They may be either cationic such as based on triaryl sulfonium (IX) and diaryliodonium (VIII) salts or anionic such as based on ferrocenes [41]. In the cationic case, photolysis results in the formation of aryl cations which may then initiate polymerization directly or first form Bronsted acids which then react with the monomers. Typical monomers here are vinyl ethers [42] and epoxides [43]. Although cationic systems are not affected by oxygen, a challenge with cationic systems is its speed.

There is a comparatively longer time for the initiation and inhibition of the polymerization process so that it exhibits the so-called dark polymerization. Moisture presence also tends to inhibit the polymerization process so that additives which can assist with a controlled termination step are necessary such that propagation does not continue indefinitely. It is usually carried out under low vacuum conditions in the absences of vapor as well as low temperature conditions. Anionic systems are not affected by moisture or oxygen but are yet to be fully explored as there are not much resin systems fully developed currently. Other resin systems include hybrid systems[44] where photocuring is initiated by both initiation processes of radical and cationic polymerization, as well as photoinitiator-free systems have also been reported in recent times [39].

b. Thermal processing (Calcination and Densification)

Calcination also referred to as debinding entails the time and temperature dependent removal process of non-ceramic components such as volatiles, binders, additives and polymer components of a 3D printed composite (green ensemble). This can be carried out either thermally or catalytically and is done in oxygen containing environments unlike in the case of metals where it is done in inert environments. The calcination process can be studied and investigated either by thermal analytical techniques like differential scanning calorimetry (DSC) and thermogravimetric analysis (TGA) or microscopic techniques. For thermal calcination processes, bond chemistry of the binder materials is important for understanding and optimizing the process and efforts are at top gear towards reducing the duration and temperatures for the process. In work by J. Qiu and coworkers for instance, a systematic partial polymerization during printing resulted in evaporation of some residual monomers which were eliminated at temperatures below 100 °C causing a buildup of channels and consequently, a speedy heat treatment process of less than 16 hours. [23].

The calcination process is key because it is at this stage that the printed object may pulverize or breakdown. The fidelity and stability here depend on the calcination protocol as well as the nature of the photocurable sludge. One way to ensure the fidelity of the printed ensemble during calcination is to add dispersants to the liquid glass. Nano-ceramics particles are generally hydrophilic and tend to agglomerate due to strong nearest neighbor attractive forces of particles. In silica nanoparticles for instance, silanol groups generally dominate surfaces. The use of dispersants thus makes these particles into hydrophobic entities before being introduced into the resin matrix, thus, resulting in a uniform homogenous mix that limits the degree of cracking during calcination. In another investigation of the effects of surfactants on the SLA printability of ZrO_2; out of Stearic acid, oleic acid, Disperbyk (an alkylammonium salt) and several other surfactants studied, Disperbyk was shown to exhibit best adaptability for printing [45]. Oleic acid and stearic acid [46] and short chain dicarboxylic acids ($n_c<10$) [47] have also been reported and compared as dispersants for Al_2O_3 in SLA systems. The use of silane coupling agents for silica is well known [48]. This helps to circumvent lots of issues associated with surface chemistry of silica such as silanol etc. Another way is to properly optimize the calcination protocol, ramp rate, and isothermal time and temperature so as to obtain crack free bodies. In work by Wang and coworkers [21], the use of a slow ramping temperature process of 22.5 ˚C/h was utilized to prevent pulverization at high calcination temperatures. Furthermore, a key cost and energy saving would be the replacement of the polymeric component of sludges with biodegradable, water soluble or organo-soluble prepolymers so that the need for thermal calcination is eliminated and ambient biological conditions are harnessed instead. Although this is common with several non-sludge based additive manufacturing, this is yet to be harnessed for VPP as well as for glass additive manufacturing.

Densification (also known as sintering) on the other hand entails the conversion of fine particles into a coalesced solid under temperature and/or pressure at sufficient conditions below that which the material will normally soften or melt (typically between 80 - 96%). In addition to conventional densification processes, Selective Laser, Spark Plasma, Flash, Capacitor discharge, Induction sintering are some current sintering methods which are subject of on-going research for ceramics. In a bid to enhance densification and calcination speed, Shoji Maruo and co-workers, first functionalized SiO_2 nano-particles with an oleic acid complexed polyethyleneimine system and combined this with a pre-polymer resin mix with a comparably reduced number of multifunctional acrylates. The photo-curing process was thus of a dual nature comprising the polymerization of the methacrylates and then a Michael additive reaction between the resulting polymethacrylates and amino functional groups attached to the SiO_2 particles [26]. Figure 2-3(IV) shows the different green ensembles derived for various densification and multifunctional acrylate concentration. The results show that these parameters can be optimized.

2.3 Progress in the VPP technique for SiO_2 Glass Manufacture.

a. Preceramics and Sol Gel Synthesis

A major focus for current research is the use of preceramic polymers in place of pre-polymer-ceramic sludges [49]. Although not much success has been recorded with using this technique for amorphous transparent glass materials, being only a successful thermal treatment step away, we discuss a couple of 3D printed ceramic materials obtained from pre-ceramic polymers fabricated via the TPP technique. Preceramic polymers are macromolecular compounds, which are pyrolyzable under certain environmental conditions (mostly under limited oxygen) into ceramic compounds referred to as polymer derived ceramics, PDCs. These PDCs have a higher degree of purity and exhibit isotropicity in shrinkage compared to ceramics derived from pre-polymer-ceramic sludges. A summary of the various types and structures are shown in Figure 2-4. These preceramic resins include polycarbosilanes and polysiloxanes and their applications in stereolithography have been demonstrated for porous and non-porous ceramics however, the use of these materials is yet to be reported as a singular SiO_2 source for pure, transparent and amorphous glass. Farsari and coworkers reported that when photocurable liquid glass ensemble comprising germanium isopropoxide and methacryloxypropyl trimethoxysilane were utilized for 3D printing using the DLW-2PP technique, the resulting Germanium silicate structures were optimized, yielding good optical and low shrinkage properties [50]. Other works have yielded silicon oxycarbide [28][51] and silicon carbon-nitride [52][53] and silicon carbide glasses [54] rather than pure silica glasses after pyrolysis as a result of the thermal treatment environment and atomic composition of the preceramics.

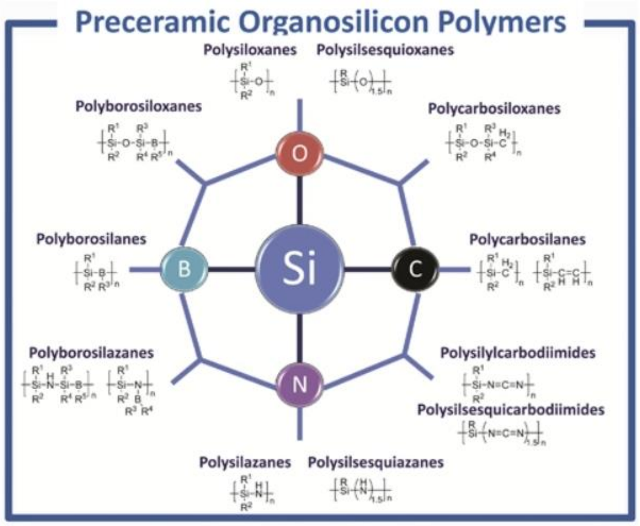

Figure 2-4: Types, structure and atomic composition of Preceramic Organosilicon polymers [55].

Preceramic SiO_2 based materials (organically modified ceramics) have been reported for application as scaffolds in cell [56], drug delivery [57] etc. Application of preceramics in VPP techniques imply that the preceramics should possess photosensitive moieties or there will be a need to combine with photoinitiators to have photocurable sludges. Additionally, preceramics produce very low ceramic yields as the photocurable side groups or component are decomposed during the process. Furthermore, the crosslinking obtained from these side groups (most times acrylic content) are decomposed during the calcination process so that there is most times a pulverization of the printed structure. Development of high ceramic yield photocurable preceramic polymers via structural modification, and combination with non-photocurable preceramics thus forming an interpenetrating cross linked network have been proposed to cater for both issues [49].

The use of sol gel synthesis instead of the currently used fumed silica has now been reported for DIW of glass [58]. Prior to this additive manufacturing report, a patent where sol gel technique had been used in fabricating doped non- transparent, ceramic structures coupled with a template method had been reported.[59] The sol gel technique helps to overcome the difficulty in handling, nanosafety issues as well as particle agglomeration associated with fumed silica nanoparticles [60]. The sol gel synthesis, which entails the hydrolysis of alkoxide precursors is well known to yield nanoparticles with good homogeneity, and allows for controllable porosity and crystallinity. YAG-Ce lumps derived from co-precipitation which first needed to be subjected to impurity-generating ball-milling process before being used with resins in stereolithography and then debinded to yield ceramic structures was reported by Korjik and coworkers [61]. The glass products here were however polycrystalline and translucent. In work by Lue and coworkers, the viscosity of the pre-polymer-ceramic sludge was reduced by carrying out multistep mixing instead of single step mixing and this helped to reduce the viscosity of the liquid glass and made it more adaptable for printing [34]. In work by Wang and coworkers, DLP of a sol-gel mix, was used to manufacture Er^{3+}/Yb^{3+} co-doped phosphosilicate glass with introduction of dopants in the liquid glass state. The EDX data showed uniform distribution of the dopants, the luminescence spectra were consistent with expected spectra for Er^{3+}/Yb^{3+} doped systems and the transparency and amorphousness of the glass were also confirmed [62].

Three dimensional printing of sol–gel based materials using DLP was first carried out by Magdassi and coworkers [19], to fabricate glass structures (Figure 2-5). Here, hybrid UV-curable materials based on silanes modified organically were used as the photopolymerizable agents. A sol gel-based hybrid sludge was prepared where silanes were combined under acidic conditions. Porous and miniature structures were demonstrated. Whereas Figure 2-5(a-c) sows the structure on the print head and after detachment, Figure 2-5d and 5e show the effect of solvent and photopolymerizable agents on density at different temperatures.

In work by Sokolov and coworkers, the introduction of MAPTMS into their sol gel mixture of TMOS and MTMS resulted in a photocurable sludge with an RI of 1.46 which was then subjected to the so called Fast-Sol Gel process. This resultant sludge was successfully utilized in printing structures using the DLP techniques [63]. Their work showed that the sludge can be further improved to make its application in other types of 3D printing systems. In work by Malinauskas and coworkers, an ultrafast 3D lithographic system was utilized in fabricating miniature structures based on hybrid sol–gel resin precursors

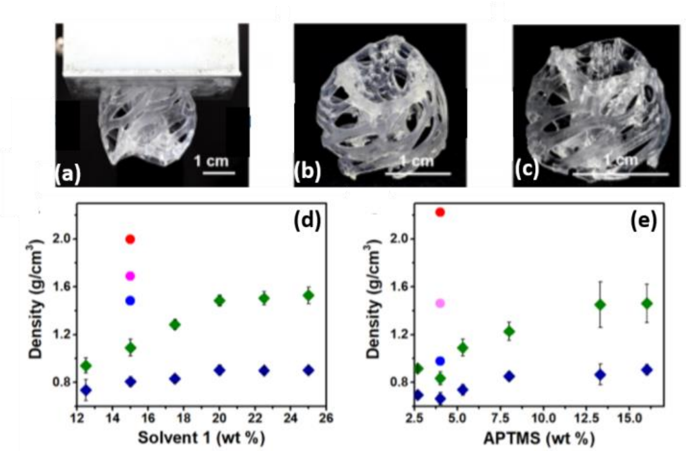

Figure 2-5: DLP printed sol gel structure (a) after printing (b) after drying and removal of solvent at 50 ˚ C (c) After thermal treatment at 800 ˚C (d)Dependence of DLP silica glass densification on (d) solvent and (e) 3- acryloxypropyl trimethoxysilane (APTMS) fraction. The blue diamond, green diamond, blue circle, pink circle, red circle, represent 50 °C, 800 °C, 900 °C, 950 °C and 1100 °C respectively. Reproduced from [19].

coupled with thermal protocol that yielded a crystalline followed by thermal treatment resulted in the formation of crystalline glass [36].

b. Doping

This entails the deliberate inculcation of impurities into a material to attain desired properties for functional applications. Typical dopants include for glass include oxides such as boron oxide, cerium oxide, other rare earth oxides etc. With VPP for ceramic glasses, dopants can be introduced directly into the filler material or the liquid photocurable sludge or after calcination or after densification. Work reported by Qiu and coworkers show the steps in doping (introduced in the brown body state) as well as resultant glass products for luminescence applications [23] whereas work by Korjik and coworkers on Cerium doped Yttrium Aluminum Garnet have also demonstrated doping(introduced in the liquid glass state) [61]. In work by Maruo and co-workers, surface modifiers utilized on the silica nanoparticles were first doped with metal salts after which the silica nanoparticles were then treated with resulting complex [26]. In the case of scintillator applications for example, prior to additive manufacturing, several other approaches such as work by Francini and coworkers [64] which entailed doping sol gel, and densification of the obtained xerogel and also work by Zhou et al. [65] which entailed impregnating of nano-porous already made glass to yield scintillator have been used but these do not offer the advantages that additive manufacturing presents. In addition, the latter will typically yield a non- homogenous glass ensemble. VPP for ceramic glasses allow for a flexibility that dopants may be introduced either before printing, after calcination or even after densification. The possibility for this in SLA was shown by Rapp and coworkers [32] where calcined ensembles were immersed in liquid solutions of ethanol and colored salts resulting in colored glasses, whereas for DIW, the introduction of GeO_2 and TiO_2 into SiO_2 matrices using two independent sludge nozzles have recently been reported [17][66]. The applications to functional glass materials in embedded optics and gradient index optics is still being researched upon and has only been reported for DIW thus far [67].

c. Miniaturization

Asides DIW [17] and VPP [32], High resolution 3D glass structures via additive manufacturing have also been recently demonstrated via a laser PBF (selective laser melting) [68]. This had been hitherto limited to single layer thicknesses [11], [69]–[71]. Here a soda lime glass was 3D printed Figure 2-6(I), shows exemplary structures of soda lime glasses with micro-dimensional features printed with this technique. Although the structures were shown to be amorphous, the often necessity for relatively high temperatures and uncertainty about the optical transmittance properties when utilizing this technique, makes the sludge based DIW and VPP preferable techniques. The relatively easy tunability of filament extrusion as well as shrinkage have been harnessed for miniaturization using the DIW technique. Figure 2-6(II) exemplary 3-d glass structures demonstrated by Dylla-Spears and co-workers. However, the relatively long post printing stage implies the need for more improvement of the technique as well as looking towards other techniques such as VPP. Miniaturization of glass products via photopolymerization have largely entailed modified SLA and DLP systems. The z-resolution is a function of the sludge chemistry, whereas the xy resolution depends on the laser diameter. Current research has focused on modified SLA systems to obtain miniature parts. Work by Rapp and coworkers shows some components designed in addition to refractive index matching of the pre-polymer-ceramic sludges which is key for high resolution structures. In additive manufacturing for SiO_2 glass, Rapp and coworkers [32] utilized a nanocomposite of 40 nm fumed silica consisting, a three step calcination and 2 step densification process (1300 ˚C) to fabricate non-porous, amorphous transparent glass with minimal roughness. By increasing the amount of cross linker, using high molecular weight acrylates, eliminating the solvent and optically index-matching the resin and nanoparticles, a transmission of about 66 % was attained at 365 nm so that miniaturization and high-resolution structures were possible. Rapp and coworkers also

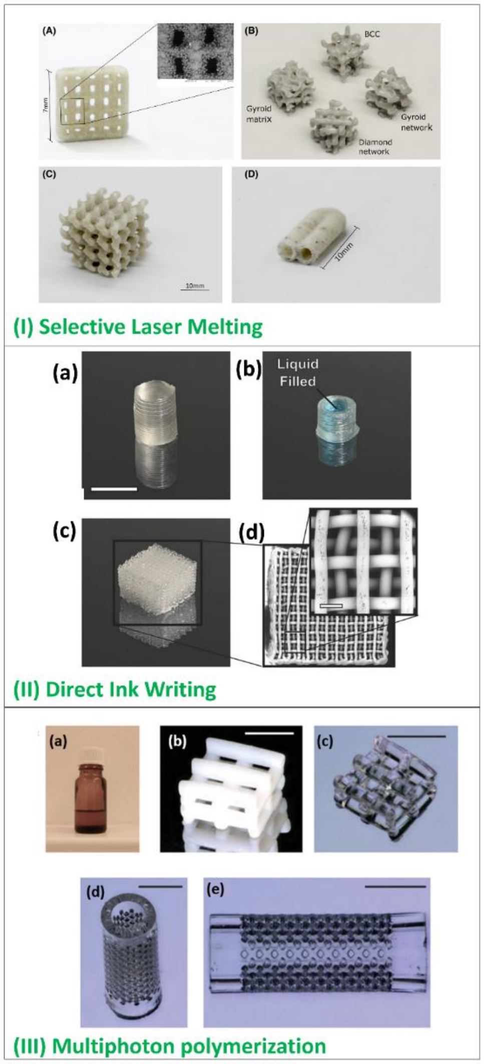

Figure 2-6: (I): 3D printed amorphous glass structures printed via selective laser melting: (a) Actual and Scanning electron micrograph image of a square mesh (b) Actual view of cubic centimeter miniature lattice structures (c) Actual view of an 8 cubic centimeter Gyroid network lattice structure (d) actual view of a reactor channel (1 mm radius). Reproduced from [68]. (II): 3D printed amorphous glass structures printed via DIW. a) Actual view of a solid cylinder. (Scale bar 5 mm). b) Actual view of a blue liquid filled hollow cylinder c) Actual view of a scaffold (d) Scanning electron micrograph of the scaffold in (c). Scale bar 250 µm. Reproduced from [17]. (III) (a) nanocomposite resin used for MPP of fused silica glass structures. Fused silica glass logpile structures fabricated via MPP (after printing) (b) as printed (c) after sintering (scale bars: 500 µm). Microfilter fused silica structures with of 55 µm pore sizes (scale bars: 500 µm). (d) top view (e) side view. Reproduced from [73].

show some miniatures structures as well as the resin sludge utilized for their miniature printing process. Work by Hayden Taylor and coworkers have also recently demonstrated that using a Glassomer µSLA comprising silica nanoparticles and hydroxyethylmethacrylate, alongside a µCAL 3D printer, transparent silica structures of about 50 µm resolution with good mechanical, optical and morphological properties were possible for fused silica glass in a single layer by layer independent step[38]. For VPP with much higher resolutions (<5 um) the TPP photon polymerization could typically be utilized. The TPP technique is a maskless 3D printing process that entails the use of femtosecond laser pulses which cause the absorption of two photons simultaneously, thus, initiating the polymerization process which has the possibility of producing structures having resolutions as high as 100 nm [72]. Rapp and coworkers have recently shown the possibility for this technique in manufacturing miniature glass structures. Their utilization of a unique resin nanocomposite, resulted in fused silica glass structures in the micrometer resolution range as well as comparatively low surface roughness as illustrated in the Figure 2-6(III) [73].

2.4 Machine Learning and Artificial Intelligence

In this era of the fourth industrial revolution, the importance of ML and AI which entail automating tasks with enough pre-existing data helps to eliminate several associated wasteful trial and error(arbitrary) procedures and are thus crucial for more efficient manufacturing processes [74]–[76]. Although ML and AI methods find relevance in both the 3D printing and the post-3D printing process of the VPP techniques for glasses, this review will zero in on the 3D printing part only. The role of ML and AI in additive manufacturing allows for the evaluation of digital CAD designs before printing and testing thereby causing a reduction in cost as well as time spent in experimental trial and error and this has been described in several review works [77]–[85]. They are relevant for process quality control of the eventual printed green structures as well as optimization during the Computer aided design process and photocuring process. It is at the CAD stage that the decisions on print orientation and support structures are made. These are of paramount importance for glass as the orientation could affect the isotropy as well as mechanical properties of the eventually sintered glass. Overhangs beyond 1 mm thicknesses or inclinations beyond 19˚ generally require support structures and these need to be optimally positioned so as to minimize the challenges associated with detachment. McComb and coworkers have recently reported that the Convolution neural Network technique is more reliable than the Regression model for predicting build orientation (for Material Extrusion) during design [86] whereas Wang and coworkers utilized a Double-Layered Extreme Learning Machine (DL-ELM) to train their perceptual model so that preferential print orientation as well as support positioning and area are ascertained. ML algorithms for classification and analysis of features have been reported by Harik and coworkers, Bi and coworkers as well as Kalidindi coworkers [87]–[89]. Other key reports on developments of Machine learning algorithms for additive manufacturing potentially relevant to glass manufacturing have focused on optimizing the mechanical property of the printed structure, surface roughness [90], stress [91], [92], shrinkage, laser power, printing speed [93], layer thickness, in-situ monitoring [94] etc.

2.5 Applications

Key applications of VPP for glass include microfluidics where the miniaturization advantage is harnessed to fabricate glass structures with better optical and mechanical properties compared to the commonly utilized Polydimethylsiloxane (PDMS) and polystyrene [95], optical components requiring tuning or gradation of refractive indices; bijou, figurines where the flexibility for doping is harnessed for color and esthetics tuning [96]. For macro-scale applications, additive manufacturing of optical fibers [97], use in the aerospace industry [7], where factors including functional gradation and on demand manufacturing are increasingly being desired, public infrastructure where harsh weather conditions may be inevitable such as housing and bridges etc. [98].

The applications of VPP also consists of systems where their advantages of high resolution and minimal roughness can be harnessed. They include macro and micro optical systems, light, illumination and luminescent systems, sensing systems etc. For macro optical systems, these may include for printing complicated light guiding optical systems, which allow for spatial resolution of light into wavelengths, 3D displays as well as lens systems[99], [100]. With regards to the later, manufacturing of gradient refractive index lenses[44] doublets[101] refractive panoramic lenses [102], [103] etc. are conventionally being fabricated from polymeric and composite structures at the moment. The advantages of glass over polymers could be harnessed by a replacement and the VPP makes this fabrication process much easier. Applications for micro optical systems include for collimation of light beams [104], [105] solar cells [106] or cameras [107], [108] microscopy [109], etc. The reduction of spherical aberrations as well as migration towards more durable materials such as glasses make the VPP very relevant. Conventional fabrication methods for micro lenses currently include lithography [110], [111] and melting photoresist [112] which are complicated for 3D structures. Applications for light sources may include LEDs [113]–[115], additively manufactured optical converter [116], photoluminescent optics [21] etc. The several conventional techniques currently in use especially for polymer-based systems can be readily replaced by glasses fabricated by VPP.

2.6 Outlook and Conclusion

This review has encompassed a background and summary of current trends with regards to mechanisms, techniques and materials for vat based photopolymerization of glass materials. Modern day research advances in the field for transparent glass ceramics such as the use of alternative sol gel and preceramic precursors, doping, miniaturization as well as machine learning are discussed to yield an overview of the state of art as well as future trends. In general, current challenges with VPP have been widely treated as fields of opportunities where very recent advances have sprung up from. For instance, the disadvantages of utilizing nanoparticles have now been overcome by adopting the sol gel technique Similarly, current reports have shown that pulverization during thermal treatment, deformation and waste resulting from support structures etc. have also been overcome. The future of additive manufacturing encompasses improved efficiency of the fabrication processes, exploration of novel application areas as well as cost in addition to improvement in the overall quality and properties of the printed structures. Further approaches to additive manufacturing of SiO_2 glass in recent times have included focus on materials selection for prepolymer-ceramic sludge mix and modification of the 3D printing set ups as well as improving the speed of the post printing processes. Another key area of research includes fabrication of functional glass materials by the inculcation of dopants into the silica glass matrix. The extension of this vat techniques to low softening temperature ceramics such as borosilicates, borophosphosilicates, soda lime glasses etc. is yet to be fully explored. These ceramics have softening temperatures which lie in close proximity with the typical degradation temperature of the polymer matrix resulting in some difficulties as there is an overlap between their densification temperature region and the calcination step (my paper). There is thus a need for proper selection of prepolymer resins which could result in polymers that have much lower degradation temperatures such as several epoxides or an optimization of the current process to allow for good quality glass products. The extensive drying, calcination and densification time typically over 20 hours in SLA and 110 hours for DIW can be reduced by selecting and inculcating densification aids into the sludge or choosing a solvent with a lower drying rate in the case of DIW. However, the effect of these densification aids on the optical properties and rheology of the sludge need to be first optimized to allow for easy printability. Reports on this are not yet available.

In summary, additive manufacturing is now at a point where functional glass materials can be fabricated with enhanced and more efficient methods and amenable sludge formulations. Future breakthroughs depend on selection of sludge formulations (photo-initiators, monomers, oligomers, additives etc. and precursor ceramic fillers etc.), index matching with the right viscosity and minimized light scattering. Multimaterial printing and miniaturization are now possible even though significant challenges still remain to be overcome for scale up and industrial applications. Methods for thermal treating pre-ceramic resins in such a way as to allow for the elimination of all organic components including carbon without leading to a collapse of the printed structure still need to be explored. Resolving the challenge of shape distortion, anisotropic shrinkage and pulverization of structures associated with the TPP process for pre-ceramic materials in addition could result in its application for materials in various applications as well as fabrication of highly complex, on-demand and customized and hard to machine structures.

2.7 Reference

[1] J. F. D. Carl R. Deckard, Joseph J. Beaman, "Method for selective laser sintering with layerwise cross-scanning - US5155324A," 1990.

[2] N. Travitzky *et al.*, "Additive manufacturing of ceramic-based materials," *Adv. Eng. Mater.*, vol. 16, no. 6, pp. 729–754, Jun. 2014.

[3] S. Singh, S. Ramakrishna, and R. Singh, "Material issues in additive manufacturing: A review," *J. Manuf. Process.*, vol. 25, pp. 185–200, Jan. 2017.

[4] J. Deckers, J. Vleugels, and J. P. Kruth, "Additive manufacturing of ceramics: A review," *J. Ceram. Sci. Technol.*, vol. 5, no. 4, pp. 245–260, 2014.

[5] Z. Chen *et al.*, "3D printing of ceramics: A review," *J. Eur. Ceram. Soc.*, vol. 39, no. 4, pp. 661–687, Apr. 2019.

[6] L. C. Hwa, S. Rajoo, A. M. Noor, N. Ahmad, and M. B. Uday, "Recent advances in 3D printing of porous ceramics: A review," *Curr. Opin. Solid State Mater. Sci.*, vol. 21, no. 6, pp. 323–347, Dec. 2017.

[7] T. D. Ngo, A. Kashani, G. Imbalzano, K. T. Q. Nguyen, and D. Hui, "Additive manufacturing (3D printing): A review of materials, methods, applications and challenges," *Compos. Part B Eng.*, vol. 143, pp. 172–196, Jun. 2018.

[8] J. Klein *et al.*, "Additive Manufacturing of Optically Transparent Glass," *3D print. Addit. Manuf.*, vol. 2, no. 3, pp. 92–105, 2015.

[9] R. F. Shepherd *et al.*, "Stop-flow lithography of colloidal, glass, and silicon microcomponents," *Adv. Mater.*, vol. 20, no. 24, pp. 4734–4739, Dec. 2008.

[10] F. Klocke, A. Mcclung, and C. Ader, “Direct laser sintering of borosilicate glass,” *Proc. Solid Free. Fabr. Symp.*, pp. 214–219, 2004.

[11] M. Fateri and A. Gebhardt, “Selective Laser Melting of Soda-Lime Glass Powder,” *Int. J. Appl. Ceram. Technol.*, vol. 12, no. 1, pp. 53–61, Jan. 2015.

[12] B. Rapp; F. Kotz, “Composition and method for producing a molded body from a highly pure, transparent quartz glass by means of additive manufacturing - US10954155B2,” 2017.

[13] J. Cesarano III; P. D. Calvert, “Method for freeforming objects with low-binder slurry - US6401795B1,” 2000.

[14] G. M. Gratson *et al.*, “Direct-Write Assembly of Three-Dimensional Photonic Crystals: Conversion of Polymer Scaffolds to Silicon Hollow-Woodpile Structures,” *Adv. Mater.*, vol. 18, no. 4, pp. 461–465, Feb. 2006.

[15] C. M. Larson *et al.*, “Direct Ink Writing of Silicon Carbide for Microwave Optics,” *Adv. Eng. Mater.*, vol. 18, no. 1, pp. 39–45, Jan. 2016.

[16] K. Sun, T. S. Wei, B. Y. Ahn, J. Y. Seo, S. J. Dillon, and J. A. Lewis, “3D printing of interdigitated Li-ion microbattery architectures,” *Adv. Mater.*, vol. 25, no. 33, pp. 4539–4543, Sep. 2013.

[17] D. T. Nguyen *et al.*, “3D printing: 3D printed Transparent Glass,” *Adv. Mater.*, vol. 29, no. 26, p. 1701181, 2017.

18] R. D. Farahani, M. Dubé, and D. Therriault, “Three-Dimensional Printing of Multifunctional Nanocomposites: Manufacturing Techniques and Applications,” *Adv. Mater.*, vol. 28, no. 28, pp. 5794–5821, Jul. 2016.

[19] I. Cooperstein, E. Shukrun, O. Press, A. Kamyshny, and S. Magdassi, “Additive Manufacturing of Transparent Silica Glass from Solutions,” *ACS Appl. Mater. Interfaces*, vol. 10, no. 22, pp. 18879–18885, Jun. 2018.

[20] J. Serbin, B. N. Chichkov, and R. Houbertz, “Three-dimensional nanostructuring of hybrid materials by two-photon polymerization,” *Nanocrystals, Org. Hybrid Nanomater.*, vol. 5222, p. 171, Nov. 2003.

[21] O. Okpowe, V. Drozd, O. Ares-Muzio, N. Pala, and C. Wang, “Additive manufacturing of borosilicate glass via stereolithography,” *Ceram. Int.*, vol. 48, no. 9, pp. 12721–12728, Jan. 2022.

[22] C. W. Hull and C. Arcadia, “Apparatus for production of three-dimensional objects by stereolithography,” vol. US492940, Aug. 1984.

[23] C. Liu, B. Qian, X. Liu, L. Tong, and J. Qiu, “Additive manufacturing of silica glass using laser stereolithography with a top-down approach and fast debinding,” *RSC Adv.*, vol. 8, no. 29, pp. 16344–16348, Apr. 2018.

[24] F. B. Löffler, E. C. Bucharsky, K. G. Schell, S. Heißler, and M. J. Hoffmann, “Development of silica based organic slurries for stereolithographic printing process,” *J. Eur. Ceram. Soc.*, vol. 40, no. 13, pp. 4556–4561, Oct. 2020.

[25] L. He, F. Fei, W. Wang, and X. Song, “Support-Free Ceramic Stereolithography of Complex Overhanging Structures Based on an Elasto-viscoplastic Suspension Feedstock,” *ACS Appl. Mater. Interfaces*, vol. 11, no. 20, pp. 18849–18857, May 2019.

[26] R. Arita *et al.*, “Rapid three-dimensional structuring of transparent SiO_2 glass using interparticle photo-cross-linkable suspensions,” *Commun. Mater. 2020 11*, vol. 1, no. 1, pp. 1–7, May 2020.

[27] J. L. Hornbeck, “Multi-level digital micromirror device - US5583688A,” Dec. 1993.

[28] J. Schmidt, L. Brigo, A. Gandin, M. Schwentenwein, P. Colombo, and G. Brusatin, “Multiscale ceramic components from preceramic polymers by hybridization of vat polymerization-based technologies,” *Addit. Manuf.*, vol. 30, p. 100913, Dec. 2019.

[29] B. E. Kelly, I. Bhattacharya, H. Heidari, M. Shusteff, C. M. Spadaccini, and H. K. Taylor, “Volumetric additive manufacturing via tomographic reconstruction,” *Science*, vol. 363, no. 6431, pp. 1075–1079, 2019.

[30] M. Mader *et al.*, “Melt-Extrusion-Based Additive Manufacturing of Transparent Fused Silica Glass,” *Adv. Sci.*, vol. 8, no. 23, p. 2103180, Dec. 2021.

[31] J. Luo, L. J. Gilbert, C. Qu, R. G. Landers, D. A. Bristow, and E. C. Kinzel, “Additive Manufacturing of Transparent Soda-Lime Glass Using a Filament-Fed Process,” *J. Manuf. Sci. Eng. Trans. ASME*, vol. 139, no. 6, p. 061006, Jun. 2017.

[32] F. Kotz *et al.*, “Three-dimensional printing of transparent fused silica glass,” *Nature*, vol. 544, no. 7650, pp. 337–339, 2017.

[33] C. Liu, B. Qian, R. Ni, X. Liu, and J. Qiu, “3D printing of multicolor luminescent glass,” *RSC Adv.*, vol. 8, no. 55, pp. 31564–31567, Sep. 2018.

[34] P. Cai *et al.*, “Effects of slurry mixing methods and solid loading on 3D printed silica glass parts based on DLP stereolithography,” *Ceram. Int.*, vol. 46, no. 10, pp. 16833–16841, Jul. 2020.

[35] D. G. Moore, L. Barbera, K. Masania, and A. R. Studart, “Three-dimensional printing of multicomponent glasses using phase-separating resins,” *Nat. Mater.*, vol. 19, no. 2, pp. 212–217, Feb. 2020.

[36] D. Gailevičius, V. Padolskytė, L. Mikoliūnaitė, S. Šakirzanovas, S. Juodkazis, and M. Malinauskas, “Additive-manufacturing of 3D glass-ceramics down to nanoscale resolution,” *Nanoscale Horizons*, vol. 4, no. 3, pp. 647–651, Apr. 2019.

[37] F. Kotz *et al.*, “Two-Photon Polymerization of Nanocomposites for the Fabrication of Transparent Fused Silica Glass Microstructures,” *Adv. Mater.*, vol. 33, no. 9, p. 2006341, Mar. 2021.

[38] J. T. Toombs *et al.*, “Volumetric additive manufacturing of silica glass with microscale computed axial lithography,” *Science (80-.).*, vol. 376, no. 6590, pp. 308–312, Apr. 2022.

[39] S. C. Ligon, R. Liska, J. Stampfl, M. Gurr, and R. Mülhaupt, “Polymers for 3D printing and Customized Additive Manufacturing,” *Chem. Rev.*, vol. 117, no. 15, pp. 10212–10290, Aug. 2017.

[40] C. E. Hoyle, “An Overview of Oxygen Inhibition in Photocuring,” *Tech. Conf. Proceedings-UV EB Technol. Expo Conf. Charlotte, NC, United States*, p. 104, 2004.

[41] Y. Yamaguch, B. J. Palmer, C. Kutal, T. Wakamatsu, and D. B. Yang, “Ferrocenes as Anionic Photoinitiators,” *Macromolecules*, vol. 31, no. 15, pp. 5155–5157, Jul. 1998.

[42] U. Bulut and J. V. Crivello, “Reactivity of oxetane monomers in photoinitiated cationic polymerization,” *J. Polym. Sci. Part A Polym. Chem.*, vol. 43, no. 15, pp. 3205–3220, Aug. 2005.

[43] U. Bulut and J. V. Crivello, “Investigation of the reactivity of epoxide monomers in photoinitiated cationic polymerization,” *Macromolecules*, vol. 38, no. 9, pp. 3584–3595, May 2005.

[44] O. Okpowe, A. Durygin, V. Drozd, T. Olowu, N. Pala, and C. Wang, “Hybrid Polymers for Gradient Refractive Index Lens,” *2021 IEEE Photonics Conf. IPC 2021 - Proc.*, pp. 1–2, 2021.

[45] J. Sun, J. Binner, and J. Bai, “Effect of surface treatment on the dispersion of nano zirconia particles in non-aqueous suspensions for stereolithography,” *J. Eur. Ceram. Soc.*, vol. 39, no. 4, pp. 1660–1667, Apr. 2019.

[46] K. Li and Z. Zhao, “The effect of the surfactants on the formulation of UV-curable SLA alumina suspension,” *Ceram. Int.*, vol. 43, no. 6, pp. 4761–4767, Apr. 2017.

[47] S. Zhang, N. Sha, and Z. Zhao, “Surface modification of α-Al_2O_3 with dicarboxylic acids for the preparation of UV-curable ceramic suspensions,” *J. Eur. Ceram. Soc.*, vol. 37, no. 4, pp. 1607–1616, Apr. 2017.

[48] M. Myers, “Current State-of-the-Art and Impending Developments of Silica Nanoparticle Use in UV-Curable Systems,” *RadTech 2010 Tech. Conf.*, p. 1530, 2010.

[49] J. Schmidt and P. Colombo, “Digital light processing of ceramic components from polysiloxanes,” *J. Eur. Ceram. Soc.*, vol. 38, no. 1, pp. 57–66, Jan. 2018.

[50] M. Malinauskas *et al.*, “3D microoptical elements formed in a photostructurable germanium silicate by direct laser writing,” *Opt. Lasers Eng.*, vol. 50, no. 12, pp. 1785–1788, Dec. 2012.

[51] J. Bauer *et al.*, “Additive Manufacturing of Ductile, Ultrastrong Polymer-Derived Nanoceramics,” *Matter*, vol. 1, no. 6, pp. 1547–1556, Dec. 2019.

[52] T. W. Lim *et al.*, “Net Shape Manufacturing of Three-Dimensional SiCN Ceramic Microstructures Using an Isotropic Shrinkage Method by Introducing Shrinkage Guiders,” *Int. J. Appl. Ceram. Technol.*, vol. 5, no. 3, pp. 258–264, May 2008.

[53] T. A. Pham, D. P. Kim, T. W. Lim, S. H. Park, D. Y. Yang, and K. S. Lee, “Three-Dimensional SiCN Ceramic Microstructures via Nano-Stereolithography of Inorganic Polymer Photoresists,” *Adv. Funct. Mater.*, vol. 16, no. 9, pp. 1235–1241, Jun. 2006.

[54] T. W. Lim *et al.*, “Fabrication of three-dimensional SiC-based ceramic micropatterns using a sequential micromolding-and-pyrolysis process,” *Microelectron. Eng.*, vol. 83, no. 11–12, pp. 2475–2481, Nov. 2006.

[55] P. Colombo, G. Mera, R. Riedel, and G. D. Sorarù, “Polymer-Derived Ceramics: 40 Years of Research and Innovation in Advanced Ceramics,” *J. Am. Ceram. Soc.*, vol. 93, no. 7, pp. 1805–1837, Jul. 2010.

[56] L. A. Gerasimova, “Interferometric measurement of the refractive-index gradient distribution in gradient-index optical blanks,” *Appl. Opt.*, vol. 35, no. 16, p. 2997, Jun. 1996.

[57] S. H. Ahn, J. Lee, S. A. Park, and W. D. Kim, “Three-dimensional bio-printing equipment technologies for tissue engineering and regenerative medicine,” *Tissue Eng. Regen. Med. 2016 136*, vol. 13, no. 6, pp. 663–676, Dec. 2016.

[58] J. F. Destino *et al.*, "3D printed Optical Quality Silica and Silica–Titania Glasses from Sol–Gel Feedstocks," *Adv. Mater. Technol.*, vol. 3, no. 6, p. 1700323, Jun. 2018.

[59] A. Yu-Chung, "Mesoporous membranes with complex functional architectures and methods for making - US8211498B2," Jun. 12, 2009.

[60] D. A. Seleci *et al.*, "Determining nanoform similarity via assessment of surface reactivity by abiotic and in vitro assays," *NanoImpact*, vol. 26, p. 100390, Feb. 2022.

[61] G. A. Dosovitskiy *et al.*, "First 3D printed complex inorganic polycrystalline scintillator," *CrystEngComm*, vol. 19, no. 30, pp. 4260–4264, Jul. 2017.

[62] J. Wang, B. Zheng, and P. Wang, "3D printed Er3+/Yb3+ co-doped phosphosilicate glass based on sol-gel technology," *J. Non. Cryst. Solids*, vol. 550, p. 120362, Dec. 2020.

[63] R. Gvishi and I. Sokolov, "3D sol–gel printing and sol–gel bonding for fabrication of macro- and micro/nano-structured photonic devices," *J. Sol-Gel Sci. Technol.*, vol. 95, no. 3, pp. 635–648, Sep. 2020.

[64] N. Chiodini *et al.*, "Rare-Earth Doped Sol-Gel Silicate Glasses for Scintillator Applications," *Radiat. Eff. Defects Solids Inc. Plasma Sci. Plasma Technol.*, vol. 158, no. 1–6, pp. 463–467, Jan. 2014.

[65] M. Zhou; Y. Qiao; W. Ma, "Rare earth ions doped alkali metal silicate luminescent glass and the preparation method thereof - US9156733B2," Jul. 2010.

[66] K. Sasan *et al.*, "Additive Manufacturing of Optical Quality Germania-Silica Glasses," *ACS Appl. Mater. Interfaces*, vol. 12, no. 5, pp. 6736–6741, Feb. 2020.

[67] R. Dylla-Spears *et al.*, "3D printed gradient index glass optics," *Sci. Adv.*, vol. 6, no. 47, pp. 7429–7447, Nov. 2020.

[68] K. C. Datsiou, E. Saleh, F. Spirrett, R. Goodridge, I. Ashcroft, and D. Eustice, "Additive manufacturing of glass with laser powder bed fusion," *J. Am. Ceram. Soc.*, vol. 102, no. 8, pp. 4410–4414, Aug. 2019.

[69] R. S. Khmyrov, S. N. Grigoriev, A. A. Okunkova, and A. V. Gusarov, "On the Possibility of Selective Laser Melting of Quartz Glass," *Phys. Procedia*, vol. 56, no. C, pp. 345–356, Jan. 2014.

[70] R. S. Khmyrov, C. E. Protasov, S. N. Grigoriev, and A. V. Gusarov, “Crack-free selective laser melting of silica glass: single beads and monolayers on the substrate of the same material,” *Int. J. Adv. Manuf. Technol. 2015 855*, vol. 85, no. 5, pp. 1461–1469, Nov. 2015.

[71] M. Fateri and A. Gebhardt, “Jewelry Fabrication via Selective Laser Melting of Glass,” *ASME 2014 12th Bienn. Conf. Eng. Syst. Des. Anal. ESDA 2014*, vol. 1, p. 20380, Oct. 2014.

[72] K. S. Lee, R. H. Kim, D. Y. Yang, and S. H. Park, “Advances in 3D nano/microfabrication using two-photon initiated polymerization,” *Prog. Polym. Sci.*, vol. 33, no. 6, pp. 631–681, Jun. 2008.

[73] F. Kotz *et al.*, “Two-Photon Polymerization of Nanocomposites for the Fabrication of Transparent Fused Silica Glass Microstructures,” *Adv. Mater.*, vol. 33, no. 9, p. 2006341, Mar. 2021.

[74] J. Butt, “Exploring the Interrelationship between Additive Manufacturing and Industry 4.0,” *Designs*, vol. 4, no. 2, p. 13, Jun. 2020.

[75] A. Haleem and M. Javaid, “Additive Manufacturing Applications in Industry 4.0: A Review,” *J. Ind. Integr. Manag.*, vol. 04, no. 04, p. 1930001, Oct. 2019.

[76] M. A. Kaleem and M. Khan, “Significance of Additive Manufacturingfor Industry 4.0With Introduction of Artificial Intelligence in Additive Manufacturing Regimes,” *Proc. 2020 17th Int. Bhurban Conf. Appl. Sci. Technol. IBCAST 2020*, pp. 152–156, Jan. 2020.

[77] G. D. Goh, · S L Sing, and · W Y Yeong, “A review on machine learning in 3D printing: applications, potential, and challenges,” *Artif. Intell. Rev.*, vol. 54, pp. 63–94, 123AD.

[78] J. Yang, Y. Chen, W. Huang, and Y. Li, “Survey on artificial intelligence for additive manufacturing,” *ICAC 2017 - 2017 23rd IEEE Int. Conf. Autom. Comput. Addressing Glob. Challenges through Autom. Comput.*, pp. 1–6, Oct. 2017.

[79] S. S. Razvi, S. Feng, A. Narayanan, Y. T. T. Lee, and P. Witherell, “A Review of Machine Learning Applications in Additive Manufacturing,” *Proc. ASME Des. Eng. Tech. Conf.*, vol. 1, p. 98415, Nov. 2019.

[80] F. W. Baumann, A. Sekulla, M. Hassler, B. Himpel, and M. Pfeil, “Trends of machine learning in additive manufacturing,” *Int. J. Rapid Manuf.*, vol. 7, no. 4, p. 310, 2018.

[81] D. Grierson, A. E. W. Rennie, S. D. Quayle, R. Agarwal, and G. Ruta, “Machine Learning for Additive Manufacturing,” *Encycl. 2021, Vol. 1, Pages 576-588*, vol. 1, no. 3, pp. 576–588, Jul. 2021.

[82] C. Wang, X. P. Tan, S. B. Tor, and C. S. Lim, “Machine learning in additive manufacturing: State-of-the-art and perspectives,” *Addit. Manuf.*, vol. 36, p. 101538, Dec. 2020.

[83] Z. Jin, Z. Zhang, K. Demir, and G. X. Gu, “Machine Learning for Advanced Additive Manufacturing,” *Matter*, vol. 3, no. 5, pp. 1541–1556, Nov. 2020.

[84] L. Meng *et al.*, “Machine Learning in Additive Manufacturing: A Review,” *JOM*, vol. 72, no. 6, pp. 2363–2377, Jun. 2020.

[85] Y. Bin Wang, P. Zheng, T. Peng, H. Y. Yang, and J. Zou, “Smart additive manufacturing: Current artificial intelligence-enabled methods and future perspectives,” *Sci. China Technol. Sci. 2020 639*, vol. 63, no. 9, pp. 1600–1611, May 2020.

[86] G. Williams, N. A. Meisel, T. W. Simpson, and C. McComb, “Design repository effectiveness for 3D convolutional neural networks: Application to additive manufacturing,” *J. Mech. Des. Trans. ASME*, vol. 141, no. 11, p. 111701, Nov. 2019.

[87] Y. Shi, Y. Zhang, S. Baek, W. De Backer, and R. Harik, “Manufacturability analysis for additive manufacturing using a novel feature recognition technique,” vol. 15, no. 6, pp. 941–952, 2018.

[88] X. Yao, S. K. Moon, and G. Bi, “A hybrid machine learning approach for additive manufacturing design feature recommendation,” *Rapid Prototyp. J.*, vol. 23, no. 6, pp. 983–997, 2017.

[89] M. V. Johnson, K. Garanger, J. O. Hardin, J. D. Berrigan, E. Feron, and S. R. Kalidindi, “A generalizable artificial intelligence tool for identification and correction of self-supporting structures in additive manufacturing processes,” *Addit. Manuf.*, vol. 46, p. 102191, Oct. 2021.

[90] E. Vahabli and S. Rahmati, “Application of an RBF neural network for FDM parts’ surface roughness prediction for enhancing surface quality,” *Int. J. Precis. Eng. Manuf. 2016 1712*, vol. 17, no. 12, pp. 1589–1603, Dec. 2016.

[91] A. K. Sood, R. K. Ohdar, and S. S. Mahapatra, “Experimental investigation and empirical modelling of FDM process for compressive strength improvement,” *J. Adv. Res.*, vol. 3, no. 1, pp. 81–90, Jan. 2012.

[92] A. Khadilkar, J. Wang, and R. Rai, "Deep learning-based stress prediction for bottom-up SLA 3D printing process," *Int. J. Adv. Manuf. Technol.*, vol. 102, pp. 2555–2569, 2019.

[93] H. He, Y. Yang, and Y. Pan, "Machine learning for continuous liquid interface production: Printing speed modelling," *J. Manuf. Syst.*, vol. 50, pp. 236–246, Jan. 2019.

[94] K. Wasmer, C. Kenel, C. Leinenbach, and S. A. Shevchik, "In situ and Real-Time Monitoring of Powder-Bed AM by Combining Acoustic Emission and Artificial Intelligence," *Ind. Addit. Manuf. - Proc. Addit. Manuf. Prod. Appl.*, pp. 200–209, 2017.

[95] M. Mader *et al.*, "Fused deposition modeling of microfluidic chips in transparent polystyrene," *Micromachines*, vol. 12, no. 11, p. 1348, Nov. 2021.

[96] D. Zhang, X. Liu, and J. Qiu, "3D printing of glass by additive manufacturing techniques: a review," *Front. Optoelectron.*, vol. 14, pp. 263–277, 2020.

[97] J. Wang *et al.*, "Silica optical fibre fabrication via 3D printing technology: material processing and related issues," *Eur. Phys. J. Spec. Top. 2021*, pp. 1–12, Dec. 2021.

[98] P. Wu, J. Wang, and X. Wang, "A critical review of the use of 3-D printing in the construction industry," *Autom. Constr.*, vol. 68, pp. 21–31, Aug. 2016.

[99] Y. Zhu *et al.*, "Recent advancements and applications in 3D printing of functional optics," *Addit. Manuf.*, vol. 52, p. 102682, Apr. 2022.

[100] G. M. Williams, H. Akhavan, C. Dupuy, and P. Harmon, "Additive manufacturing of freeform optics for defense applications," *2021 IEEE Res. Appl. Photonics Def. Conf. RAPID 2021*, pp. 1–2, Aug. 2021.

[101] L. D. Vallejo-Melgarejo, R. G. Reifenberger, B. A. Newell, C. A. Narváez-Tovar, and J. M. Garcia-Bravo, "Characterization of 3D printed lenses and diffraction gratings made by DLP additive manufacturing," *Rapid Prototyp. J.*, vol. 25, no. 10, pp. 1684–1694, Nov. 2019.

[102] M. Rank *et al.*, "3D printing of Optics Based on Conventional Printing Technologies," *Springer Ser. Opt. Sci.*, vol. 233, pp. 45–167, 2021.

[103] H. Wang *et al.*, "Panoramic lens designed with transformation optics," *Sci. Reports 2017 71*, vol. 7, no. 1, pp. 1–7, Jan. 2017.

[104] Z. L. Liau, J. N. Walpole, D. E. Mull, C. L. Dennis, and L. J. Missaggia, “Accurate fabrication of anamorphic microlenses and efficient collimation of tapered unstable-resonator diode lasers,” *Appl. Phys. Lett.*, vol. 64, no. 25, p. 3368, Jun. 1998.

[105] B. N. K. Ann, K. S. Seong, and Z. Xiao-qun, “Single aspherical lens for deastigmatism, collimation, and circularization of a laser beam,” *Appl. Opt. Vol. 39, Issue 7, pp. 1148-1151*, vol. 39, no. 7, pp. 1148–1151, Mar. 2000.

[106] O. Fidaner *et al.*, “High efficiency micro solar cells integrated with lens array,” *Appl. Phys. Lett.*, vol. 104, no. 10, p. 103902, Mar. 2014.

[107] R. Stevensa and T. Miyashita, “Review of standards for microlenses and microlens arrays,” *Imaging Sci. J.*, vol. 58, no. 4, pp. 202–212, 2013.

[108] R. Ferreira and N. Goncalves, “Fast and accurate micro lenses depth maps for multi-focus light field cameras,” *Ger. Conf. pattern Recognit.*, vol. 9796, pp. 309–319, 2016.

[109] A. Orth and K. Crozier, “Scanning Confocal Microscopy with A Microlens Array,” *Proc. Front. Opt. 2011/Laser Sci. XXVII*, p. FWS7, 2011.

[110] H. Ottevaere *et al.*, “Comparing glass and plastic refractive microlenses fabricated with different technologies,” *J. Opt. A Pure Appl. Opt.*, vol. 8, no. 7, p. S407, Jun. 2006.

[111] H. Nishihara, J. Koyama, and T. Fujita, “Fabrication of micro lenses using electron-beam lithography,” *Opt. Lett.*, vol. 6, no. 12, pp. 613–615, Dec. 1981.

[112] X. Zeng *et al.*, “The manufacture of microlenses by melting photoresist,” *Meas. Sci. Technol.*, vol. 1, no. 8, p. 759, Aug. 1990.

[113] S. Stolz *et al.*, “One-step additive crosslinking of conjugated polyelectrolyte interlayers: improved lifetime and performance of solution-processed OLEDs,” *J. Mater. Chem. C*, vol. 4, no. 47, pp. 11150–11156, Dec. 2016.

[114] X. Cao, Y. Ye, X. Liu, T. Guo, and Q. Tang, “Realization of uniform oled pixels based on multi-nozzle by inkjet printing,” *Dig. Tech. Pap. - SID Int. Symp.*, vol. 52, no. S1, pp. 395–397, 2021.

[115] C. Eder, M. Rank, and A. Heinrich, “Additive manufactured organic light-emitting

diodes," *Proc. SPIE 11277, Org. Photonic Mater. Devices XXII*, vol. 11277, pp. 8–17, Feb. 2020.

[116] L. Brzozowski and E. H. Sargent, "All-Optical Analog-to-Digital Converters, Hardlimiters, and Logic Gates," *J. Light. Technol.*, vol. 19, no. 1, pp. 114–119, 2001.

3 Additive manufacturing of borosilicate glass via stereolithography

3.1 Introduction

Borosilicate (B-SiO_2) glass consists of SiO_2 and B_2O_3 as network formers and oxide modifiers respectively. Its excellent optical properties such as transparency and tunable refractive index, chemical resistance, low thermal expansivity and tunable chemical composition make it useful for a wide range of applications such as luminescence [1,2]; optical lenses [3]; electrochromism [4], lab ware, medical implants, waste immobilization [5], and other microelectromechanical systems (MEMS). In addition, the high thermal neutron cross-section of boron and high luminescence efficiency of Cerium (Ce) makes Ce-doped borosilicate glass a perfect scintillator material for radiation detection [6–9]. The optical properties of glass fabricated by conventional melt-quenching or high temperature densification approaches depend on the glass fabrication method, precursors and processing conditions for incorporation of Ce into the B-SiO_2 matrix [1]. However, the conventional glass fabrication based on melt-quenching resorts to relatively high temperatures (>1000 ˚C) for melting and also needs reduced environment to ensure the dopant state during the melt and cooling process.

Recently, additive manufacturing of B-SiO_2 ceramics has been demonstrated by various 3D printing techniques such as: selective laser melting (SLM) [10], direct laser sintering (DLS) [11] and fused deposition modeling (FDM). Both SLM and DLS are powder bed fusion techniques where powders are consolidated either by melting or by densification using a high-power density heat source such as a CO_2 laser or electron beams. These glasses were shown to exhibit high porosity and low optical transparency. FDM utilizes a CO_2 laser heat source to generate molten glass from glass filaments [12,13]. Other than its low resolution, the other key challenge with FDM for B-SiO_2 glass formation is the bubble formation resulting from the printing process, which has been shown to be resolvable by carrying out systematic post-annealing [12,13]. Other glass additive manufacturing approaches, such as material extrusion and stop flow lithography [14] have also been reported for SiO_2 glass fabrication with issues of relatively rough surface finishing and difficulty to form complex 3D structure, respectively. More recently, the exploration of sludge based additive manufacturing accompanied by a subsequent heat treatment step at relatively low temperatures have been shown to be a preferable route for glass fabrication as they helped overcome the challenges of melt-quenching [15–18].

The sludge-based technique typically entails either direct ink writing (DIW), digital light processing (DLP) or stereolithography (SLA) and allows for a room temperature printing after which the thermal processing can be carried out usually below the softening temperature of the ceramic material. The DIW technique was first patented for additive manufacturing of ceramics in 2000 by Cesarano et al. [19]. It had been used for 3D printing a wide range of materials such as photonic crystals [20,21] and energy devices [22] until its recent success in 2017 with glass materials [17]. In terms of DIW, the rheological properties of the sludge are tuned in such a way that in the presence of a shear force the viscous liquid flows and thins to maximize the z-resolution of the eventual prints and then stops when the force is removed however, the process is subjected to a relatively long (110 hours) drying, calcination and the densification process. SLA, a VPP technique, invented by Chucks Hall in 1986 on the other hand, typically entails curing a liquid photosensitive pre-polymer resin mixture by an irradiation light source (most commonly UV) [23]. The latter induces a chemical reaction by first attacking the photoinitiator, which in turn reacts with the monomers and oligomers in the mix resulting in a highly cross-linked polymer network. In terms of ceramics printing by SLA, a homogeneous photocurable sludge based on mixing and dispersing of a pre-polymer photosensitive resin mixture with ceramic filler particles can be formed with the aid of surfactants or additives. Recently Rapp and coworkers at KIT have successfully synthesized high-resolution undoped and amorphous pure silica glass by SLA using 40 nm fumed silica particles and high molecular weight acrylate-based resin in a multi-step calcination and densification process (1300 °C) [15,24]. By immersing the brown body in solutions of alcohol and metal salts, they were able to obtain colored glasses with different optical transmission characteristics. Following the pioneer work of KIT there are several other groups developing SLA based process for transparent silica glass manufacturing with noticeable progress towards photovoltaic applications and general process improvement [16]. All these works have demonstrated that SLA is a promising approach for printing fine details and complex geometric structures since the resolution depends on the dimensions of the laser beam. However, several challenges of SLA based glass fabrication have to be further addressed. The rheological properties and optical properties of the sludge and the eventual shrinkage in the final glass product are all dependent on the sludge compositions. The viscosity of commercially available resins is close to 3000 mPas. The typical volumetric composition of sludge (ceramics in the resin) ranges from 30 vol% (low viscosity) to 60 vol % (high viscosity). Higher viscosities could help to maintain the structure stability with lower shrinkage of final products but with the trade-off of light scattering and printability. In addition, refractive index matching of the polymer resin and the ceramic particles is key for higher degree of structure fidelity [25]. Moreover, the relatively low softening temperature (T_s) for B-SiO_2 (~ 711 ˚C) makes the thermal treatment step cumbersome partially because of an overlap of the calcination and densification thermal processing regions.

In the present work, we demonstrate, 3D printed B-SiO_2 glass fabricated via stereolithography with comparable optical properties to commercial B-SiO_2 glass, irrespective of their low softening temperatures. The processing parameters of densification and calcination were optimized to achieve structure stability of the resulting undoped and Ce-doped B-SiO_2 glass. Optical parameters including the optical band gap, Urbach energy and refractive index were deduced from the optical absorption spectra with comparable quality to doped glasses fabricated by conventional melt quench method.

3.2 Experimental Procedure

The glasses were fabricated by first mixing B-SiO_2 7070 (Corning Inc.) with acrylate-based pre-polymer resin-mix comprising hydroxyethyl methacrylate (HEMA) (Sigma Aldrich Inc.), trimethylolpropane ethoxylate triacrylate (Sigma Aldrich Inc.), hydroquinone (Sigma Aldrich Inc.), Tinuvin 384-2 (Ribelin Inc.) and 0.5 wt% of phenylbis(2,4,6-trimethylbenzoyl) phosphine oxide (Sigma Aldrich Inc.) in the ratio of 100:50:7:6:7 by weight, respectively or Formlabs 1+ clear resin (Formlabs Inc.). Some properties of the B-SiO_2 powder, its scanning electron morphology as well as BET surface area morphology and porosity are indicated in Table A1, Figure A1(a) and Figure A1(b) respectively. The composition of the sludge was 40 vol % of the B-SiO_2 particles, printed and then calcined before densification. For the cerium doped glass, cerium (III) acetate sesquihydrate (Fisher Scientific Inc.) was introduced into the sludge at mole ratios varying from 0.1-1 mol % with respect to the B-SiO_2. The individual components of the liquid sludge were mixed before the dispersion using a hotplate stirrer. The resulting sludge was then degassed under vacuum before 3D printing. Detailed description of the prepared samples is summarized in Table 1. For sample nomenclature, the first 3 digits indicate the number of calcination steps, middle digits indicate the maximum calcination temperature and last digits indicate the densification time for undoped samples. Additional post-subscripts indicate either a non-vacuum environment (ambient air) or the volume composition of B-SiO_2 in the sludge. Doped samples are indicated by the chemical symbol of the dopant used (e.g. Ce for Cerium-doped). Table 2 lists the samples following the same nomenclature except that the dopant concentrations for doped samples are indicated as the last two digits in place of the densification times. The green body is the 3D printed body whereas the calcined body is the sample obtained when the green body is subjected to thermal treatment in air to eliminate polymeric components and then the densified body is obtained when the calcined body is subjected to further processing to eliminate porosities and increase density of the sample.

The 3D printing process was carried out using a Formlabs 1+ 3D printer (λ = 405 nm) with an XY-resolution of 300 µm based on custom CAD-designs on a Solid Works software. The lateral and Z-direction resolutions were set to 0.2 mm for all printing. The obtained green body was then detached from their support structures, rinsed in ethanol, post cured using a 15-Watt 365 nm Blak-Ray XX-15BLB UV bench lamp for about 10min before being carefully moved to a furnace for thermal processing. The thermal processing was carried out at calcination and densification temperatures based on Table 1, which described specifics and fabrication conditions of samples. An Isotemp Muffle Furnace (Fisher Scientific) with a rotary pump mounted on it was utilized for these processes.

Scanning Electron Microscopy (SEM), JEOL JSM-6330F field emission SEM-EDS (Tokyo, Japan), was employed to investigate the morphology of the resulting body at various steps of the fabrication process. Energy Dispersive X-ray Spectroscopy (EDS) was used to ascertain the elemental composition of the resulting products. The presence and degree of devitrification of fabricated products were studied by X-ray diffraction (XRD) technique using a Siemens D-5000 X-ray diffractometer (Munich, Germany) which utilizes a copper K_α X-ray source of wavelength 1.54178 Å. The scan rate used was 0.1 degree/min while step size was 0.02 degree.

The surface area and porosities were determined by nitrogen adsorption/desorption isotherms at 77 K using a Tri-Star II Micromeritics and calculated by Brunauer–Emmett–Teller (BET) measurement. Prior to the measurements, all of the samples were degassed at 373 K for 24 h and finally outgassed to 10^{-3} Torr. The Differential Scanning Calorimetry

(DSC) and Thermogravimetric Analysis (TGA) experiments were both carried out using a spectrofluorophotometer.

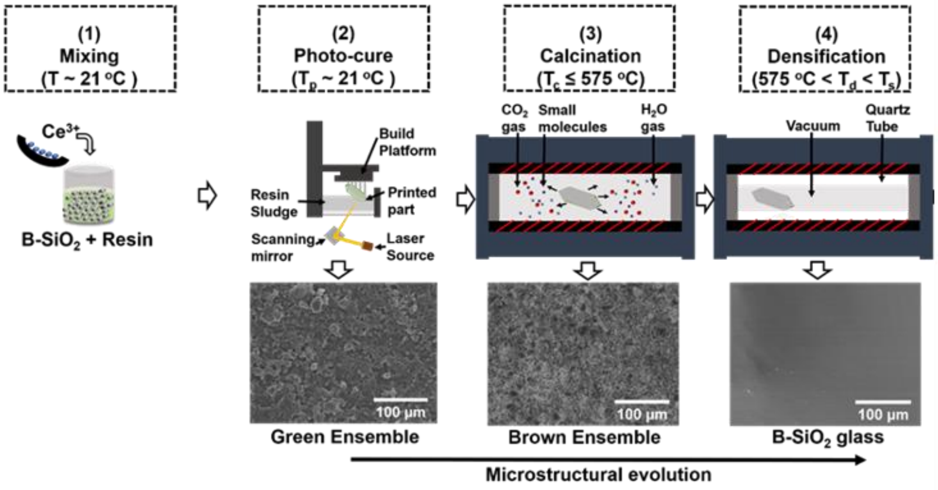

Figure 1.4-1: Illustration of the key steps in the fabrication of 3D borosilicate glass bodies. T_p, T_c, T_d and T_s represent printing, calcination, densification and softening temperatures, respectively. Step (1): Mixing step (and incorporation of Ce dopant); Step (2): Printing and photocuring process of the sludge using the SLA 3D printer; Step (3): Calcination process of the green body in the furnace; Step (4): Densification process of the calcined $B\text{-}SiO_2$ within a vacuumed quartz tube in the furnace. Bottom images show the scanning electron micrographs of the green body (left); calcined body (middle); and the densified body (right).

Table 3-1: Summary of synthesis parameters of 3D printed $B\text{-}SiO_2$ glass samples.

Sample	Sludge $B\text{-}SiO_2$ vol (%)	Calcination						Densification		
		T_{c1}(˚C)	t_{c1}(h)	T_{c2}(˚C)	t_{c2}(h)	T_{c3}(˚C)	t_{c3}(h)	T_d(˚C)	t_d(h)	Environment
(1SC-575-10)$_{40}$	40	-	-	-	-	575	10	700	10	Vacuum
(3SC-575-05)$_{40}$	40	180	5	360	5	575	5	700	5	Vacuum
(3SC-500-10)$_{40}$	40	180	5	360	5	500	5	700	10	Vacuum
(3SC-500-02)$_{40}$	40	180	5	360	5	500	5	700	2	Vacuum
(3SC-600-05)$_{40}$	40	180	5	360	5	600	5	700	5	Vacuum
(3SC-575-10)$_{40}$	40	180	5	360	5	575	5	700	10	Vacuum
(3SC-575-10)$_{40+air}$	40	180	5	360	5	575	5	700	10	Air
(3SC-575-10)$_{20}$	20	180	5	360	5	575	5	700	10	Vacuum
(3SC-575-10)$_{60}$	60	180	5	360	5	575	5	700	10	Vacuum

Simultaneous DSC-TGA (SDT) Q600 instrument. The light transmittance and absorption at different wavelengths of the final densified body are investigated using a Solar Cell Spectral response measurement system (PV measurements, Inc (Model QEX10)) whereas the luminescence properties are investigated by a Shimadzu RF-1501.

Table 3-2: Summary of synthesis parameters of 3D printed B-SiO_2 glasses with different amount of Ce dopant.

Sample	Sludge B-SiO_2 vol (%)	Calcination						Dopant conc. (mol %)	Sample thickness (mm)
		T_{c1}(˚C)	t_{c1}(h)	T_{c2}(˚C)	t_{c2}(h)	T_{c3}(˚C)	t_{c3}(h)		
Ce:3SC-575-02	40	180	5	360	5	575	5	2	1.73
Ce:3SC-575-04	40	180	5	360	5	575	5	4	1.15
Ce:3SC-575-06	40	180	5	360	5	575	5	6	1.39
Ce:3SC-575-08	40	180	5	360	5	575	5	8	2.06
Ce:3SC-575-10	40	180	5	360	5	575	5	10	2.16

3.3 Results and Discussion

The schematic for the entire fabrication process is illustrated in Figure 3-1. First, the Cerium acetate, B-SiO_2 particles and resin mixture are mixed at room temperature after which they are printed and cured with the aid of the SLA printer, calcined and densified. Figure A1(a) shows the scanning electron microscopy image of the as-received B-SiO_2 ceramics powder and this expectedly exhibits particle dimensions <40 µm. From Figure A1(b) it is evident from the BET measurement that there is a complete absence of porosity in B-SiO_2 sample unlike compared to commercial SBA-15 whose pore size and distribution is well established. We also estimate the surface area to be 282.01 m^2/g as presented in Table A1. Figure A2 shows a Computer Aided designed structure and some printed structures before calcination. The exemplary resulting densified glass samples for different particle loading in the liquid sludge body used for printing are shown on the Figure A-3. For a 20 % particle loading by volume, there is an expectedly observed distorted opaque structure signifying a too low loading. However, the optical clarity increases with increasing loading due to decreasing degree of porosity. SEM images of the printed, calcined, and densified samples are also shown in Figure 3.1. There is a high degree of porosity after calcination, which is as a result of the complete elimination of the polymeric component of the printed body, but this porosity is absent at the end of the densification process.

For the thermal analysis of B-SiO_2 powder (control sample) and B-SiO_2-resin green body sample ($(3SC\text{-}575\text{-}10)_{20}$) investigated and shown in Figure 3.2(a), the temperature heat flow profile alongside a corresponding decomposition of the green body as a function of temperature for a ramping of 10 °C/min is presented. The DSC plot shows the heat flow versus temperature behavior of the borosilicate particles where the softening temperature for the B-SiO_2 glass is observed to be at 711 °C with an exothermic peak. For the degradation of $(3SC\text{-}575\text{-}10)_{20}$, initially there is a super-slow process (region I) where weight is constant up to 250 °C implying complete curing and absence of residual monomers or oligomers within the body structure. Beyond this temperature, there exist three, relatively faster, main stages of decomposition which may be ascribed to depolymerization with elimination of chain-end monomers (region II), side-chain reactions involving chain scissions (region III), and carbon skeleton degradation (region IV), respectively. Overall, there is an ~80 % weight loss for the TGA analysis of sample $(3SC\text{-}575\text{-}10)_{20}$ which indicates a complete elimination of the polymeric component corresponding to a prepolymer resin sludge – ceramic initial loading ratio of 4:1 for the green body. To optimize the calcination process, sufficient times of 5 hours each are given at selected temperatures within these three regions (T_{c1} = 180 °C, T_{c2} = 360 °C and T_{c3} = 575 °C) to allow for optimized calcination and negligible pulverization of the 3D printed structures resulting in the thermal protocol shown in the calcination stage of Figure 3.2(b). The temperature range between the degradation offset temperature (575 °C) and the softening temperature of the B-SiO_2 (T_s = 711 °C) implies that there is a smaller window (T_w = 136 ^oC) for both calcination and densification for B-SiO_2 compared to other ceramic materials such as SiO_2 where this window is much wider (~5.3T_w) [15,17]. Figure 3.2(b) gives the optimized thermal protocol used for the entire thermal processing based on the TGA behavior of the green body. The calcination region is where mostly the polymeric component is eliminated in the form of carbon (IV) oxide, steam, and other small molecules. Temperature-time condition, T_{c1}, corresponds to the mid-temperature of region I (in Figure 3.2(a)), whereas the temperature-time condition T_{c2} corresponds to the temperature boundary between region II and III (in Figure3.2 (a)). Temperature-time condition T_{c3} is the degradation-offset temperature established (in Figure 3.2(a)) and the relatively slower ramp temperature between T_{c2} and T_{c3} was utilized because there is a higher tendency for pulverization at these temperature regions. An optimum temperature for densification (T_d =700 ˚C ~ 98.5 % T_s) was established and the densification was carried out for a sufficient time of 10 hours as observed in Figure 3.2(b) (temperature-time condition T_d).

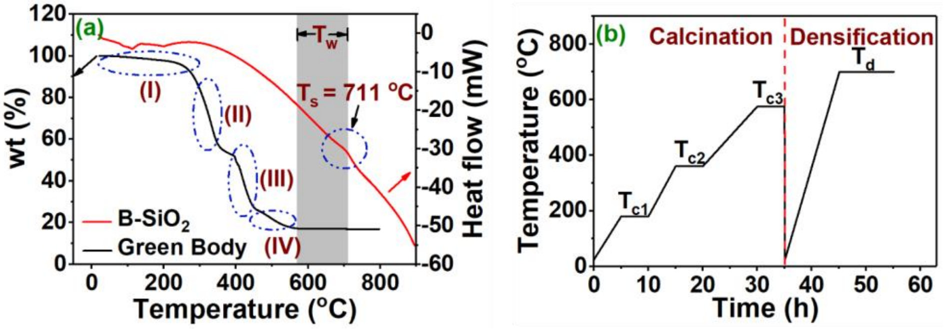

Figure 3-2: (a) DSC and TGA curves for B-SiO_2 powder and B-SiO_2-resin green body respectively for temperature ramping of 10°C/min in air. The regions (I)-(IV) indicate elimination of solvents, depolymerization, side chain reactions and elimination of residual polymer network component, respectively. (b) Thermal protocol for the calcination and densification of the B-SiO_2 body. The temperature-time conditions, T_{c1}, T_{c2} and T_{c3} indicate conditions allowing for gradual and steady reactions for the regions (I) – (IV). T_{c1} corresponds to the mid-temperature of region I in Figure 3.2a; T_{c2} corresponds to the temperature boundary between region II and III in Figure 3.2a. T_{c3} is the degradation-offset temperature established in Figure 3.2a. T_d is densification temperature.

The optical transparency property is key for glasses in general hence we investigated the optical transmittance property of the fabricated glass as a function of the particle loadings in the resin sludge. Under the same temperature, time and environmental conditions, we observed that Samples $(3SC\text{-}575\text{-}10)_{40}$ and $(3SC\text{-}575\text{-}10)_{60}$ with ceramic particle loadings of 40 % and 60 % yielded more transparent samples with better fidelity and we ascribe this to the fact that the densification conditions used reduced the porosities much without causing any devitrification whereas sample $(3SC\text{-}575\text{-}10)_{20}$ exhibited the least optical transparency as there was remnant porosity within its structure after densification. Its transmittance was only about 45 % that of the $(3SC\text{-}575\text{-}10)_{40}$ sample. Figure 3.3(a) however showed a better transmittance for a 40 % loading compared to that for 60 %, therefore most part of this work was carried out using a 40 % loading. Apparently, there is a sintering temperature limit beyond which softening will occur (711 ˚C) altering the printed shape or causing devitrification. However, we presume that the use of finer and more homogenous ceramic precursor particles, appropriate sintering aids, extended sintering times or improved vacuum conditions could further improve the overall transmittance of the samples for desired applications.

Figure 3.3(b) shows XRD patterns collected on the samples densified under ambient pressures and under vacuum using similar heat treatment protocols. Crystalline peaks observed at 27.6°, 42° and 51° can be ascribed to the formation of hexagonal quartz crystals with lattice parameters of a = 4.9127Å and c = 5.4045 Å (space group $P3_221$) which are evidence of the devitrification [26]. Under vacuum densification, the sample remained amorphous with just the typical halo for amorphous materials observed, thus confirming the absence of devitrification as no crystalline peaks were observed. Figure 3.3(c) shows the XRD results observed after densification in vacuum for different heat treatment protocol shown in Table 1. There are no observed continuous or discrete sharp devitrification peaks irrespective of the route taken; however, slight shifts in the amorphous halo peaks and magnitude are observable and these may be ascribed to varying degree of amorphousness as a result of the various thermal protocols [27]. The amorphous halo peaks for B-SiO_2 glass are typically observed at 26°. For the case of this work, the temperature of calcination has a negligible effect on the amorphous peak positions as observed when comparing samples $(1SC\text{-}575\text{-}10)_{40}$ to $(3SC\text{-}500\text{-}10)_{40}$ and $(3SC\text{-}575\text{-}05)_{40}$ to $(3SC\text{-}600\text{-}05)_{40}$; however, larger densification times (t_d) result in a more leftward deviation of the halo peak from this typical value (26°). We attribute this deviation to a gradual reorganization of the silicon oxide continuous random network towards the formation of a random close packed semi-phase leaving behind an amorphous halo rich in boron oxide.

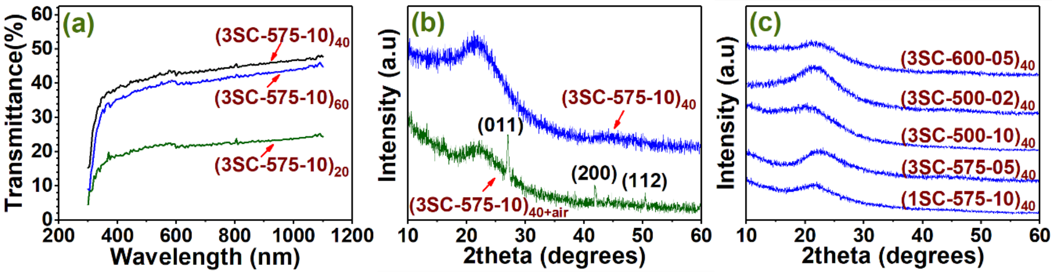

Figure 3-3: (a). Optical transmittance spectra of B-SiO_2 densified glass samples with different initial ceramic resin composition. (b) XRD patterns of prepared B-SiO_2 glass samples after densification in air at 700 °C; after densification in vacuum at 700 °C. (c) XRD patterns of prepared B-SiO_2 glass samples under different heat treatments in vacuum indicated in Table 1.

Figure 3.4(a) shows the EDS spectrum of the B-SiO_2 structure modified by Ce^{3+} ions with concentration 8 mol%. The 0.883 keV M and 1.739 keV K_α energy peaks for cerium and silicon, respectively, are evident. Quantitatively, from the EDS data, the atomic percent ratio of cerium silicon and boron are respectively 0.1:28.4:11.2 Figure 3.4(b) shows the excitation and emission spectra of B-SiO_2:Ce^{3+} and pure B-SiO_2 samples. The expectedly observed emission and excitation peaks at 388 nm and 242 nm respectively, are ascribable to the 4f–5d electronic transitions associated with the presence of Ce^{3+} ions [28–30] and the deviation of luminescent peak values from other published works is ascribed to the incident radiation interaction with the glass structure as well as effects during the transfer of carriers to the luminescence centers.

The observed luminescence further establishes the capacity of the stereolithographic technique to retain ions in the luminescent trivalent state as against having a competition between the tetravalent states observed during typical melt-quenching in the absence of a reducing atmosphere [28,30–32]. There is no emission in the undoped B-SiO_2 glass at the excitation wavelength considered which indicates the absence of luminescence centers. The optical properties of the Ce-doped glasses were also studied. Figure A4 gives the reflectance of an arbitrary sample Ce: 3SC-575-08 showing that there is only a 4% reflectance loss for our samples during the transmittance measurements. Figure 3.4(c) gives the absorbance cut-off wavelength as a function of increasing cerium concentration. This is the wavelength below which the glass absorbs all of the incident light and it is observed to depend strongly on concentration as expected, ranging from about 300 nm to 360 nm so that there is an overall change of about 60 nm for a concentration change of 10 mol %. This change is comparable to that reported for Ce-doped B-SiO_2 glasses (40 nm for 0.5 wt. % Ce_2O_3 change concentration) [33] and increasing trend is similar for other glasses of different compositions [30,33–35]. The increasing trend has been observed in several doped borosilicate glasses [33]. Figure 3.4(d-f) show the optical band gap values (E_g), refractive index and Urbach Energy as functions of increasing cerium concentration. The Urbach energy which is characteristic for band edge transition of semiconductors is the width of the tail of localized states corresponding to the optical transition between localized states adjacent to the valence band and the extended states in the conduction band lying above the mobility edge [36]. Lower values for Urbach energy imply the presence of minimal defect (less degree of disorder) and thus a more structurally organized matrix. The presence of these disorders and defects within glass matrix systems typically lead to generation of localized states near or within the conduction band thus increasing band tail widths. Our Urbach energy results show a steep decrease up to 2 mol%, a gradual increase up to 8 mol % and then a decrease up to 10 mol %. In comparison to past reports, for the dopant range of 0 - 0.5 mol % a similarly decreasing Urbach energy trend is observed in works by Kaur et al [37] whereas a reverse increasing trend is observed by Lak et al [38]. Between 0.5 mol % and 1 mol % dopant concentration, a similar decreasing Urbach energy is however observed in both reports [37,38] with increasing cerium dopant concentration. The optical band gap E_g is determined based on the Urbach and Tauc model [8,39] by considering a linear extrapolation to the zero ordinate of a plot of ($ahv^{1/2}$) against the incident photon energy (hv) [40]. The Tauc plot relation for optical band gap is given by eqn. (1):

$$\frac{hv\alpha}{n} = A(hv - E_g) \ldots\ldots\ldots\ldots\ldots\ldots\ldots\ldots\ldots\ldots\ldots \text{(1)}$$

Where h is the Planck's constant, v is the vibration frequency, α is the absorption coefficient, E_g is the band gap energy, A is a constant proportionality and n is ½, 3/2, 2 or 3 for a direct, forbidden direct, indirect or forbidden indirect transition respectively. The Urbach energy was estimated based on eqn. (2) by taking the reciprocal slope of a graph of the natural logarithm of the absorption coefficient (lnα) against the incident photon energy (hv):

$$\alpha = \alpha o \exp\left(\frac{hv}{Eu}\right) \ldots\ldots\ldots\ldots\ldots\ldots\ldots\ldots\ldots\ldots\ldots \text{(2)}$$

The refractive index (n) obtained from the optical band gap was determined according to the eqn. (3) based on the Lorenz theory:

$$\frac{n^2-1}{n^2+2} = 1 - \sqrt{\left(\frac{E_g}{20}\right)} \text{ .... (3)}$$

where n is the refractive index and E_g is the optical band gap whereas the reflectance losses were determined based on eqn. (4):

$$R = \left(\frac{n-1}{n+1}\right)^2 \text{ .... (4)}$$

The optical band gap is observed to vary from 3.64 to 3.12 for a Cerium dopant concentration range of 0 to 10 % whereas the Urbach energy varies from 0.40 to 0.55 eV. The reflection loss estimated from eqn 4 and shown in Table 3 show that the scattering losses in this work are comparable to other doped B-SiO_2 by melt quenching ranging between 0.124- 0.130 in the dopant range we have considered. The observed decrease in band gap and corresponding increase in the Urbach energy with increasing concentration is consistent with the reported band gap changes of 3.53 eV to 3.26 eV and Urbach energy changes of 0.61 to 0.25 eV (for 0.5 to 1.5 CeO_2 %) [38]. Our result shows a gradual decrease in band gap with increasing dopant concentration which is consistent with reports on cerium doped B-SiO_2 glasses [37,38,42]. This observed change is less steep compared to other reports and band gap values here reported are comparatively higher than similar reports implying less formation of non-bridging oxygen. Non-bridging oxygen binds excited electrons less tightly than bridging oxygen [43]. We ascribe the differences in band gap magnitude at zero cerium dopant concentration compared to the reports in Table 3 to the effects of the other constituents of our borosilicate matrix which expectedly vary from one borosilicate system to the other [37,38,42]. A gradual decrease in optical band gap energy and a corresponding increment in Urbach energy up to 8 % Cerium content is observed in our work after which a reverse trend is observed to 10 mol %. This has been ascribed to an increased presence of non-bridging oxygen, increasing concentration of bonding effects and consequent increase of the donor centers within the B-SiO_2 network [8,43,44]. The reverse trend beyond 8 % Cerium concentration could be attributed to saturation (a quenching effect) typically observed in doped luminescent systems for some dopant beyond certain doping levels [41]. This effect could be ascribed to an increased interaction between Ce-ion luminescent centers with dopant concentration in the B-SiO_2 matrix as well as non-radiative losses in excitation energies. It should be noted that the determination of bandgap values from the optical absorption has to be performed with care since the scattering could be strong which makes the calculated bandgaps unreasonably smaller than real values (for typical borosilicate glasses). Future studies need to be carried out to compare the bandgap values using other characterization approaches. Figure 3.4(f) shows that the refractive index increases from 2.08 to 2.13 for a Ce concentration range of 0% to 10%. This increasing trend is consistent with observed increasing values reported for Nd doped glass (2.97 to 3.026) [45]. In comparison to values obtained for Cerium doped borosilicate glass estimated by the Gladstone Dale relation by Kietly et al. [35], values obtained in this work were about 33% higher than values obtained in their report (~1.5) and this difference is ascribable to be as a result of the difference in borosilicate glass composition. Other previous reports on Cerium doped B-SiO_2 glasses also show a similar increasing refractive index trend with increasing cerium concentration [37]. Again, the quenching effect is also observed beyond 8 % Cerium concentration as with the Urbach and band gap energies.

Table 3 further shows the data of other reported values for doped borosilicate glasses with different dopant concentrations. In general, dopant whose oxides have a higher refractive index compared to silica exhibit an increasing refractive index with increasing concentration and the reverse is the case for dopants with oxides whose oxides have a lower refractive index. The theoretically expected refractive index for ideal ceramic composites is given by eqn. 5:

$$\varepsilon = n^2 = \sum v_i {n_i}^2 \text{.....................} \; (5)$$

Where, ε is the dielectric constant, n is the refractive index of the resultant glass, v_i are the fractional content and n_i are the refractive indices of the individual constituents. Our observed refractive index change agrees with equation 4 and the gradient of the

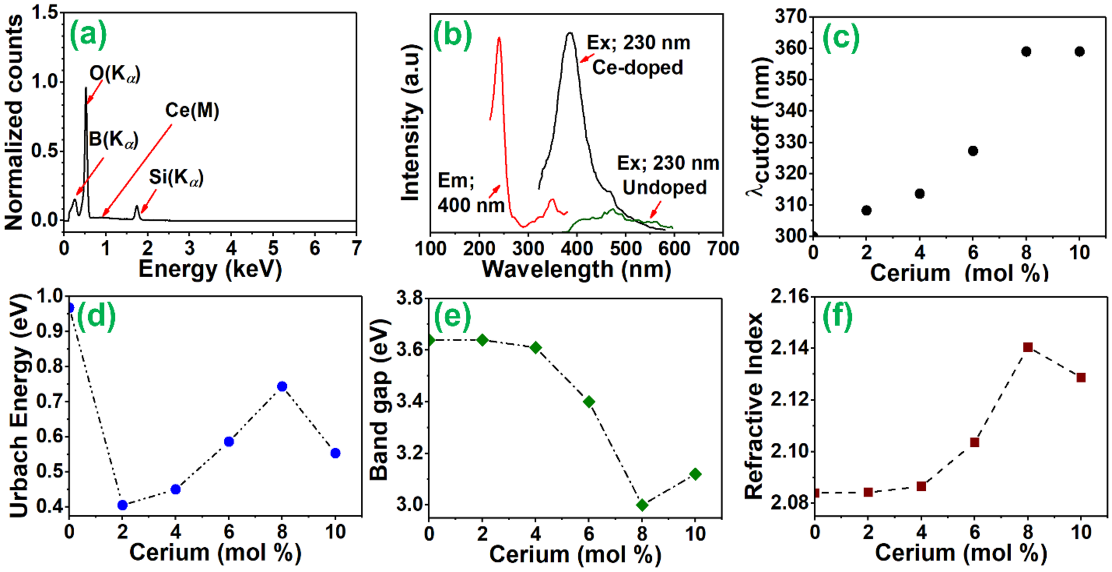

Figure 3-4: (a) Energy dispersive spectra of the Ce-doped B-SiO$_2$ glass (Ce:3SC-575-08)$_{40}$ for a 8 mol % Ce dopant concentration. (b) Photoluminescence excitation (400 nm emission) and emission spectra (230 nm excitation) for undoped and 4 mol % Ce acetate glass. (c-f) The effect of Ce dopant concentration on cut off wavelength, optical band gap, Urbach energy, and refractive index of Ce-doped B-SiO$_2$ glass, respectively. Broken lines are guides to the eyes only.

Table 3.3: Summary of some reported optical properties of borosilicate glass with different dopants.

Material composition	Dopant range (%)	Urbach energy change (eV)	Band gap (eV)	Refractive index	Reflection Losses	Method of analysis	Method of sample preparation	Ref.
B-SiO$_2$:Sm	0.3	**1.04	**1.01	N/A	N/A	Davis and Mott relation	Melt quenching	[46]
B-SiO$_2$:Pr	1	**1.077	**0.942	**1.614	0.055	Tauc Relation	Melt quenching	[47]
B-SiO$_2$:Er	0 - 4	0.17 - 0.61	2.56 - 2.8	2.45 - 2.53	0.177-0.188	Tauc Relation	Melt quenching	[48]
B-SiO$_2$:Nd	0.3	**1.08	**0.96	**1.62	0.056	Tauc Relation	Melt quenching	[49]
B-SiO$_2$:Cr	0 - 0.8	0.33 - 0.22	3.79 - 2.09	N/A	N/A	Tauc Relation	Melt quenching	[50]
B-SiO$_2$:Mn	0 - 0.9	0.249 - 0.275	4.05 - 3.65	1.65 - 1.66	0.060-0.062	Tauc Relation	Melt quenching	[51]
B-SiO$_2$:Co	0 - 5	0.25 - 1.2	N/A	N/A	N/A	N/A	Melt quenching	[52]
B-SiO$_2$:Ti	0 - 10	0.565 - 0.48	3.41 - 3.44	2.61 - 2.64	0.199-0.203	Tauc Relation	Melt quenching	[53]
B-SiO$_2$:Pb	0 - 0.7	0.33 - 0.37	2.9 - 2.85	N/A	N/A	Tauc Relation	Melt quenching	[54]
B-SiO$_2$:Ce	1.8	N/A	** 3.37	N/A	N/A	Tauc Relation	Commercial	[54]
B-SiO$_2$:Ce	0 - 1	1 – 0.62	3.15 – 2.92	2.78 – 2.85	0.222-0.231	Tauc Relation	Melt quenching	[37]
B-SiO$_2$:Ce	0 – 1.5	0.45 – 0.25	3.53 – 3.26	1.66 - 1.68	0.062-0.064	Tauc Relation	Melt quenching	[38]
B-SiO$_2$:Ce	0 – 2	N/A	3.00 – 2.44	N/A	N/A	Tauc Relation	Melt quenching	[42]
B-SiO$_2$:Ce	2 - 10	0.4 - 0.55	3.64 - 3.12	2.08 - 2.13	0.124-0.130	Tauc Relation	Stereolithography	This work
** indicates maximum of a reported range of values								

refractive index with cerium composition is differs by only 3 %. The reflection loss estimated from eqn 4 and shown in Table 3 show that the scattering losses in this work are comparable to other published works and range between 0.124-0.130 in the dopant range we have considered. The results of the optical properties for our Cerium doped B-SiO$_2$ show consistency of the optical properties of luminescent glass fabricated by stereolithography with that of other fabrication processes. The steepness trends also indicate that compared to other reports and methods of fabrication, the stereolithography technique is unique and could accommodate more tunability in a broad dopant concentration while also ensuring uniform doping. Although we have focused on optical properties and characterizations here we intend to further explore higher resolution structures in subsequent works.

3.4 Conclusion

We have successfully synthesized transparent undoped and Ce doped borosilicate glass with a dopant level of up to 10 mol % by stereolithography calcining and densification in air and vacuum. The calcination temperature is about 98 % of the softening temperature and the glass exhibits no devitrification and good optical properties, which can be further modified to yield functional glass materials. Incorporation of Cerium dopants yielded luminescent glass which exhibited a quenching effect at 8% dopant concentration level and a direct band gap. This is, to the best of our knowledge, one of the first reports on the fabrication of amorphous borosilicate glass via stereolithography. Our fabrication approach provides a potentially promising path for the application of VPP, powder bed fusion and other additive manufacturing techniques for B-SiO_2 glass fabrication. It is a procedure that will allow for rapid, digital and on-demand manufacturing for advanced optical and luminescence systems.

3.5 References

[1] C. Canevali, M. Mattoni, F. Morazzoni, R. Scotti, M. Casu, A. Musinu, R. Krsmanovic, S. Polizzi, A. Speghini, M. Bettinelli, Stability of luminescent trivalent cerium in silica host glasses modified by boron and phosphorus, J. Am. Chem. Soc. (2005). https://doi.org/10.1021/ja052502o.

[2] K.S. Rudramamba, S.K. Taherunnisa, M. Rami Reddy, The role of CuO as limiting and luminescent probe for orange red emission of Sm3+ ions in strontium bismuth borosilicate glasses, Opt. Mater. (Amst). (2020). https://doi.org/10.1016/j.optmat.2020.110340.

[3] Z. Tang, Z. Huang, W. Han, J. Qi, N. Ma, Y. Zhang, T. Lu, Microwave-assisted synthesis of uranium doped Y2Zr2O7 transparent ceramics as potential near-infrared optical lens, Scr. Mater. (2020). https://doi.org/10.1016/j.scriptamat.2019.11.007.

[4] M.H. Jo, B.R. Koo, H.J. Ahn, Fe co-doping effect on fluorine-doped tin oxide transparent conducting films accelerating electrochromic switching performance, Ceram. Int. (2020). https://doi.org/10.1016/j.ceramint.2020.01.061.

[5] Z. Wang, L. Gan, W. Huang, Structural recovery and optical properties stabilization of CeO2/TiO2-doped boroaluminosilicate glass under gamma irradiation, Radiat. Phys. Chem. (2018). https://doi.org/10.1016/j.radphyschem.2018.05.033.

[6] J. An, Z. Zhang, Y. Qiu, Z.Y. Fu, Y. Zhou, F. Zeng, Luminescence properties of borosilicate glass doped with Ce3+/Dy3+/Eu3+ under ultraviolet excitation for white LED, J. Non. Cryst. Solids. (2019). https://doi.org/10.1016/j.jnoncrysol.2018.09.050.

[7] X.Y. Sun, Z.H. Xiao, Y.T. Wu, X.G. Yu, Q.L. Hu, Y. Yuan, Q. Liu, C. Struebing, Z. Kang, Role of Al3+ on tuning optical properties of Ce3+-activated borosilicate scintillating glasses prepared in air, J. Am. Ceram. Soc. (2018). https://doi.org/10.1111/jace.15773.

[8] A. Saeed, Y.H. Elbashar, S.U. El Kameesy, Optical Spectroscopic Analysis of High Density Lead Borosilicate Glasses, Silicon. (2018). https://doi.org/10.1007/s12633-015-9391-7.

[9] H.A. Elbatal, A.M. Abdelghany, F.H. Elbatal, F.M. Ezzeldin, Gamma rays interactions with WO 3-doped lead borate glasses, Mater. Chem. Phys. (2012). https://doi.org/10.1016/j.matchemphys.2012.03.032.

[10] B. Seyfarth, G. Matthäus, T. Ullsperger, S. Nolte, L. Schade, A. Tunnermann, Selective laser melting of glass using ultrashort laser pulses, in: 2018. https://doi.org/10.1117/12.2289614.

[11] F. Klocke, C. Ader, Direct laser sintering of ceramics, Solid Free. Fabr. Symp. (2003).

[12] J. Luo, J.T. Goldstein, A.M. Urbas, D.A. Bristow, R.G. Landers, E.C. Kinzel, Additive manufacturing of borosilicate glass (Conference Presentation), in: SPIE-Intl Soc Optical Eng, 2017: p. 8. https://doi.org/10.1117/12.2256667.

[13] J. Luo, T. Bender, D.A. Bristow, R.G. Landers, J.T. Goldstein, A.M. Urbas, E.C. Kinzel, Bubble formation in additive manufacturing of borosilicate glass, 2016.

[14] J. Klein, M. Stern, G. Franchin, M. Kayser, C. Inamura, S. Dave, J.C. Weaver, P. Houk, P. Colombo, M. Yang, N. Oxman, Additive Manufacturing of Optically Transparent Glass, 3D print. Addit. Manuf. (2015). https://doi.org/10.1089/3dp.2015.0021.

[15] F. Kotz, K. Arnold, W. Bauer, D. Schild, N. Keller, K. Sachsenheimer, T.M. Nargang, C. Richter, D. Helmer, B.E. Rapp, Three-dimensional printing of transparent fused silica glass, Nature. 544 (2017). https://doi.org/10.1038/nature22061.

[16] I. Cooperstein, E. Shukrun, O. Press, A. Kamyshny, S. Magdassi, Additive Manufacturing of Transparent Silica Glass from Solutions, ACS Appl. Mater. Interfaces. 10 (2018). https://doi.org/10.1021/acsami.8b03766.

[17] D.T. Nguyen, C. Meyers, T.D. Yee, N.A. Dudukovic, J.F. Destino, C. Zhu, E.B. Duoss, T.F. Baumann, T. Suratwala, J.E. Smay, R. Dylla-Spears, 3D printing: 3D printed Transparent Glass (Adv. Mater. 26/2017), Adv. Mater. 29 (2017). https://doi.org/10.1002/adma.201770191.

[18] T. Moritz, J. Schilm, A. Rost, E. Schwarzer, S. Weingarten, U. Scheithauer, K. Wätzig, D. Wagner, A. Michaelis, Ceramic Additive Manufacturing Methods Applied to Sintered Glass Components with Novel Properties, Ceram. Mod. Technol. 1 (2019) 111–119. https://doi.org/10.29272/CMT.2019.0008.

[19] D.P. Cesarano III, Joseph; calvert, Freeforming Objects With low Binder Slurry, 2000.

[20] G.M. Gratson, F. García-Santamaría, V. Lousse, M. Xu, S. Fan, J.A. Lewis, P.V. Braun, Direct-Write Assembly of Three-Dimensional Photonic Crystals: Conversion of Polymer Scaffolds to Silicon Hollow-Woodpile Structures, Adv. Mater. 18 (2006) 461–465. https://doi.org/10.1002/adma.200501447.

[21] C.M. Larson, J.J. Choi, P.A. Gallardo, S.W. Henderson, M.D. Niemack, G. Rajagopalan, R.F. Shepherd, Direct Ink Writing of Silicon Carbide for Microwave Optics, Adv. Eng. Mater. 18 (2016) 39–45. https://doi.org/10.1002/adem.201500298.

[22] K. Sun, T.S. Wei, B.Y. Ahn, J.Y. Seo, S.J. Dillon, J.A. Lewis, 3D printing of interdigitated Li-ion microbattery architectures, Adv. Mater. 25 (2013) 4539–4543. https://doi.org/10.1002/adma.201301036.

[23] Method of and apparatus for production of three dimensional objects by stereolithography, 1992.

[24] Foreign Application Priority Data (54) Composition and method for producing a molded body from a highly pure , transparent quartz glass by means of additive manufacturing, 2016.

[25] US10940639B1 - Glass scintillators and methods of manufacturing the same - Google Patents, (n.d.). https://patents.google.com/patent/US10940639B1/en (accessed May 14, 2021).

[26] P. Norby, Synchrotron Powder Diffraction using Imaging Plates: Crystal Structure Determination and Rietveld Refinement, J. Appl. Crystallogr. (1997). https://doi.org/10.1107/S0021889896009995.

[27] S. Thakral, M.W. Terban, N.K. Thakral, R. Suryanarayanan, Recent advances in the characterization of amorphous pharmaceuticals by X-ray diffractometry, Adv. Drug Deliv. Rev. (2016). https://doi.org/10.1016/j.addr.2015.12.013.

[28] Y. Isokawa, D. Nakauchi, G. Okada, N. Kawaguchi, T. Yanagida, Radiation induced luminescence properties of Ce-doped Y2O3-Al2O3-SiO2 glass prepared using floating zone furnace, J. Alloys Compd. (2019). https://doi.org/10.1016/j.jallcom.2018.12.245.

[29] W. Chewpraditkul, Y. Shen, D. Chen, B. Yu, P. Prusa, M. Nikl, A. Beitlerova, C. Wanarak, Luminescence and scintillation of Ce3+-doped high silica glass, Opt. Mater. (Amst). (2012). https://doi.org/10.1016/j.optmat.2012.04.012.

[30] Y. Tratsiak, M. Korzhik, A. Fedorov, G. Dosovitsky, O. Akimova, S. Belus, M. Fasoli, A. Vedda, V. Mechinsky, E. Trusova, On the stabilization of Ce, Tb, and Eu ions with different oxidation states in silica-based glasses, J. Alloys Compd. (2019). https://doi.org/10.1016/j.jallcom.2019.05.105.

[31] K. Kagami, Y. Fujimoto, M. Koshimizu, D. Nakauchi, T. Yanagida, K. Asai, Photoluminescence and radiation response properties of CsPO3-Al(PO3)3-CeCl3-based glass scintillators, Opt. Mater. (Amst). (2019). https://doi.org/10.1016/j.optmat.2018.04.036.

[32] H. El Hamzaoui, B. Capoen, N. Al Helou, G. Bouwmans, Y. Ouerdane, A. Boukenter, S. Girard, C. Marcandella, O. Duhamel, G. Chadeyron, R. Mahiou, M. Bouazaoui, Cerium-activated sol-gel silica glasses for radiation dosimetry in harsh environment, Mater. Res. Express. (2016). https://doi.org/10.1088/2053-1591/3/4/046201.

[33] C. Jiang, Q. Zeng, F. Gan, Scintillation luminescence of cerium-doped borosilicate glass containing rare-earth oxide, Hard X-Ray, Gamma-Ray, Neutron Detect. Phys.

II. 4141 (2000) 316–323. https://doi.org/10.1117/12.407593.

[34] L. Dong, A.K. Agarwal, D.J. Beebe, H. Jiang, Adaptive liquid microlenses activated by stimuli-responsive hydrogels, Nature. 442 (2006) 551–554. https://doi.org/10.1038/nature05024.

[35] M.W. Kielty, M. Dettmann, V. Herrig, M.G. Chapman, M.R. Marchewka, A.A. Trofimov, U. Akgun, L.G. Jacobsohn, Investigation of Ce3 + luminescence in borate-rich borosilicate glasses, J. Non. Cryst. Solids. 471 (2017) 357–361. https://doi.org/10.1016/J.JNONCRYSOL.2017.06.022.

[36] N. Ghobadi, Band gap determination using absorption spectrum fitting procedure, Int. Nano Lett. (2013). https://doi.org/10.1186/2228-5326-3-2.

[37] R. Kaur, R.B. Rakesh, S.G. Mhatre, V. Bhatia, D. Kumar, H. Singh, S.P. Singh, A. Kumar, Thermoluminescence, structural and optical properties of Ce3+ doped borosilicate doped glasses, J. Mater. Sci. Mater. Electron. 2021 3213. 32 (2021) 18381–18396. https://doi.org/10.1007/S10854-021-06382-8.

[38] F. Lak, M. Rezvani, Optical characterization of BK7 borosilicate glasses containing different amounts of CeO2, Adv. Ceram. Prog. 2 (2016) 17–24. https://doi.org/10.30501/ACP.2016.70026.

[39] J. Tauc, A. Menth, States in the gap, J. Non. Cryst. Solids. 8–10 (1972). https://doi.org/10.1016/0022-3093(72)90194-9.

[40] P. Limkitjaroenporn, J. Kaewkhao, P. Limsuwan, W. Chewpraditkul, Physical, optical, structural and gamma-ray shielding properties of lead sodium borate glasses, J. Phys. Chem. Solids. (2011). https://doi.org/10.1016/j.jpcs.2011.01.007.

[41] S. Insitipong, J. Kaewkhao, T. Ratana, P. Limsuwan, Optical and Structural Investigation of Bismuth Borate Glasses Doped With Dy3+, Procedia Eng. 8 (2011) 195–199. https://doi.org/10.1016/j.proeng.2011.03.036.

[42] P. Kaur, G.P. Singh, S. Kaur, D.P. Singh, Modifier role of cerium in lithium aluminium borate glasses, J. Mol. Struct. 1020 (2012) 83–87. https://doi.org/10.1016/J.MOLSTRUC.2012.03.053.

[43] A. Bahadur, Y. Dwivedi, S.B. Rai, Optical properties of cerium doped oxyfluoroborate glass, Spectrochim. Acta - Part A Mol. Biomol. Spectrosc. (2013). https://doi.org/10.1016/j.saa.2013.03.066.

[44] Z. Hussain, Optical Band Gap, Oxidation Polarizability, Optical Basicity and Electronegativity Measurements of Silicate Glasses Using Ellipsometer and Abbe

Refractometer, New J. Glas. Ceram. 11 (2021) 1–33. https://doi.org/10.4236/njgc.2021.111001.

[45] R. Kaur, R.B. Rakesh, S.G. Mhatre, V. Bhatia, D. Kumar, H. Singh, S.P. Singh, A. Kumar, Physical, optical, structural and thermoluminescence behaviour of borosilicate glasses doped with trivalent neodymium ions, Opt. Mater. (Amst). 117 (2021) 111109. https://doi.org/10.1016/j.optmat.2021.111109.

[46] P. Goyal, Y.K. Sharma, S. Pal, U.C. Bind, S.C. Huang, S.L. Chung, Structural, optical and physical analysis of B2O3–SiO2–Na2O–PbO–ZnO glass with Sm3+ ions for reddish–orange laser emission, J. Lumin. 192 (2017) 1227–1234. https://doi.org/10.1016/J.JLUMIN.2017.08.061.

[47] S.P. Priyanka Goyal, U.C.B. and Y.K. Sharma, Structural and physical analysis of borosilicate glasses with Pr3+ ions, Adv. Mater. Proc. 2 (2017) 119–124.

[48] N.A.N. Razali, I.S. Mustafa, N.Z.N. Azman, H.M. Kamari, A.A. Rahman, K. Rosli, N.S. Taib, N.A. Tajuddin, The Physical and Optical Studies of Erbium Doped Borosilicate Glass, J. Phys. Conf. Ser. 1083 (2018) 012004. https://doi.org/10.1088/1742-6596/1083/1/012004.

[49] Yogesh Kumar Sharma, Priyanka Goyal, Sudha Pal, Umesh Chandra Bind, Optical and Physical Analysis of Nd3+ Doped Borosilicate Glasses, J. Mater. Sci. Eng. B. 5 (2015) 406–417. https://doi.org/10.17265/2161-6221/2015.11-12.002.

[50] E. Ebrahimi, M. Rezvani, Optical and structural investigation on sodium borosilicate glasses doped with Cr2O3, Spectrochim. Acta Part A Mol. Biomol. Spectrosc. 190 (2018) 534–538. https://doi.org/10.1016/J.SAA.2017.09.031.

[51] M.Y. Hassaan, H.M. Osman, H.H. Hassan, A.S. El-Deeb, M.A. Helal, Optical and electrical studies of borosilicate glass containing vanadium and cobalt ions for smart windows applications, Ceram. Int. 2 (2017) 1795–1801. https://doi.org/10.1016/J.CERAMINT.2016.10.137.

[52] K.S. Shaaban, I. Boukhris, I. Kebaili, M.S. Al-Buriahi, Spectroscopic and Attenuation Shielding Studies on B2O3-SiO2-LiF- ZnO-TiO2 Glasses, Silicon 2021. (2021) 1–10. https://doi.org/10.1007/S12633-021-01080-W.

[53] C.R. Gautam, S. Das, S.S. Gautam, A. Madheshiya, A.K. Singh, Processing and optical characterization of lead calcium titanate borosilicate glass doped with germanium, J. Phys. Chem. Solids. 115 (2018) 180–186. https://doi.org/10.1016/J.JPCS.2017.12.038.

[54] S. Baccaro, A. Cemmi, I. Di Sarcina, F. Menchini, Gamma Rays Effects on the Optical Properties of Cerium-Doped Glasses, Int. J. Appl. Glas. Sci. 6 (2015) 295–301. https://doi.org/10.1111/IJAG.12131.

4 Towards the incorporation of stereolithography for gradient refractive index lens (GRI-L) fabrication: a modelling and simulation approach.

4.1 Introduction

The use of transparent lenses in various applications where the modification of light, sound or electronic waves are of paramount importance is well known [1,2]. Hydrogel based, silicone, silica and poly (methyl methacrylate) (PMMA) based glasses have all been utilized for fabricating various lens types depending on the specific properties required for varying applications. These properties include oxygen permeability, cost and ease of manufacturing, transparency, biocompatibility, density, mechanical properties like, toughness stiffness and elastic modulus, hydrophobicity, bio compatibility etc. Gradient Refractive Index lenses (GRI-Ls) entail optical properties generated from a preset gradation of refractive index in a material. Dating back to Maxwell [3]; properties of cylindrical GRI-Ls may either exhibit axial or radial trends. Key merits of GRI-Ls over normal spherical lenses are that these lenses with planar surfaces make mounting in systems with other optical components much easier. In addition, spherical aberrations typical of spherical lenses are much reduced and tunable depending on the precision of the fabrication technique utilized. GRI-Ls find applications in micro-optical telescopes, solid state lasers, fiber collimators, optical data storage, ophthalmology (high power contact lenses) etc.

Conventional fabrication modes for lenses entail spin casting, molding and lathe cutting. In order to generate gradient refractive indices on substrates several approaches have been utilized. For polymeric lenses, the use of photocurable systems such as UV lasers, where photosensitive monomeric systems are either partially polymerized or partially cross-linked so that the refractive index changes as a function of the degree of polymerization or crosslinking at different radial distances [4–7] have been reported. For ceramic GRI-Ls, the use of selective charged particle substitution and implantation [8] where ion deficit substrates are immersed in an ion rich liquid to allow for diffusion into the matrix or for a replacement have also been utilized; ion reorganization where for instance, the application of an electric field near the glass transition temperature induces migration of ions in the lens material [9,10], chemical vapor deposition where two or more materials are selectively deposited onto a substrate [11], and generation of dopant profile by nucleon irradiation have also been used to generate refractive index profiles [12,13]. Controlled vitrification has also been shown possible by subjecting a preformed material selectively to thermal energy sources even though this may lead to a slight degree of scattering from the crystallites/crystals present [10,14,15]. Most of these techniques have not been shown to be promising towards scale-up as well as for on-chip applications. There are limited commercially available GRI-Ls which parade a narrow range of material choices. The recent successes in additive manufacturing for ceramic and polymeric glasses imply that the key issues with other fabrication methods for materials such as difficulty in shaping and resolution of structures can now be overcome [16,17]. Very recently the Direct Ink Writing (DIW) where thermal-curable resins are dried and then subjected to heat treatment has been reported for ceramic GRI-Ls [18]. Here two separate inks of silica and silica-titania were utilized in building GRI-Ls by a controlled selective ink writing process. However, the subsequent drying and heat treatment process associated with the DIW technique is relatively time consuming. The use of a piezo ink-jet printing technique for printing GRI-Ls have also been explored [7] although the extension of this for ceramic glass lenses requires a resort to undesirably high melting temperatures and could result in poly-crystalline materials if not properly controlled. In addition, these additive manufacturing processes have not focused on tailoring the -Ls towards precise properties for desired applications.

This work shows a modelling and simulation approach that predicts the use of stereolithography as an additive manufacturing technique for fabricating GRI-Ls as well as establishes some resulting optical properties. It combines established knowledge about the so-called sol-gel synthesis for ceramic materials alongside current advancements in stereolithographic techniques. As a test case we simulate and investigate the properties of pure ceramic (SiO_2-TiO_2 GRI-Ls. Unlike other methods for GRI-L fabrication, this technique is cheap, fast, less complex easy to carry out, allows for better resolution of structures, produces a precise distribution of the refractive index, and can be extended to ceramic glass lenses. It can also potentially allow for integration into on-chip applications, Experimental investigation of the miscibility of the resin system and hybrid resin systems based on a ceramic-polymer composite (HEMA-TiO_2) demonstrates the feasibility of the process as well as the potential for the application of stereolithography towards GRI-Ls.

4.2 Experimental Section

4.2.1 Simulation

The simulation was carried out using COMSOL based on Electromagnetic Ray Optic Modules. Incident plane polarized waves of wavelength 589.29 nm with intensity 100 W/m^2 were used. Three GRI-L systems (L1, S1, H1) with refractive index exhibiting a rotational symmetry about the z axis with parabolic transverse profiles according to the expressions in Table 1 were utilized where $n(r)$ is the refractive index at a location r from the origin; n_o is the refractive index at the origin and; R is the radius of the lens. The parameters A (= ${g_o}^2$); g and f (sometimes called focal parameter) are all measures of the GRI-L parameter. Because the simulation was based on a ceramic lens case study, we modeled a 60 % shrinkage consistent with the post-printing processes (calcination and densification) of the pHEMA-B-SiO$_2$ printed structures.

Table 4-1: Summary of synthesis parameters of simulated 3D printed B-SiO$_2$ glass samples.

	p(HEMA)	B-SiO$_2$	TiO$_2$
n_o	1.514	1.47	2.76
GRI-L Power law distribution (so-called Luneburg) (L1)	$n(r) = \frac{1}{f}\sqrt{1+f^2-(\frac{r}{R})^2}$		
GRI-L Quadratic distribution (so-called selfoc) (S1)	$n(r) = n_o(1-\frac{{g_o}^2}{2}r^2)$		
GRI-L hyperbolic distribution (H1)	$n(r) = n_o(\sec h(gr))$		

Table 4-2: GRI-L Parameters for an average GRI-L profile of 5 m^{-1}.

GRI-L Quadratic distribution (so-called selfoc) (S1)	1651.3 m^2
GRI-L hyperbolic distribution (H1)	40.86 m^{-1}

4.2.2 Materials Selection:

We utilized miscible ceramics and polymeric material systems in such a way that we have a refractive index distribution from one extreme to the other. For the composite case, we utilize acrylate monomers as well as sol-gel precursors. As a test case we utilize hydroxyethyl methacrylate (HEMA) with a refractive index of 1.514 as the acrylate component and TiO_2 wet gel precursor system. For the ceramic lens case, fumed silica (n =1.45) coupled with a similar solution doped with 2-4 wt % TiO_2 precursor further combined with a photocurable HEMA resin mix in a 40: 60 ratio is utilized. The refractive index of both the pHEMA-TiO_2 and the SiO_2 -TiO_2 sludges vary according to equation 1.

$$n_s^2 = \sum \nu_i \, {n_i}^2 \qquad (1)$$

where n_s = refractive index of the sludge, v_i = composition of each sludge component and n_i = refractive index of each sludge component.

4.2.3 Printing:

We utilize a home-made printer that allows for 3D printing. The top down printer utilizes a 405 nm laser for curing a photoresin prepolymer sludge placed in a vat at some distance below the laser. The laser diameter can be tuned to desired resolution of about 100 µm. Figure 1 show the spin coating schematic utilized for presetting the composition gradation in the resin before printing radially outward. The characteristic gradation for a printing process is determined by the spin coating speed as well as the composition of both resins.

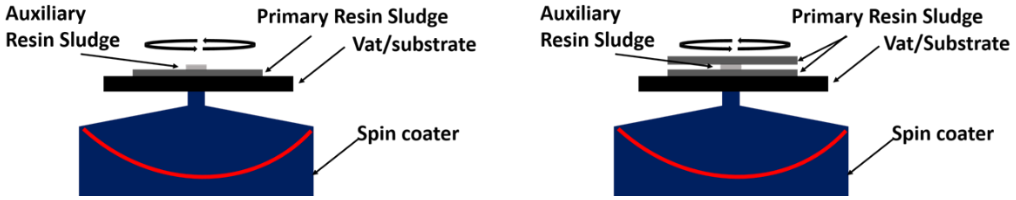

Figure 4-1: Schematic of the resin sludge stacking pattern for GRI-Ls. (a) two-layer stacking (b) three-layer stacking on a spin coater system.

The lenses were fabricated by first assembling two or more layers of both resins alternately upon a spin coater systematically. A first resin system (RS 1) was prepared from an acrylate-based pre-polymer resin-mix comprising hydroxyethyl methacrylate (HEMA) (Sigma Aldrich Inc.), trimethylolpropane ethoxylate triacrylate (Sigma Aldrich Inc.), and 0.5 wt% of phenylbis(2,4,6-trimethylbenzoyl) phosphine oxide (Sigma Aldrich Inc.) in the ratio of 100:50:7. The second (RS 2) was 40 volume % fumed silica nanoparticles to the first resin system to prepare a sludge. A third and fourth resin sludge system (RS 3, RS 4) were prepared by adding a TiO_2 gel to the first and second resin systems respectively and mixing thoroughly with a hotplate and magnetic stirrer in the dark for 24 hours. The gel: resin ratio was 1:4 by weight. The TiO_2 gel was formed by aging a TiO_2 sol-gel precursor synthesized from titanium isopropoxide. A 1 ml mixture of iso-propanol and 1 ml of water was added drop by drop to a 2 ml of titanium isopropoxide and left stirring for one hour at 80 ˚C. A nitric acid solution of 0.08 ml HNO3 acid and 0.8 ml of deionized water was further added into the mixture drop by drop while stirring at 80 ˚C for 6 hours. The final resin system (RS 4) was prepared by introducing 2wt % and 4 wt % TiO_2 into RS 2 and stirring vigorously. The prepared sludges were then degassed under vacuum before the 3D printing process on the SLA printer. Scanning Electron Microscopy (SEM), FS100 FEG emission SEM-EDS (Tokyo, Japan), was utilized to investigate the morphology of the resulting lens. Energy Dispersive X-ray Spectroscopy (EDS) was used to ascertain the elemental composition of the resulting products as well as establish the dopant profile. The light transmittance and absorption at different wavelengths of the final densified body are investigated using a Solar Cell Spectral response measurement system (PV measurements, Inc (Model QEX10)) in transmittance mode.

4.3 Results

4.3.1 Simulation Results

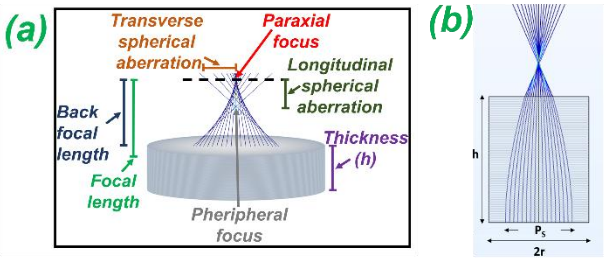

Figure 4-2: (a) Schematic showing the resulting ray properties when an initial parallel beam of some arbitrary peripheral ray span is focused on a planar GRI-L of thickness (h) (b) A schematic of a typical GRI-L showing the peripheral ray span and lens dimensions.

Figure 4.2a gives a schematic illustration of the optical characteristics of emergent rays from an arbitrary GRI-L. The optical axis of the GRI-L is an imaginary straight line through its geometrical center which joins the two centers of curvature of the lens surfaces. Rays along or closest to the optical axis making only a minute angle with it are paraxial rays whereas those farther away are the marginal or peripheral rays. The back-focal length and focal length of Luneburg lenses are designed to be unity whereas those for hyperbolic and parabolic GRI-Ls in Table 1 are given by Equation 4.[21].

$$f = \frac{1}{n_0 g \sin(gh)} \tag{2}$$

$$P = \frac{1}{f} \tag{3}$$

$$bfl = \frac{1}{n_0 g \tan(gh)} \tag{4}$$

Where f represents the focal length, bfl is back-focal length, g is a measure of the GRI-L parameter, n_o is the refractive index at the lens center and P is the dioptric power of the lens. Spherical aberrations occur when varying wavelengths are focused at different points on the focal plane. For convex lens systems for instance, they may be positive when the peripheral rays are closer to the lens surface than the paraxial rays or negative when the peripheral rays are focused further away from the lens surface than the paraxial ones. The longitudinal spherical aberration corresponds to the interspace along the optical axis over which an image is focused whereas, the interspace between the outermost ray and the optical axis at the paraxial focus is the transverse spherical aberration. Figure 2b shows a schematic of the rays as well as the lens dimensions. The distance between the farthest incident peripheral rays is the peripheral ray span (P_s).

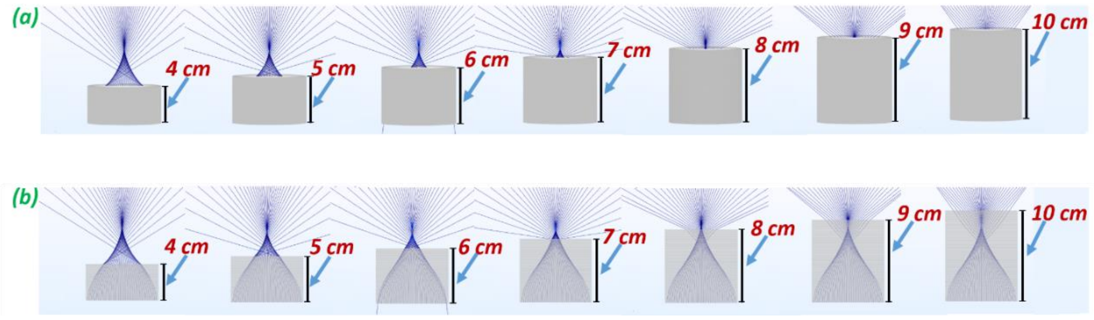

Figure 4-3: (a): Optical ray behavior for Luneburg power-law profiled B-SiO_2 ceramic GRI-Ls for varying lens thicknesses indicated in red. (b) Orthographic projection view of Luneburg power-law profiled B-SiO_2 ceramic GRI-Ls showing the ray propagation behavior within the lens structure, for varying lens thicknesses indicated in red.

Figure 4.3a shows that the optical ray behavior of the ray trajectories obtained for the printed lenses exhibiting Luneburg behavior (L1) have a refractive index varying according to the power law equation in table 1. The GRI-L constant (focal parameter) is a function of the initial refractive index at the center of the lens. The refractive index decreases to unity at a unique preset diameter, however, smaller dimensions may be utilized as well. By taking the refractive indices of both materials the B-SiO_2 at wavelength of 589.29 nm to be that of the lens at its origin, the focal parameter and the radius of the lens corresponding to the desired characteristic GRI-L profile ($\frac{\delta n}{\delta x}$) is fixed. The lens thicknesses were varied from 4 cm to 10 cm. The focal length expectedly reduces with increasing lens thickness until beyond 7 cm thickness where it domiciles within the lens structure. The cross-sectional views of both lenses expectedly indicate the gradual decrease of the refractive index from the lens center towards its circumference. Figure 4.3b, shows the orthographic projection view of the Luneburg GRI-Ls at specified lens thicknesses. This allows for evidence of the ray propagation behavior within the lens structure in addition to the location of the focal lengths. In addition to the power law profile, GRI-Ls with their refractive indices exhibiting a parabolic profile according to quadratic (S1) and hyperbolic functions (H1) shown in table 1 are also utilized in this work.

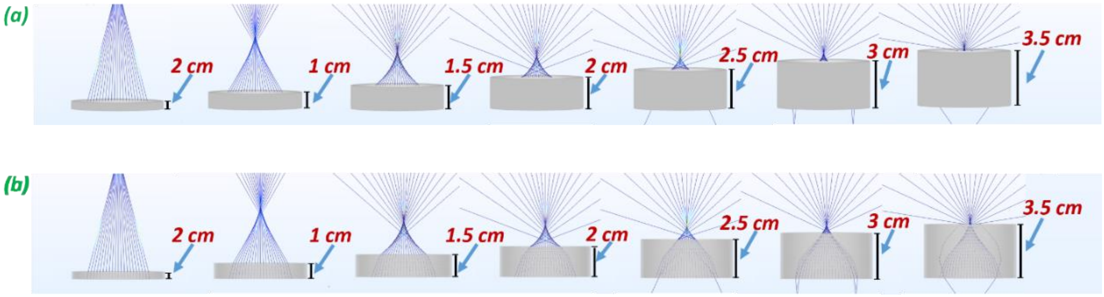

Figure 4-4 (a): Optical ray behavior for self-focusing quadratic profiled B-SiO_2 ceramic lenses (focal parameter = 1700.68 m^{-2}) for varying lens thicknesses. Thicknesses are indicated in red (b) Orthographic projection view of for self-focusing quadratic profiled B-SiO_2 ceramic lenses showing the ray propagation behavior within the lens structure. Thicknesses are indicated in red.

Figure 4.4a shows the observed emergent rays for a lens GRI-L profile based on quadratic (S1) profile for the B-SiO_2. The focal lengths are expectedly observed to reduce as the lens thickness increases. There is a lens thickness threshold beyond which the focal length becomes negative and the rays begin to diverge getting reflected back into the lens structure as observed in Figure 4.4b beyond the 2 cm thick lenses. A comparison between the series of figures in 4.3 and 4.4 shows that the emergent ray behavior expectedly depends on GRI-L profile utilized for simulation as will expectedly be the case in reality.

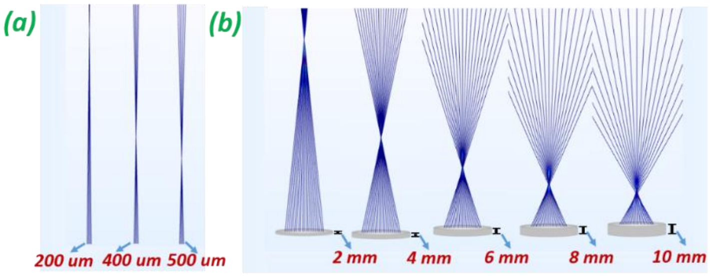

Figure 4-5: Optical ray trajectories for printed B-SiO_2 lenses with profiles varying parabolically; (a) micro-lenses with thicknesses indicated in red, (b) millimeter thick lenses with indicated thicknesses in red.

Figure 4.5 illustrates the results of the simulation for the optical behavior of the ray trajectories for printed B-SiO_2 ceramic lenses exhibiting the so-called SELFOC-lens behavior according to Table 1. Lens shown are for heights varying between 200 um and 10 mm. For a B-SiO_2 lens system where n = 1.47; for a 0.02 change in refractive index in a 4 cm radius lens, the GRI-L parameter can be estimated (A = 1700.68 m^{-2}). A lens of radius 4 cm was used. Equation 5 gives an expression to determine the number of slices (n_s) utilized for the simulation process for a given lens of thickness h.

$$s_n = \frac{h}{z_{res} f_c} \qquad (5)$$

Where z_{res} and fc are respectively the z-resolution of the SLA printing system and the fractional content of the B-SiO_2 particles by volume in the resin sludge before printing. In our case, the z-resolution used is that of the 3D printer (200 um) which is equivalent to 12500 slices /m according to equation 5.

Figure 4.6a shows the dioptric power as a function of lens thickness for a B-SiO_2-TiO_2 and pHEMA-TiO_2 system based on a hyperbolic (H1) GRI-L profiles. The lens power increases and plateaus at a thickness of about 0.038 m after which it decreases. The slight change in both power profiles implies that the material composition of the GRI-L lenses will affect the power of lenses for specific thicknesses. Lens thicknesses for applications requiring specific dioptric power may thus be estimated. Based on this thickness-power relation, the spherical longitudinal and transverse aberrations can be readily determined (Figure 4.6b) for different lens thicknesses. Fig. 6b shows the variation of the longitudinal and transverse spherical aberrations with increasing dioptric power of lenses for a quadratic(S1) GRI-L profile (g = 41 m^{-1}). The observed approximately increasing linear relationship correlates with reported trends for GRI-Ls such as natural, crystalline etc. [22]

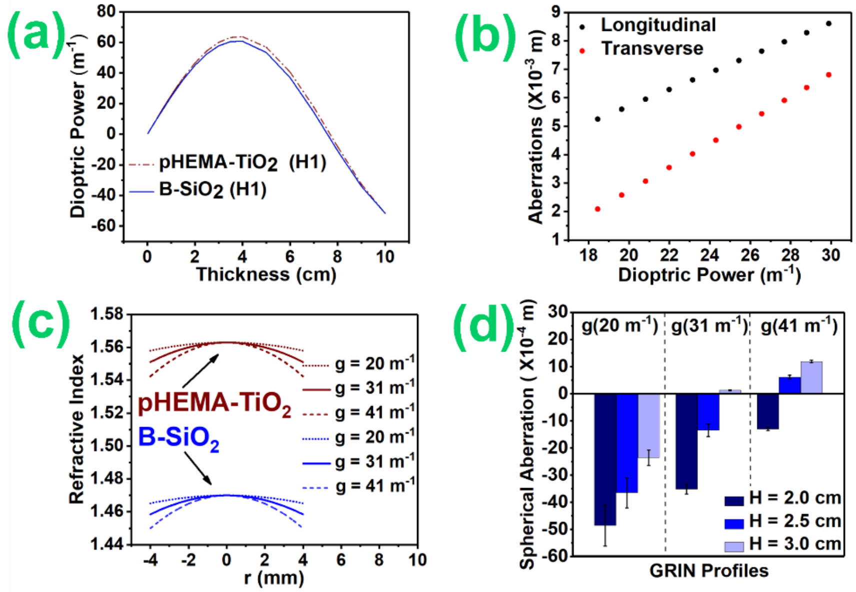

Figure 4-6: (a) Variation of Dioptric power with increasing thickness of Poly (Hydroxyethyl methacrylate) (pHEMA)-Titania (TiO_2) and Borosilicate (B-SiO_2) planar GRI-Ls for a Hyperbolic (H1) refractive index profiles. (b) Simulated spherical aberrations from a planar B-SiO_2 GRI-L with a quadratic GRI-L profile (S1) (g = 1700.68 m^{-2}) as a function of lens power. (Dioptric power range: 18 - 30 m^{-1}) (c) Refractive index profile for p(HEMA)-TiO_2 and B-SiO_2 lenses based on the hyperbolic refractive index expression in Table 1. GRI-L parameters are indicated, and the incident peripheral ray span is 0.032 m (d) Spherical aberration for B-SiO_2 lenses for varying heights and GRI-L parameters based on the hyperbolic refractive index expression in table 1.

For further specific optical studies, we considered a lens with a peripheral ray span of 3.2 cm (interspace between the farthest incident peripheral ray and the optical axis was fixed at 0.016 m) and utilized this for obtaining the spherical aberration values based on a hyperbolic index distribution (H1). In Figure 4.6c, the refractive index profile for the planar B-SiO_2 GRI-L based on a hyperbolic refractive index expression in table 1 is shown for a 4 mm radius with different GRI-L parameters. Higher GRI-L parameter values expectedly result in steeper profiles for both systems. Figure 4.6d shows the spherical aberrations for B-SiO_2 based lenses for varying lens thicknesses (2 cm – 3 cm) and GRI-L parameters for a hyperbolic refractive index profile. Within the ranges considered, aberrations become more positive both with increasing GRI-L parameter values and increasing lens thicknesses. Based on these results, zero aberration lenses can thus easily be extrapolated while keeping either of these two variables constant.

4.3.2 Experiment

A key factor in using this technique to obtain high quality lenses is to establish the miscibility and behavior of the resin sludge. In order to verify the miscibility of the resin and print process, we place our vat under a UV lamp of wavelength 365 nm. We utilize HEMA-TiO_2 sludge system as a test case. The resin vat was first filled with a HEMA based photocurable sludge with a 4 % TiO_2 content. After which an undoped auxiliary resin was introduced gradually into the vat while curing. The ratio of the primary and auxiliary resin systems was kept at 1:3 by volume at the end of the photocuring process. The vat was protected by an adjustable system of overlapping black plates which allowed for controlling the diameter of a central hole for light passage.

Figure 4.7a shows the EDS spectrum of the pHEMA structure modified by TiO_2 at an arbitrary position on the lens. The Titanium (K_α: 4.508 keV), Carbon (K_α: 0.277 keV) and Oxygen (K_α: 0.5249 keV) energy peaks are evident. The peak at 2.12 keV is characteristic for gold which was used in coating the lenses to enhance conductivity. The inset figure in

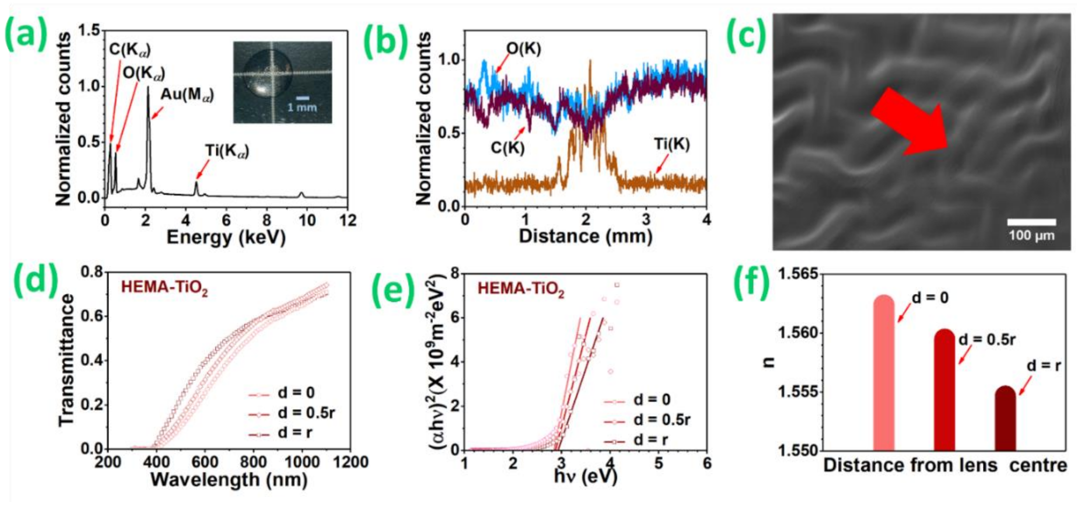

Figure 4-7: (a) Energy dispersive X-ray fluorescence spectroscopy of a TiO_2-pHEMA GRI-L (b)A linear distribution of characteristic EDX peaks for a TiO_2-pHEMA GRI-L across its diameter. (c) Scanning electron micrograph of a TiO_2-pHEMA GRI-L (arrow implies radially outwards) (d) The luminous transmittance of a TiO_2-pHEMA GRI-L at indicated spots on the lens. (e) Optical band gap extraction from fitting to the Tauc model for TiO_2-pHEMA GRI-L at indicated spots on the lens. (f) Position dependent refractive index of a TiO_2-pHEMA GRI-L.

figure 4.7a shows a lens with GRI-L profile shown in Figure 4.7b. Figure 4.7b shows the elemental concentration profile across the lens diameter. The expected increase in the intensity of the titanium characteristic peak and corresponding decrease in the carbon and oxygen peak profile establishes the miscibility and effectiveness of the technique. The scanning electron microscopy image is shown in Figure 4.7c. The observed zigzag structure of locally quasi-ordered domains indicate the gelled TiO_2 network embedded with the HEMA matrix. The red arrow indicates an outwardness towards the circumference of the lens and it is evident that there is a lower density of TiO_2 radially outwards. The SEM image observed is similar to that reported in previous TiO_2-HEMA reports [23], [24] . Figure 4.7d gives the optical transmittance as a function of wavelength at three spots on the lens (center (0) semi radius (r/2) and at the circumference (r). The optical transparency slightly increases radially outwards as is observed from the figure. We ascribe this to be as a result of the nature of the size of the TiO_2. TiO_2 nanoparticles are reported to have minimal effect on optical transparency whereas as particle size increases, this expectedly decreases. We presume that a reduced gelation time (aging time) could result in a TiO_2-HEMA lens system of higher transparency although this could result in trade-off for other properties. The decrease in the transparency however does not significantly affect the overall transparency or quality of the lens. The cut off wavelength is also found to decrease progressively radially outwards from 400 nm -370 nm. This cut-off wavelength corresponds to the wavelength below which a material absorbs all incident radiation and this expectedly depends strongly on dopant nature and concentration[25].

The quality of GRI-Ls may be characterized by correctly measuring the GRI-L profiles either via destructive or non-destructive techniques. Methods such as focusing method[26] Transverse ray tracing[27], interferometry [28], [29], tomography[30], [31] etc. have been reported. Our technique is simple and basic while allowing for a non-destructive and precise characterization as the easily measurable composition of the dopants is a direct reflection of the GRI-L profile. Figure 4.7e shows a plot that enables an estimation of the refractive index at different locations on the lens based on the Tauc model. The Tauc model is a model that is utilized for estimating the optical properties of transparent materials such as band gap, Urbach energy, refractive indices etc. from transmittance and absorptance data [32], [33]. Here, we determine the optical band gap E_g by considering a linear extrapolation to the zero ordinate of a plot of (ahv$^{1/2}$) against the incident photon energy (hv)[34]. The Tauc plot relation for optical band gap is given by equation. (6):

$$\frac{hv_a}{n} = A(hv - E_g) \text{ .... } (6)$$

Where h is the Planck's constant, ν is the vibration frequency, α is the absorption coefficient, E_g is the band gap energy, A is a constant proportionality and n is ½, 3/2, 2 or 3 for a direct, forbidden direct, indirect or forbidden indirect transition respectively.

The refractive index (n) obtained from the optical band gap was determined according to the equation. (7) based on the Lorenz theory:

$$\frac{n^2-1}{n^2+2} = 1 - \sqrt{\left(\frac{E_g}{20}\right)} \text{ .... } (7)$$

where n and $E_g$are the refractive index and optical band gap respectively. The refractive index values obtained at the three positions on the lens are shown in figure 4.7f. There is a decrease in value outwards.

Figure 8 a and b show the GRI-L profiles for an 8 mm diameter lens green ensemble. For similar compositions, the peak refractive index expectedly decreased with increasing spin coat speed due to the outward spreading of the stacked resins. The refractive index change Δn for the samples expectedly decreases with increasing spin coating speed. Figure 8 b further shows that when three layers of stacking (3L) in place of 2 was utilized, for a constant TiO_2 concentration and spincoating speed, though the peak refractive index remained the same, the refractive index change, Δn as well as the distribution was slightly different. The results show that tailoring composition as well as spincoating speed could be harmonized with simulation procedures to obtain precise GRI-Ls. Table 4 gives a comparison between the Δn values reported here and some previously reported ones, which indicate that the ranges reported for this work are close to those reported with the ones here easily tunable to desired GRI-L profile values.

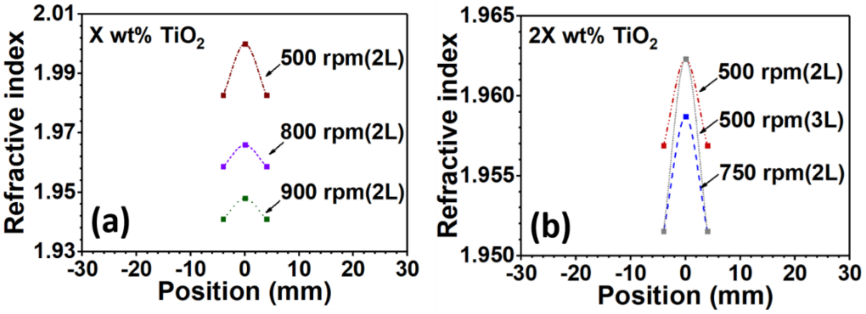

Figure 4-8: Refractive index profile of an exemplary (a) X wt% TiO_2 (b) 2X wt% TiO_2; of TiO_2-SiO_2-pHEMA GRI-L across the diameter of an 8 mm 3D printed lens. The spin coat speeds are indicated. 2L indicates two layers of auxiliary and primary resin were used before spincoating. 3L indicates the auxiliary resin was sandwiched between two layers of the primary resins.

Table 4-3: Summary of some refractive index gradient for optical GRI-Ls

Materials	Δn	Literature
Human eyes	0.02	[35]
High-low exposed photopolymer	0.015 (0.025 mm)	[36]
High-low exposed photopolymer	0.0044 (0.4 mm)	[37]
HEMA-Norland	0.049	[38]
HEMA-Epoxy	0.019-0.024	[39]
HEMA-(PPGEFM, PBAEG, NGDE)	0.062-0.0878	[40]
HEMA-(BECMA)	0.018	[40]
TiO_2 -SiO_2	0.02(4 mm)	[18]
HEMA-SiO_2-TiO_2(Experimental)	0.007- 0.022 (8 mm)	This work
HEMA-SiO_2-TiO_2 (Simulation)	0.011 (6 mm)	This work

4.4 Discussion

The SLA process for ceramics is known for products exhibiting a high degree of porosity values after calcination unlike other conventional ceramic fabrication processes where the product porosities are much lower (about 50% less). This higher porosity is due to the need to make the resin sludges flowable and compatible with the SLA process during printing. Hence there is a tradeoff between these and should be accounted for during the densification process where shrinkage takes place. In an ideal case, the final densified glass is proportional to the initial ceramic composition in the sludge and hence this is accounted for during the simulation procedure for printing in terms of the number of slices.

In practice, the inhomogeneity of the ceramic particles such as borosilicates will act as a hindrance towards effective sintering as there is a complicated mix of micro and nanoparticles in the sludge with different surface energies and diffusion rates during the densification process. Whereas the nanoparticles form amalgams or attach to the microparticles, the latter require much more energy for diffusion. However, the use of homogenous nanoparticles and sol-gel precursors in the case of this work, helps to eliminate this densification challenge thus resulting in a more efficient densification process. Our simulation accounts for the expected porosity by accommodating shrinkage in the printed body by utilizing appropriate number of slices although it however ignores the non-idealness of the densification process preferring to work with a simplified process partly because we have based our work on the sol-gel precursors which result in a homogenous network. Future work could entail investigating combinations of isothermal and non-isothermal temperature and time treatments for densification of non-homogenous systems to allow for more agreement of simulated and experimental data. Another factor that could affect the closeness of our results to the ideal is that here we have utilized the simplified ray optics which depends on Gaussian approximations and simple ray tracing and does not handle light as an electromagnetic wave which it actually is so that effects of diffraction for instance are neglected. Future work could consider the use of wave optics or more encompassing simulation procedures.

4.5 Conclusion

GRI-Ls for practical applications require preset distributions and the need to properly simulate these distributions to accurately predict the fabrication conditions is of paramount importance. In addition, from a technological stance, prior utilization of simulations before 3D printing results in saving time, cost, energy and other resources for fabricating quality GRI-Ls. Here we have to the best of our knowledge for the first time focused on adapting the SLA technique for GRI-L manufacture. Results from our simulations show several degrees of freedom and flexibility for the manufacture of gradient-index lenses based on both composition and design. Experimental results show the compatibility of ceramic sol-gel precursors and SLA hydroxyethyl methacrylate resins for photocurable sludge preparations. This study was carried out to demonstrate the possibility of the SLA cum simulation method for GRI-L fabrication. Accuracy, exactness and other correctness tests requiring more complexities should be tested to ascertain the predictive power of our simulation model for pure ceramic lenses even though they are a subject of work in progress by us and could be presented subsequently. Further development of the model should be made with the goal of qualitative prediction of properties and processing parameters. This could be a perfect tool for replacing conventional fabrication of GRI-Ls as well as improving the additive manufacturing process which is at a preliminary phase.

4.2 References

[1] N. Sugiura and S. Morita, "Variable-focus liquid-filled optical lens," *Appl. Opt.*, vol. 32, no. 22, pp. 4181–4186, Aug. 1993, doi: 10.1364/ao.32.004181.

[2] L. Dong, A. K. Agarwal, D. J. Beebe, and H. Jiang, "Adaptive liquid microlenses activated by stimuli-responsive hydrogels," *Nature*, vol. 442, no. 7102, pp. 551–554, Aug. 2006.

[3] J. C. Maxwell, ".," *Cambridge and Dublin Math.*, vol. 8, pp. 188–189, 1854.

[4] R Moore, "Plastic optical element having refractive index gradient," US3718383A, 1973.

[5] A. J. Yee and D. T. Moore, "Free-space infrared Mach–Zehnder interferometer for relative index of refraction measurement of gradient index optics," *Opt. Eng.*, vol. 56, no. 11, p. 111707, Apr. 2017.

[6] C. M. Schwarz *et al.*, "Fabrication and characterization of micro-structures created by direct laser writing in multi-layered chalcogenide glasses," in *Advanced Fabrication Technologies for Micro/Nano Optics and Photonics VIII*, Mar. 2015, vol. 9374, p. 937403.

[7] P. J. Wang *et al.*, "Study of 3D printing method for GRIN micro-optics devices," in *Advanced Fabrication Technologies for Micro/Nano Optics and Photonics IX*, Mar. 2016, vol. 9759, p. 975910.

[8] F. Horowitz, M. B. Pereira, S. Pelli, and G. C. Righini, "Towards a more accurate refractive index profile of ion-exchanged waveguides," *Thin Solid Films*, vol. 460, no. 1–2, pp. 206–210, Jul. 2004.

[9] A. Lepicard, F. Adamietz, V. Rodriguez, K. Richardson, and M. Dussauze, “Demonstration of dimensional control and stabilization of second harmonic electro-optical response in chalcogenide glasses,” *Opt. Mater. Express*, vol. 8, no. 6, pp. 1613–1624, Jun. 2018.

[10] K. A. Richardson *et al.*, “Advances in infrared gradient refractive index (GRIN) materials: a review,” *Opt. Eng.*, vol. 59, no. 11, p. 112602, Jun. 2020.

[11] J. R. Hensler, “Method of producing a refractive index gradient in glass,” US3873408A, Nov. 09, 1972.

[12] P. Sinai, “Correction of Optical Aberrations by Neutron Irradiation,” *Appl. Opt.*, vol. 10, pp. 99–104, Jan. 1971, Accessed: Jan. 28, 2021. [Online]. Available: https://www.osapublishing.org/viewmedia.cfm?uri=ao-10-1-99&seq=0&html=true.

[13] S. Ohmi, H. Sakai, Y. Asahara, S. Nakayama, Y. Yoneda, and T. Izumitani, “Gradient-index rod lens made by a double ion-exchange process,” *Appl. Opt.*, vol. 27, no. 3, pp. 496–499, Feb. 1988.

[14] L. Sisken *et al.*, “Infrared Glass–Ceramics with Multidispersion and Gradient Refractive Index Attributes,” *Adv. Funct. Mater.*, vol. 29, no. 35, p. 1902217, Aug. 2019.

[15] K. Richardson *et al.*, “Engineering novel infrared glass ceramics for advanced optical solutions,” in *Advanced Optics for Defense Applications: UV through LWIR*, May 2016, vol. 9822, p. 982205.

[16] D. T. Nguyen *et al.*, “3D printing: 3D printed Transparent Glass,” *Adv. Mater.*, vol. 29, no. 26, p. 1701181, 2017.

[17] F. Kotz *et al.*, “Three-dimensional printing of transparent fused silica glass,” *Nature*, vol. 544, no. 7650, pp. 337–339, 2017.

[18] R. Dylla-Spears *et al.*, “3D printed gradient index glass optics,” *Sci. Adv.*, vol. 6, no. 47, pp. 7429–7447, Nov. 2020.

[19] T. Liu, S. Guessasma, J. Zhu, W. Zhang, and S. Belhabib, “Functionally graded materials from topology optimisation and stereolithography,” *Eur. Polym. J.*, vol. 108, pp. 199–211, Nov. 2018.

[20] P. Gonzalez, E. Schwarzer, U. Scheithauer, N. Kooijmans, and T. Moritz, “Additive Manufacturing of Functionally Graded Ceramic Materials by Stereolithography,” *J.*

Vis. Exp., vol. 2019, no. 143, Jan. 2019.

[21] M. J. Riedl and Society of Photo-optical Instrumentation Engineers., “Optical design fundamentals for infrared systems,” p. 182, 2001.

[22] D. A. Atchison, “Aberrations associated with rigid contact lenses,” *JOSA A, Vol. 12, Issue 10, pp. 2267-2273*, vol. 12, no. 10, pp. 2267–2273, Oct. 1995.

[23] P. Gorbovyi, A. Uklein, S. Tieng, O. Brinza, M. T.- Nanoscale, and U. 2011, “Novel nanostructured pHEMA–TiO 2 hybrid materials with efficient light-induced charge separation,” *pubs.rsc.org*, 2011, Accessed: Dec. 16, 2021. [Online]. Available: https://pubs.rsc.org/en/content/articlehtml/2011/nr/c0nr00909a.

[24] M. Sangermano, E. Amerio, A. Priola, A. Di Gianni, and B. Voit, “Preparation and characterization of acrylic resin/titania hybrid nanocomposite coatings by photopolymerization and sol–gel process,” *J. Appl. Polym. Sci.*, vol. 102, no. 5, pp. 4659–4664, Dec. 2006.

[25] M. W. Kielty *et al.*, “Investigation of Ce3 + luminescence in borate-rich borosilicate glasses,” *J. Non. Cryst. Solids*, vol. 471, pp. 357–361, Sep. 2017, doi: 10.1016/J.JNONCRYSOL.2017.06.022.

[26] D. Marcuse and H. M. Presby, “Preform index profiling (PIP),” *Appl. Opt. Vol. 18, Issue 5, pp. 671-677*, vol. 18, no. 5, pp. 671–677, Mar. 1979, Accessed: Dec. 16, 2021. [Online]. Available: https://www.osapublishing.org/viewmedia.cfm?uri=ao-18-5-671&seq=0&html=true.

[27] D. Peri and P. L. Chu, “Measurement of refractive-index profile of optical-fibre preform by means of spatial filtering,” *Electron. Lett.*, vol. 17, no. 11, pp. 371–372, May 1981.

[28] K. Iga and Y. Kokubun, “Refractive-index profile measurement of preform rods by a transverse differential interferogram,” *Appl. Opt. Vol. 19, Issue 6, pp. 846-851*, vol. 19, no. 6, pp. 846–851, Mar. 1980.

[29] W. E. Martin, “Refractive Index Profile Measurements of Diffused Optical Waveguides,” *Appl. Opt. Vol. 13, Issue 9, pp. 2112-2116*, vol. 13, no. 9, pp. 2112–2116, Sep. 1974.

[30] B. Dobler, B. Messerschmidt, H. Schreiber, K.-H. Brenner, and W. Singer, “Refractive-index measurement of gradient-index microlenses by diffraction tomography,” *Appl. Opt. Vol. 35, Issue 13, pp. 2167-2171*, vol. 35, no. 13, pp. 2167–2171, May 1996.

[31] D. Vazquez, E. Acosta, G. Smith, and L. Garner, “Tomographic method for measurement of the gradient refractive index of the crystalline lens. I. The spherical fish lens,” *JOSA A, Vol. 22, Issue 3, pp. 424-433*, vol. 22, no. 3, pp. 424–433, Mar. 2005.

[32] J. Tauc and A. Menth, “States in the gap,” *J. Non. Cryst. Solids*, vol. 8–10, no. C, pp. 569–585, Jun. 1972.

[33] A. Saeed, Y. H. Elbashar, and S. U. El Kameesy, “Optical Spectroscopic Analysis of High Density Lead Borosilicate Glasses,” *Silicon*, vol. 10, pp. 185–189, 2018.

[34] P. Limkitjaroenporn, J. Kaewkhao, P. Limsuwan, and W. Chewpraditkul, “Physical, optical, structural and gamma-ray shielding properties of lead sodium borate glasses,” *J. Phys. Chem. Solids*, vol. 72, no. 4, pp. 245–251, 2011.

5 Hybrid polymers for gradient refractive index lens, additive manufacturing

5.1 Introduction

Hybrid Photopolymers are polymers which combine the two or more polymeric systems is such a way that complementary desirable properties are harnessed simultaneously. They usually consist of two or more polymer systems which undergo characteristic photoploymerization mechanisms so that photocuring results in an interpenetrating crosslinked network of the parent systems. Several categories of resins are currently adaptable to the SLA (VPP in general) technique and these include free radical systems, cationic systems, anionic systems, initiator free systems etc. Radical systems for instance consist mainly of acrylates (and methacrylates) as the main monomeric component and they undergo free radical polymerization so that they require the presence of free radical sources for polymerization initiation. The polymerization process is relatively fast, and their functional groups are easily modifiable. They exhibit a high degree of shrinkage after printing of about 20 %, have very high reactivity and poor mechanical properties. They are comparatively more volatile with poor odor and their polymerization are inhibited by oxygen presence [1]–[4]. On the other hand, epoxides, oxetanes and vinyl ethers make up the cationic resin systems which depend on cation sources for polymerization initiation. Their cure rate is relatively slower and their functional groups are not easily modifiable. They exhibit very low shrinkage and better mechanical properties. They are less volatile, inhibited by moisture and their odor is not as pungent as radical resin systems.[3], [5]–[11]. A combination of di-functional oxetanes and epoxides have been shown to improve some of the key limitations of epoxide resins such as mechanical properties (cycloaliphatic epoxies crosslinked by oxetanes [12]. In works by Tingting Zhao et al. [13], [14] silicone–epoxy-acrylate composition were optimized to yield a hybrid resin utilized for SLA printing. The thermal, mechanical and curing rate were all studied for best resin properties. A microstereolithography system has also been recently developed which allows for in situ hybrid structure miniature fabrication using multiple photocurable polymers [15].

Conventional fabrication modes for lenses entail spin casting, molding and lathe cutting. In order to generate gradient refractive index (GRIN) on substrates several approaches have been utilized. For polymeric lenses, the use of photocurable systems[16]–[19] [have been reported. The use of additive manufacturing for GRI-Ls based on hybrid polymers is however yet to be reported.

This work demonstrates a modelling and simulation approach that predicts the use of photocurable pre-polymer mix of acrylates and epoxies for fabricating GRI-Ls as well as establishes optical properties of the resulting hybrid lenses. Unlike other methods for GRI-L fabrication, this technique allows for better resolution of structures, is cheap and easy to carry out, produces a precise distribution of the refractive index and is less complex. In addition, properties such as spherical aberrations can be tuned for optimum performance.

5.2 Experimental Procedure

Our approach entails the combination of two miscible pre-polymeric material systems so that there is a possibility of having a functionally graded cylindrical lens where refractive index varies radially from the lens center to the lens circumference. We utilize a hybrid resin system comprising acrylate and epoxy monomers. As a test case we utilize (hydroxyethyl)methacrylate (HEMA) with a refractive index of 1.514 as the acrylate component.

The 3D printer comprises a z-control and x-y control, which control the laser motion during printing. The Vat containing the resin is placed on stationary stage which can be adjusted to allow for focusing of the laser. For the computer control, a Candle Grbl software was utilized. First the model to be printed was designed with CAM softwares such as Inkscape. This is then converted to a G-code which is then run on the Candle software which controls the laser motion accordingly.

The simulation entails the use of COMSOL in determining the optical properties of lenses produced from a photocuring process based on a laboratory-made laser system that photocures resolution-determined rings per step off a pre-polymer resin contained in a vat. The system allows for an alternate print, hold and mix process. The times between laser motion, and the speed of a stirrer immersed in the resin tank are programmed to accommodate an alternate introduction and mixing of both components based on [20]:

$$t_m = K(V_L/N_i)^{1/3} \qquad (1)$$

where, t_m is the mixing time, V_L is the liquid volume, N_i is the stirrer speed and K is an experimentally determinable constant. The estimated amount of the secondary liquid constituent can be estimated from:

$$n(r) = v_1 n_1 + (1-v_1)n_2 \quad \Delta r < 0.2 \qquad (2)$$

where, n(r) is the refractive index of the resultant mix, v is the fractional content, n_1 and n_2 are the refractive indices of the individual constituent liquids.

The GRI-Ls may follow any of profiles described in (3):

$$n(r) = n_0(\text{sech}\,(gr)) \qquad (3a)$$

$$n(r) = n_o\left(1 - \frac{{g_o}^2}{2} r^2\right) \qquad (3b)$$

$$n(r) = \frac{1}{f}\sqrt{1 + f^2 - (\frac{r}{R})^2} \qquad (3c)$$

where n(r) is the refractive index at location r from the origin; n_0 is the refractive index at the origin, R is the radius of the lens and f and g are focal and GRI-L parameters, respectively.

5.3 Results and Discussion

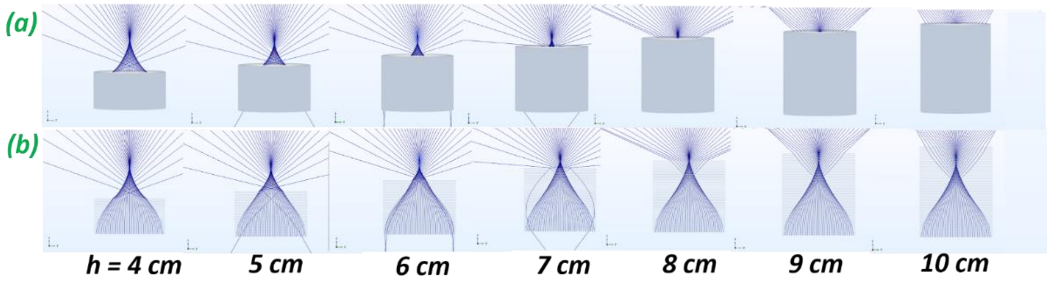

Figure 5-1: (a) Optical ray behavior for Luneburg power-law profiled p(HEMA) polymer GRI-Ls for varying lens thicknesses indicated (h). (b) Orthographic projection view of Luneburg power-law profiled p(HEMA) polymer GRI-Ls showing the ray propagation behavior within the lens structure, for varying lens thicknesses indicated.

Figure 5.1a shows that the optical ray behavior of the ray trajectories obtained for the printed lenses exhibiting Luneburg behavior (L1) have a refractive index varying according to the power law equation (eqn 3c). The GRI-L constant (focal parameter) is a function of the initial refractive index at the lens center. The refractive index decreases to unity at a unique preset diameter, however, smaller dimensions may be utilized as well. By taking the refractive indices of both materials the p(HEMA) at wavelength of 589.29 nm to be that of the lens at its origin, the focal parameter and the radius of the lens corresponding to the desired characteristic GRI-L profile $(\frac{\delta n}{\delta x})$ is fixed. The lens thicknesses were varied from 4 cm to 10 cm. The focal length expectedly reduces with increasing lens thickness until beyond 7 cm thickness where it domiciles within the lens structure. The cross-sectional views of both lenses expectedly indicate the gradual decrease of the refractive index from the center towards the lens circumference. Figure 5.1b, shows the orthographic projection view of the Luneburg GRI-Ls at specified lens thicknesses. This allows for evidence of the ray propagation behavior within the lens structure in addition to the location of the focal lengths. In addition to the power law profile, GRI-Ls with their refractive indices exhibiting a parabolic profile according to quadratic (S1) and hyperbolic functions (H1) shown in table 1 are also utilized in this work.

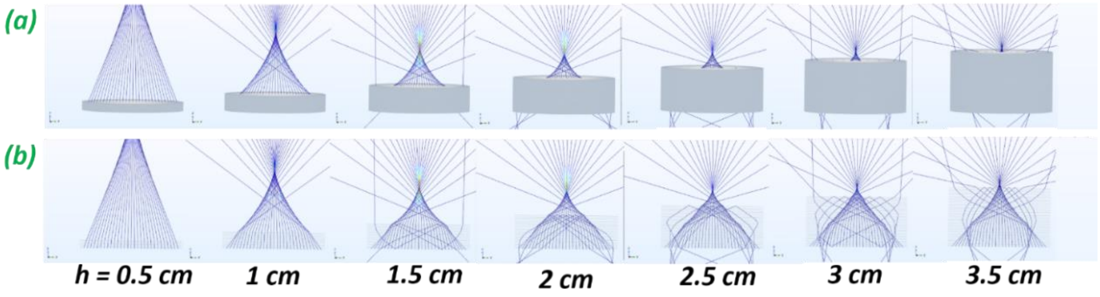

Figure 5-2: (a) Optical ray behavior for self-focusing quadratic profiled p(HEMA) polymer GRI-Ls for varying lens thicknesses indicated (b) Orthographic projection view of for self-focusing quadratic p(HEMA) polymer GRI-Ls showing the ray propagation behavior within the lens structure, for varying lens thicknesses indicated.

Figure 5.2a shows the observed emergent rays for a lens GRI-L profile based on quadratic (S1) profile for the p(HEMA). The focal lengths are expectedly observed to reduce as the lens thickness increases. There is a lens thickness threshold beyond which the focal length becomes negative and the rays begin to diverge getting reflected back into the lens structure as observed in Figure 5.2b beyond the 1 cm thick lenses. A comparison between the series of figures in 5.1 and 5.2 shows that the emergent ray behavior expectedly depends on GRI-L profile utilized for simulation as will expectedly be the case in reality.

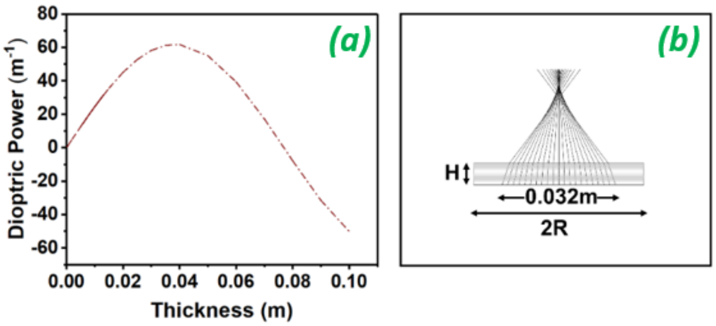

Figure 5-3: (a) Refractive index profile for p(HEMA) lenses based on the hyperbolic refractive index expression in eqn 3a. GRI-L parameters are indicated, and the incident peripheral ray span is given 0.032 m (b) A schematic of a typical p(HEMA) GRI-L showing the peripheral ray span.

Figure 5.3a shows the dioptric power as a function of lens thickness for a pHEMA system based on a hyperbolic GRI-L profiles. The lens power increases and plateaus at a thickness of about 0.038 m after which it decreases. Figure 5.3b shows a schematic of the rays as well as the lens dimensions. The distance between the farthest incident peripheral rays is the peripheral ray span (Ps).

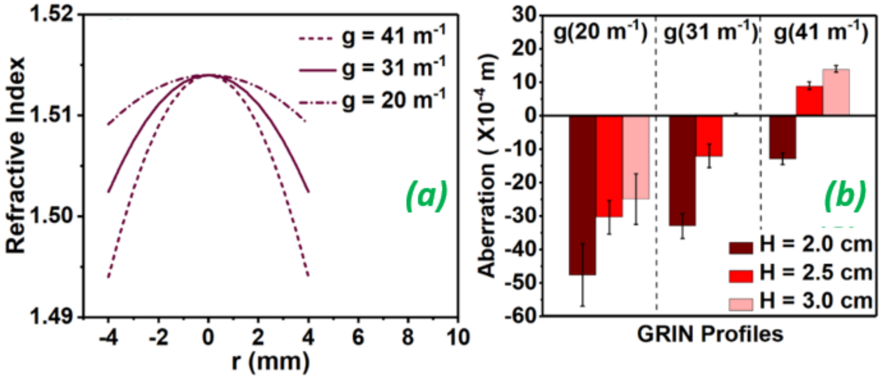

Figure 5-4: (a) Refractive index profile for p(HEMA) lenses based on an hyperbolic refractive index expression (eqn 3a). GRI-L parameters are indicated, and the incident peripheral ray span is 0.032 m (b) Spherical aberration for pHEMA lenses for varying heights and GRI-L parameters based on a hyperbolic refractive index expression (eqn 3a)

In Fig.5-4(a), the refractive index profile for the HEMA based lens based on a hyperbolic refractive index expression in (3) is shown for a 4 mm radius with different GRI-L parameters. Higher GRIL parameter values expectedly result in steeper profiles. Fig. 4(b) shows the spherical aberrations for HEMA based lenses for varying heights (2 cm – 3 cm) and GRI-L parameters for a hyperbolic refractive index profile. Within the ranges considered, aberrations become more positive both with increasing GRI-L parameter values and increasing lens thicknesses for a fixed peripheral ray span. Based on these results, zero aberration lenses can thus easily be extrapolated while keeping either of the two variables constant.

5.4 Conclusion

In this work, the resultant ray optical properties are estimated for cylindrical GRI-Ls based on a hybrid polymer resin system. Though useful for the evaluating the behavior of fabricated lenses, variations for real lenses may occur. Future research could take into cognizance the 3D printer properties such as the x-y and z- print resolutions and results should be further verified by real measurements. This work demonstrates a method that paves the way for more efficient fabrication processes for GRI-Ls by using hybrid photocurable polymer systems.

5.5 References

[1] R. Yu *et al.*, “Three-dimensional printing of shape memory composites with epoxy-acrylate hybrid photopolymer,” *ACS Appl. Mater. Interfaces*, vol. 9, no. 2, pp. 1820–1829, Jan. 2017, Accessed: Jan. 20, 2022. [Online]. Available: https://pubs.acs.org/doi/abs/10.1021/acsami.6b13531.

[2] J. Steindl, A. Svirkova, M. Marchetti-Deschmann, N. Moszner, and C. Gorsche, “Light-Triggered Radical Silane-Ene Chemistry Using a Monosubstituted Bis(trimethylsilyl)silane,” *Macromol. Chem. Phys.*, vol. 218, no. 9, p. 1600563, May 2017.

[3] C. Tang and W. Liu, “Synthesis of cationic UV-curable methacrylate copolymers and properties of the cured films of their composites with alicyclic epoxy resin,” *J. Appl. Polym. Sci.*, vol. 123, no. 3, pp. 1724–1731, Feb. 2012, Accessed: Jan. 20, 2022. [Online]. Available: https://onlinelibrary.wiley.com/doi/full/10.1002/app.34637.

[4] L. H. Nguyen and M. Gu, “Decomposition Kinetics, Life Estimation, and Dielectric Study of an Acrylate based Photopolymer for Microfabrication and Photonic Applications,” *Macromol. Chem. Phys.*, vol. 206, no. 16, pp. 1659–1664, Aug. 2005.

[5] J. Serbin, B. N. Chichkov, and R. Houbertz, “Three-dimensional nanostructuring of hybrid materials by two-photon polymerization,” *Nanocrystals, Org. Hybrid Nanomater.*, vol. 5222, p. 171, Nov. 2003.

[6] K. H. Jung and B. S. Bae, “Synthesis and characterization of photopatternable epoxy hybrid materials for the fabrication of thick and thermally stable microstructures with a high aspect ratio,” *J. Appl. Polym. Sci.*, vol. 108, no. 5, pp. 3169–3176, Jun. 2008.

[7] J. V. Crivello and R. A. Ortiz, “Design and synthesis of highly reactive photopolymerizable epoxy monomers,” *J. Polym. Sci. Part A Polym. Chem.*, vol. 39,

no. 14, pp. 2385–2395, Jul. 2001.

[8] F. B. Leal, C. M. Pereira, and F. A. Ogliari, “Synthesis, characterization, and photocuring of siloxane-oxirane monomers,” *J. Polym. Sci. Part A Polym. Chem.*, vol. 53, no. 14, pp. 1728–1733, Jul. 2015.

[9] R. A. A. Upul Ranaweera, T. P. Schuman, R. Wang, B. D. Miller, and K. V. Kilway, “Effect of moisture on cationic polymerization of silicone epoxy monomers,” *J. Appl. Polym. Sci.*, vol. 132, no. 15, Apr. 2015, doi: 10.1002/APP.41831.

[10] P. S. Balakrishnan and S. C. Murugavel, “Spectral, thermal, and photoreactivity studies on epoxy resin containing benzylidene units in the main chain,” *J. Appl. Polym. Sci.*, vol. 111, no. 5, pp. 2340–2344, Mar. 2009.

[11] X. Guillory *et al.*, “Glycidyl alkoxysilane reactivities towards simple nucleophiles in organic media for improved molecular structure definition in hybrid materials,” *RSC Adv.*, vol. 6, no. 78, pp. 74087–74099, Aug. 2016.

[12] S. Yang, J. Jin, S.-Y. Kwak, and B.-S. Bae, “Photocurable Transparent Cycloaliphatic Epoxy Hybrid Materials Crosslinked by Oxetane,” *J Appl Polym Sci*, vol. 000, pp. 0–000, 2012.

[13] T. Zhao *et al.*, “A comparative study on 3D printed silicone-epoxy/ acrylate hybrid polymers via pure photopolymerization and dual-curing mechanisms,” *J. Mater. Sci.*, vol. 54.

[14] T. Zhao *et al.*, “Silicone–Epoxy-Based Hybrid Photopolymers for 3D printing,” *Macromol. Chem. Phys.*, vol. 219, no. 10, p. 1700530, May 2018.

[15] S. Maruo, K. Ikuta, and T. Ninagawa, “Multi-polymer microstereolithography for hybrid opto-MEMS,” *Proc. IEEE Micro Electro Mech. Syst.*, pp. 151–154, 2001.

[16] R Moore, “Plastic optical element having refractive index gradient,” US3718383A, 1973.

[17] A. J. Yee and D. T. Moore, “Free-space infrared Mach–Zehnder interferometer for relative index of refraction measurement of gradient index optics,” *Opt. Eng.*, vol. 56, no. 11, p. 111707, Apr. 2017.

[18] C. M. Schwarz *et al.*, “Fabrication and characterization of micro-structures created by direct laser writing in multi-layered chalcogenide glasses,” in *Advanced*

Fabrication Technologies for Micro/Nano Optics and Photonics VIII, Mar. 2015, vol. 9374, p. 937403.

[19] P. J. Wang *et al.*, “Study of 3D printing method for GRIN micro-optics devices,” in *Advanced Fabrication Technologies for Micro/Nano Optics and Photonics IX*, Mar. 2016, vol. 9759, p. 975910.

[20] M. P. Doran, “Engineering Principles Second Edition,” *Acad. Press*, p. 903, 2013.

6 Summary and recommendation

6.1 Summary

The major conclusions from this study are

1. Transparent undoped and Ce doped borosilicate glass have been successfully synthesized with a dopant level of up to 10 mol % by stereolithography, calcining and densification in air and vacuum. The calcination temperature is about 98% of the softening temperature and the glass exhibits no devitrification and good optical properties, which can be further modified to yield functional glass materials.
2. We have designed a time, and resource saving method for fabricating quality GRI-Ls. Here we have focused on adapting the SLA technique for GRI-L manufacture. This helps to have preset distributions to properly simulate these distributions to accurately predict the fabrication conditions. Results from our simulations show several degrees of freedom and flexibility for the manufacture of gradient-index lenses based on both composition and design. Experimental results show the compatibility of ceramic sol-gel precursors and SLA hydroxyethyl methacrylate resins for photocurable sludge preparations.
3. In this work, the resultant ray optical properties are estimated for cylindrical GRI-L based on a hybrid polymer resin system for SLA adaptability. Though useful for the evaluating the behavior of fabricated lenses, variations for real lenses may occur. This work demonstrates a method that paves the way for more efficient fabrication processes for GRI-Ls by using hybrid photocurable polymer systems.

6.2 Recommendations for Future Work

Our fabrication approach for B-SiO_2 glass provides a potentially promising path for the application of VPP, powder bed fusion and other additive manufacturing techniques for B–SiO_2 glass fabrication. It is a procedure that will allow for rapid, digital and on-demand manufacturing for advanced optical and luminescence systems. Our study on GRI-Ls was designed to demonstrate the possibility of the SLA cum simulation method for GRI-L fabrication. Accuracy, exactness and other correctness tests requiring more complexities should be tested to ascertain the predictive power of our simulation model for pure ceramic lenses. Further development of the model should be made with the goal of qualitative prediction of properties and processing parameters. This could be a perfect tool for replacing conventional fabrication of GRI-Ls as well as improving the additive manufacturing process which is at a preliminary phase.

In general, future research could take into cognizance the 3D printer properties such as the x-y and z- print resolutions and results should be further verified by real measurements.

APPENDIX

A. APPENDIX: Additive Manufacturing of Borosilicate Glass via Stereolithography

Table A1: Summary of some properties of the B-SiO$_2$ powder used.

Properties	
*Density	2.13 g/cm^3
*Particle size	<40 µm
*Dielectric constant	4.6 (@1e6 Hz)
*Annealing temperature	925 ˚F
**Softening temperature	711 ˚C
**BET surface Area	282.01 m^2/g
*Indicates data culled from data sheet of the commercial sample powder (Corning 7070) ** Indicates measured properties	

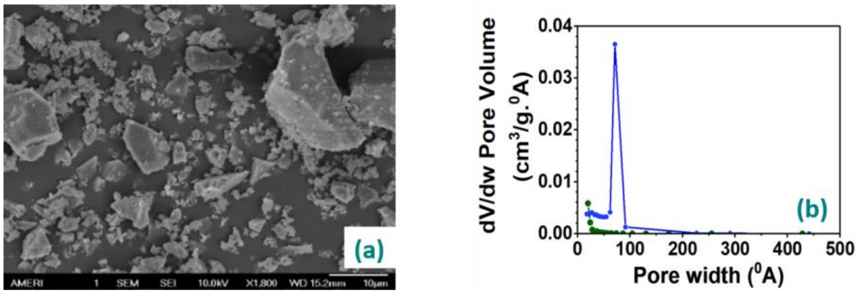

Figure A-1: Scanning electron microscopy images of the borosilicate particles used for the additive manufacturing of the green parts. (b) Pore volume plots determined from Nitrogen adsorption isotherms fit with BJH model for (B-SiO$_2$, Corning 7070(green)) (Estimated BET surface area = 282.01m^2/g) and (SBA-15(Blue)) (Estimated BET surface area = 472.37m^2/g). The data shows the absence of porosity in the B-SiO$_2$ sample utilized for printing.

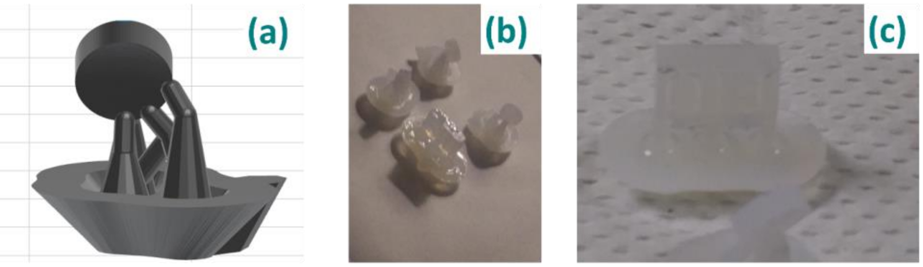

Figure A-2: (a) Computer aided model of a typical pellet utilized for printing the green bodies. (b) Printed green pellets and an exemplary structure on supports before calcination (c) An expanded view of the printed FIU green body structure still on the supports before calcination.

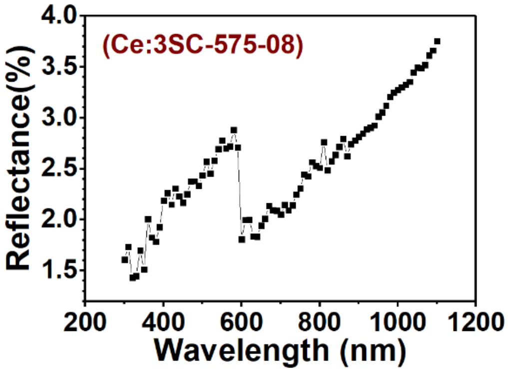

Figure A-3: (a) Reflectance loss spectra for 3D printed Cerium doped Borosilicate glass with 8% Cerium dopant concentration

B. APPENDIX

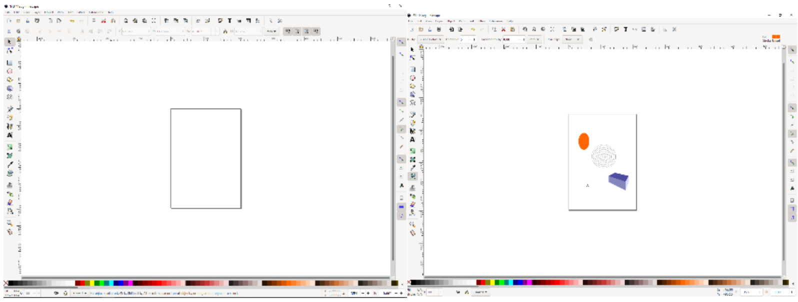

Figure B-1: Inkscape page for CAD designs, (b) Inkscape page showing some sample designs before G-code generation.

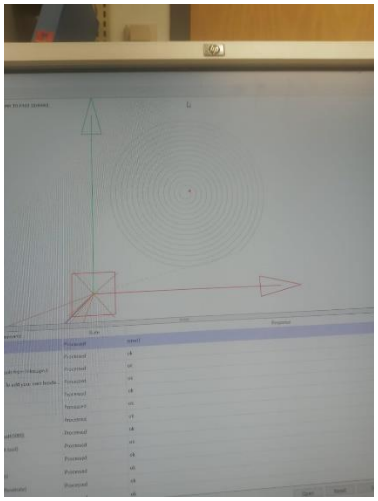

Figure B-2: A sample 3D CAD spiral figure for printing opened on a Candle GRBL software from its G-code file.

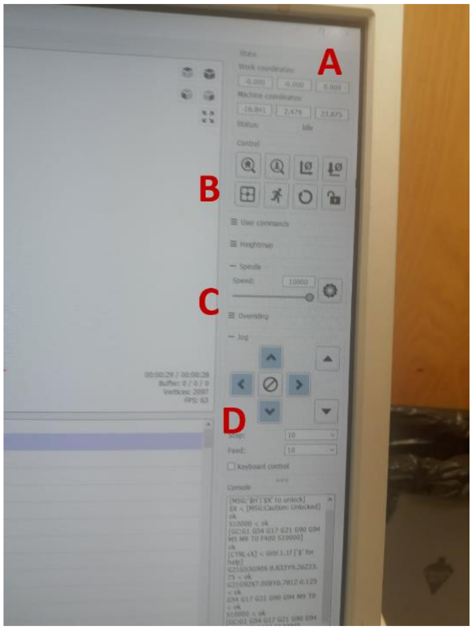

Figure B-3: Segments of the Candle software operating window showing (A)x-y and z- coordinates (B)Printer controls (C) Laser intensity control (D) Laser motion control.

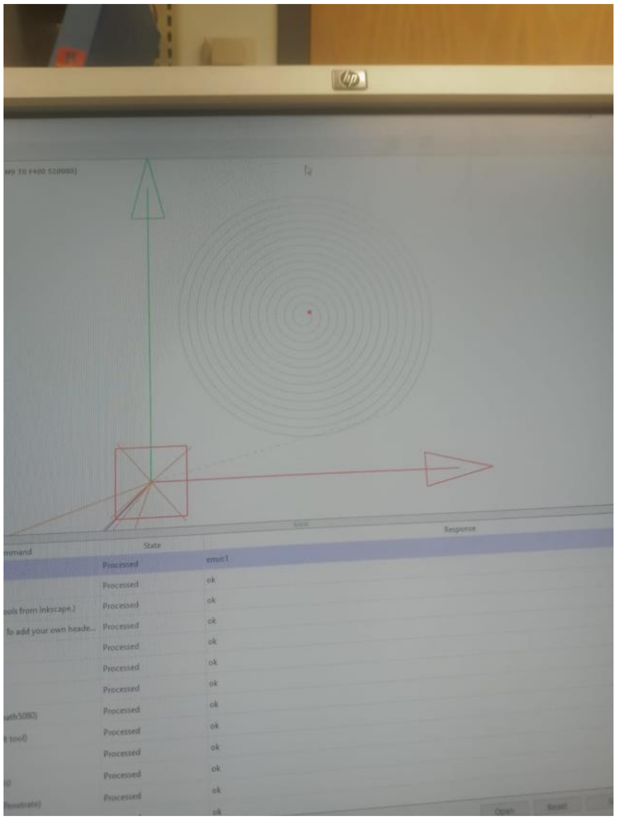

Figure B-4: The interface of the operating window of the Candle GRBL software showing a sample glass spiral design for printing.

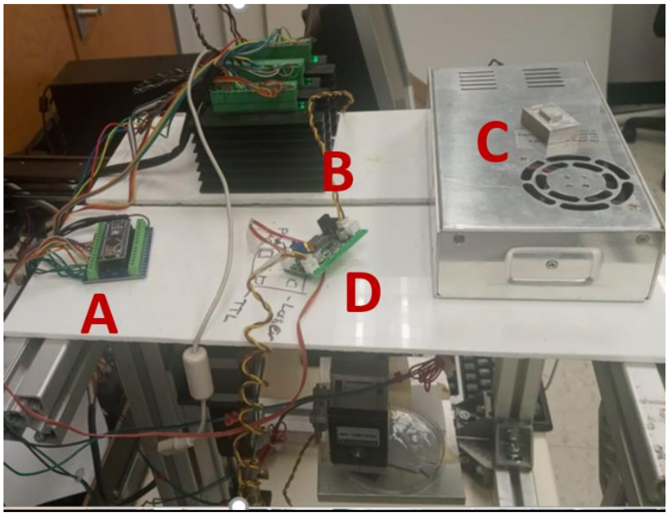

Figure B-5: Schematic of 3D printer (Top view)
(A = Contact point to the computer and software; D = connection to the laser).

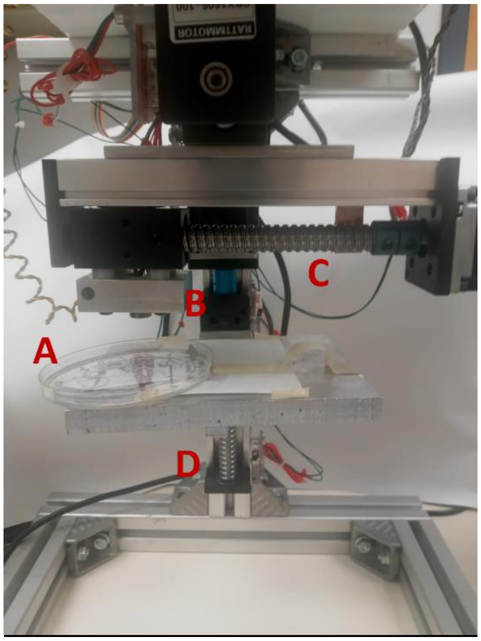

Figure B-6: Schematic of the 3D printer: Front view
(A = Resin vat for holding resin sludge; B = Laser holder with laser source mounted on it; C = x-y motion control; D = z motion control).

C. APPENDIX: List of Abbreviations

SiO_2	Silica
GRI-L	Gradient index lens
B-SiO_2	Borosilicate
3D	Three dimensional
T_p	Printing temperature
T_c	Calcination temperature
T_d	Densification temperature
T_s	Softening Temperature
SLA	Stereolithography
VPP	Vat Photopolymerization
C	Celsius
Ce	Cerium
SEPS	Suspension-enclosing projection stereolithography
DLP	Digital light Projection
APTMS	3- acryloxypropyl trimethoxysilane
MPP	Mulitphoton Polymerization
DSC	Differential Scanning Calorimetry
TGA	Thermogravimetric Analysis
XRD	Xray diffraction
pHEMA	Poly (Hydroxyethyl methacrylate)
TiO_2	Titanium IV oxide
2D	Two dimensional
UV	Ultraviolet
AM	Additive Manufacturing
DIW	Direct Ink Writing
PDMS	polydimethylsiloxane
2PP	Two photon photopolymerization
SiOC	Silicon Oxycarbide
CAL	computed axial lithography
FDM	fused deposition modelling
PBF	powder bed fusion
TEGDA	Tetraethylene glycol diacrylate
DMPA	2,2-dimethoxy-2-phenylacetophenone.
TEOS	Tetraethyl Orthosilicate
MAPTMS	Methacryloxypropyl trimethoxysilane
CGP	Chain growth polymerization
SGP	Step growth polymerization
H_2O	Water
HCl	Hydrogen Chloride
NH_3	Ammonia
CH_3OH	Methanol
ZrO_2	Zirconia
PDC	polymer derived ceramics, PDC
DLW	Direct Laser Writing
YAG	Yittrium Aluminium garnet
Er	Erbium
Yb	Ytterbium
GeO_2	Germanium oxide
ML	Machine Learning
AI	Artificial Intelligence

CAD	Computer aided Designs
DL-ELM	Double-Layered Extreme Learning Machine
B_2O_3	Boron oxide
MEMS	Micro electromechanical systems
SLM	Selective laser melting
CO2	Carbon IV oxide
SEM	Scanning Electron Microscopy
BET	Brunauer–Emmett–Teller
EDS	Energy Dispersive Spectroscopy
h	Planck's constant
ν	Vibration frequency
α	Absorption coefficient
E_g	Band gap energy
n	Refractive index
E_u	Band gap energy
R	Reflectance losses
eV	electron Volt
Sm	Samarium
Pr	Praseodymium
Nd	Neodymium
Cr	Chromium
Mn	Manganese
Co	Cobalt
Ti	Titanium
Pb	Lead
ε	Dielectric constant
PMMA	Poly (methyl methacrylate)
F	Focal length
Bfl	Back-focal length
G	Measure of the GRI-L parameter
n_o	Refractive index at the lens center
P	Dioptric power
CAM	Computer aided Model

VITA

OKPOWE OMENA

2003-2008	B.Sc. Engineering Physics Obafemi Awolowo University
2009-2010	M.Sc. Materials Science African University of Science and Technology Abuja, Nigeria
2014-2017	M.Sc., Materials Science and Engineering, Florida State University Tallahassee, Florida
2017-2022	Doctoral Candidate (PhD) Florida International University Miami, FL, USA

SELECTED JOURNAL PUBLICATIONS

Journal Papers

1. Omena Okpowe, Nezih Pala, Chunlei Wang. Recent Progress in Vat Additive Manufacturing of Silica based Glass Ceramics. Ceramic International (Under Review).
2. Omena Okpowe, Vadym Drozd, Oscar Ares-Muzio, Nezih Pala, Chunlei Wang, Additive Manufacturing of Borosilicate Glass via Stereolithography. Ceramics International, Vol 48, Issue 9, 1 May 2022, Pages 12721-12728.
3. Adelowo, E., Baboukani, A. R., Okpowe, O., Khakpour, I., Safa, M., Chen, C., & Wang, C., 2020. A high energy aqueous on-chip lithium-ion capacitor based on interdigital 3D carbon microelectrode arrays. Journal of Power Sources, 455, 227987. https://doi.org/10.1016/j.jpowsour.2020.227987.
4. O. Okpowe, A. Durygin, V. Drozd, T. Olowu, N. Pala and C. Wang, Hybrid Polymers for Gradient Refractive Index Lens, 2021 IEEE Photonics Conference (IPC), 2021, pp. 1-2, doi: 10.1109/IPC48725.2021.9592871.
5. Adelowo, E. D., Agrawal, R., Okpowe, O., Rabei Baboukani, A., & Wang, C. (2019). Development of high-performance hybrid capacitors. SPIE, 10979, 7. https://doi.org/10.1117/12.2520249.
6. Omena Okpowe, Nezih Pala, Chunlei Wang, U.S. Patent No.10,940,639B1.
7. Omena Okpowe, Nezih Pala, Chunlei Wang, U.S. Patent No. 11,130,283B2.
8. Omena Okpowe, Nezih Pala, Chunlei Wang Gradient refractive index lenses and methods of fabricating the same (Patent draft submitted).